# HEAT GENERATION MECHANISMS IN ENERGETIC COMPOSITE MATERIALS UNDER ULTRASONIC EXCITATION

by

**Zane Ashton Roberts**

**A Dissertation**

*Submitted to the Faculty of Purdue University*

*In Partial Fulfillment of the Requirements for the degree of*

**Doctor of Philosophy**


School of Mechanical Engineering

West Lafayette, Indiana

August 2019

# THE PURDUE UNIVERSITY GRADUATE SCHOOL
# STATEMENT OF COMMITTEE APPROVAL

Dr. Steven F. Son, Co-Chair
School of Mechanical Engineering
Dr. Jeffrey F. Rhoads, Co-Chair
School of Mechanical Engineering
Dr. Weinong W. Chen
School of Aeronautics and Astronautics
Dr. I. Emre Gunduz
Department of Mechanical and Aerospace Engineering, Naval Postgraduate School

**Approved by:**

Dr. Jay P. Gore
Head of the Graduate Program

*To my lovely wife Sarah*

# ACKNOWLEDGMENTS

This research was supported by the Air Force Office of Scientific Research (AFOSR) under program managers Jennifer Jordan and Martin Schmidt through grant no. FA9550-15-1-0102. The content does not necessarily reflect the position or policy of the U.S. federal government, and no official endorsement should be inferred.

My gratitude to Steve Son, who had faith that I would succeed in graduate school and introduced me to the field of energetic materials, my new passion.

Gratitude also to Jeff Rhoads, for his enormous generosity, mentorship, and always making me feel at home in his wonderful research group.

Thank you to Emre Gunduz, Weinong Chen, Terry Meyer, Marisol Koslowski, Marcial Gonzalez, and Stuart Bolton for the illuminating and directing conversations.

A special thanks to my roommates, who doubled as labmates: Trevor Fleck, Jesus Mares Jr., and David Kittell.

Thanks to the labmates, collaborators, and fellow students who helped me along the way. My predecessors who have since left: Sam Alexander, Caroline Baker, Matt Beason, Hatem Belal, Jim Catina, Jocelyn Chu, Narendra De, Humberto Detrinidad, Gabriel Diez, Bryce Geesey, Mike Harr, Sarah Isert, Andy Justice, Nick Kerschen, Trevor Kyle, Andrew McBain, Jake Miller, Luciano Mozzone, Whitney Novotny, Johanna Palsdottir, Niranjan Parab, Raghav Ramachandran, Mario Rubio, Brittney Scifres, Ian Shelburne, Bogdon Tanisou, Matt Tanner, Brandon Terry, Michael Wadas, Daniel Woods, Omar Yehia, and Chris Zaseck.

And my current colleagues and collaborators: Michael Baier, Nikhil Bajaj, Alex Brown, Alex Casey, Wesley Chapman, Kate Clements, Dianne Collard, Shannon Creegan, Nick Cummock, Akshay Dandekar, Josh Dean, Camilo Duarte, Spencer Fehlberg, Matt Gettings, Mateo Gomez, Scott Habermehl, Trey Harrison, Jill Joffe, Rufat Kulakhmetov, Amelia Leenig, Anna Loehr,

Tim Manship, Lindsey May , Monique McClain, Miranda McConnell, Gabe Montoya, Jacob Morris, Allison Murray, Caitlin O'Grady, Metin Ornek, Adarsh Patra, Shane Paulson, Michael Powell, Conor Pyles, Allison Range, Morgan Ruesch, Dakota Scott, Zac Siefker, J.C. Smith-McCaw, Christian Sorensen, Kyle Uhlenhake, Vasant Vuppuluri, Marlon Walls, Eric Westphal, and Jason Wickham.

Thanks to my Boise friends, with whom I enjoyed my vacations back home.

Love to my family Celia, Kevin, Luke, Jenna, the Roberts' and the Voelker's (and Ries', Giddings', Heckelsmiller's, Belveal).

And love to my new family, the Bischoff's (and Smith's).

Praise to God and thanks to my church family which I found at Graduate InterVarsity and City of God.

# TABLE OF CONTENTS

LIST OF FIGURES ..... 8
ABSTRACT ..... 14
1 INTRODUCTION ..... 15
1.1 Motivation ..... 15
1.2 Overview ..... 15
2 BACKGROUND ..... 17
2.1 Hot Spots and the Ignition of Explosives Due to Periodic (Vibrational) Loading ..... 17
2.2 Transducer Near-Field Model ..... 25
2.3 Select Non-Intrusive Temperature Diagnostics ..... 27
2.3.1 Infrared Thermography ..... 27
2.3.2 Second Harmonic Generation ..... 28
2.3.3 Shadowgraphy and Schlieren ..... 31
2.4 Analysis of Variance Methods for Determining Statistically Significant Differences ..... 32
3 PHASE CHANGES IN EMBEDDED HMX IN RESPONSE TO PERIODIC MECHANICAL EXCITATION ..... 35
3.1 Introduction ..... 35
3.2 Experimental Methods ..... 35
3.2.1 Sample Preparation ..... 35
3.2.2 Mechanical Excitation and Second Harmonic Generation Measurement ..... 37
3.3 Results and Discussion ..... 40
3.4 Conclusions ..... 43
4 THE EFFECTS OF CRYSTAL PROXIMITY AND CRYSTAL BINDER ADHESION ON TEMPERATURE IN ULTRASONICALLY EXCITED COMPOSITE ENERGETIC MATERIALS ..... 46
4.1 Introduction ..... 46
4.2 Experimental Methods ..... 47
4.2.1 Sample Preparation and Characterization ..... 47
4.2.2 Mechanical Excitation and Infrared Thermography ..... 49
4.3 Results and Discussion ..... 51

4.4 Statistics ..... 56
4.5 Conclusions ..... 62
5 IN-SITU X-RAY OBSERVATIONS OF ULTRASOUND-INDUCED EXPLOSIVE DECOMPOSITION ..... 64
5.1 Introduction ..... 64
5.2 Experimental Methods ..... 64
5.3 Results and Discussion ..... 66
5.4 Conclusions ..... 71
6 MESOSCALE OBSERVATIONS OF THERMAL DECOMPOSITION OF ENERGETIC COMPOSITES UNDER ULTRASONIC EXCITATION ..... 72
6.1 Introduction ..... 72
6.2 Sample Preparation ..... 72
6.3 Results and Discussion ..... 76
6.4 Conclusions ..... 81
7 HIGH-SPEED MICROSCOPY OF ULTRASONICALLY INITIATED POLYMER BONDED EXPLOSIVES ..... 84
7.1 Introduction ..... 84
7.2 Sample Preparation and Testing Procedures ..... 84
7.3 Results ..... 86
7.3.1 PETN ..... 86
7.3.2 RDX ..... 90
7.3.3 CL-20 Based PBXs ..... 94
7.3.4 HMX ..... 101
7.4 Discussion ..... 104
7.5 Conclusions ..... 107
7.6 Acknowledgements ..... 108
REFERENCES ..... 109
VITA ..... 116
PUBLICATIONS ..... 117

# LIST OF FIGURES

Figure 2.1. Plot of Equations (2.13) and (2.16) showing on-axis near-field normalized pressure while varying the parameters $c$ =1050-1100 m/s, $f$ = 210.5 kHz, and $a$ = 4-5 mm. . 27
Figure 2.2. Dynamic SHG of 500 μm HMX crystals on a hot plate. A 40 kHz, 1064 nm wavelength laser was converted to 532 nm green light. ..... 29
Figure 3.1. An illustration of the final dimensions and casting steps of a short Sylgard sample. 37
Figure 3.2. Representative tall (left) and short (right) samples attached to the piezoelectric transducers. ..... 38
Figure 3.3. Schematic showing the relative positions of the camera and laser. ..... 39
Figure 3.4. Selected frames showing a high reflectance of SHG green light during propagation across one of the embedded β-HMX crystals. ..... 41
Figure 3.5. Plot of intensity versus excitation time at the point of maximum observed SHG light in a region of interest in the video comprising Fig. 3.4. ..... 41
Figure 3.6. Selected frames showing a representative SHG response of a single-crystal transition event. ..... 42
Figure 3.7. Selected frames showing SHG response of embedded HMX crystals which resulted in decomposition. ..... 43
Figure 4.1. Separated triad and debonded-separated triad minimum edge-to-edge separation distances and maximum crystal lengths (three values each per sample) are shown alongside the mean values for all of the samples. Debonded samples were created from a population of ideally pristine samples to achieve approximately the same separation distance and crystal lengths for later statistical analysis. Crystal locations did not change within the binder after debonding, nor were the crystals damaged.. 48
Figure 4.2. Image sequence showing the mechanical debonding of Sylgard binder from the HMX crystals in a debonded-contacting triad sample configuration. The arrow shows an edge of the delaminated area which moved across the surface of a crystal as a compressive force was applied from the top and bottom of the frame. All three crystals were debonded. ..... 49
Figure 4.3. Experimental schematic depicting a contacting triad sample, infrared camera, and the excitation signal generating equipment..... 50

Figure 4.4. Maximum surface temperature rise versus time for 12 samples of each configuration: (a) contacting triad, (b) separated triad, (c) debonded-contacting triad, and (d) debonded-separated triad. For each sample, the temperature was recorded over 4 s for 5 runs and the maximum and minimum temperature rise at any time for each sample are bounded by a patch of 20% opacity. The data for the 12 samples of each set are overlaid on each other, where overlapping patches for samples achieving the same temperature rise with time result in darker hues. Schematics of typical crystals are shown for clarity. ..... 52

Figure 4.5. Infrared thermography image sequences for representative contacting triad, separated triad, debonded-contacting triad, and debonded-separated triad samples with backlit microscope images of crystals superimposed at 25% opacity after 2 s, 3 s, and 4 s. The temperature scale was fixed for each sequence by the temperature field of the final frame. Contacting triad images show a representative intense localized spot of maximum temperature appearing above crystal points of contact. Separated triad images show bulk heating of the sample with no apparent localized heat source. Debonded-contacting triad images show localized heating above a single inclusion location. Debonded-separated triad images show a case with heating from all 3 inclusion locations. ..... 53

Figure 4.6. Dot-box plots of the maximum surface temperature rise at 4 s of excitation for the 4 configurations of contacting triad, separated triad, debonded-contacting triad, and debonded-separated triad. Means at 3.1 °C, 1.0 °C, 6.0 °C, and 5.2 °C, respectively, are represented by a solid diamond. All 5 runs of each of the 12 samples among the 4 sample types are presented. X-axis locations of the dots are arranged by sample number which sometimes results in clusters of data points. Note that these are the last data points from Fig. 4.4. ..... 55

Figure 4.7. Residual estimates of experimental error vs. predicted responses (the overall means as shown in Fig. 4.6, are for separated, contacting, debonded-separated, and debonded-contacting, equaling 1.0 °C, 3.1 °C, 5.2 °C, and 6.0 °C, respectively). The full data set and the 5 test average data set are plotted together. ..... 57

Figure 4.8. Residual estimates of experimental error for both the full data set and the 5 test averaged data set are plotted as crystal adhesion (bonded and debonded) groups. .. 58

Figure 4.9. Residual estimates of experimental error for both the full data set and the 5 test averaged data set are plotted as separation distance (contacting and separated) groups. ..... 59
Figure 4.10. Main effect with dependent variable (maximum temperature rise after 4 s) on the y-axis and two independent variables as the x-axis (crystal separation) and in the legend (adhesion). Note that the lines do not cross, indicating no interaction between degree of adhesion and geometry. The temperature is higher for contacting crystal samples in both the bonded and debonded cases. ..... 60
Figure 4.11. Quantile-quantile plot of sample data versus standard normal. Normality can be assumed because the data are reasonably linear by inspection. ..... 61
Figure 5.1. A diagram and depiction of the X-ray PCI imaging setup at Argonne National Laboratory Advanced Photon Source, beamline 32-ID-B. ..... 65
Figure 5.2. Select frames of a single HMX crystal subjected to ultrasonic excitation recorded at 90 kHz in 1 s bursts. ..... 66
Figure 5.3. Select frames showing the delamination, increased size from phase change, cracking, melting, and thermal decomposition (gas production) of a single HMX crystal under ultrasonic excitation recorded at 80 kHz in 1 s bursts. ..... 67
Figure 5.4. Select frames showing the delamination, increased size from phase change, cracking, melting, and thermal decomposition (gas production) of a single HMX crystal under ultrasonic excitation recorded at 70 kHz in 1 s bursts. ..... 68
Figure 5.5. Select frames of the X-ray PCI of a multi crystal sample imaged from the side during ultrasonic excitation recorded at 20 kHz in 1 s bursts. ..... 69
Figure 5.6. Post-test microscope images of the high-solids loaded HMX sample from Fig. 5.5. Both backlighting and top ring-lighting are shown. A circle is drawn around the area of δ-HMX crystals and a possible site of gas production is identified. ..... 70
Figure 6.1. Recrystallized HMX (a) before agitation in acetone, (b) after 1 min, (c) 2 min, and (d) 3 min. ..... 73
Figure 6.2. Images of representative HMX crystals embedded in Sylgard used in this study. These stills were taken from actual test samples. ..... 74
Figure 6.3. Side view from a FLIR A325sc infrared camera of a pre-delaminated β-HMX sample which transitioned to δ-phase. The transducer is also shown as well as a

white dashed outline around the crystal location. The sample was modified to have a particle embedded 1 mm from the side wall to obtain a more differentiated temperature pattern. This image sequence was used to determine the end time of 15 s, about when heat conducted from the transducer first tangibly influenced the ultrasonically driven heat at the particle location. ..... 76

Figure 6.4. Timelines of events observed for different HMX samples. Another visualization of this data is given in Fig. 6.5. ..... 77

Figure 6.5. Time of events observed during the 15 s duration tests for 15 of each embedded, single crystal HMX samples: (a) β-HMX, (b) pre-δ-HMX, (c) pre-delaminated β-HMX and (d) recrystallized β-HMX. Rounded recrystallized β-HMX had no responses within 15 s. The events beyond initial delamination, phase change, and gas production included re-solidification, melting, and additional gas production before breaking out of the cavity/plane of casting in some cases. Dashed lines represent samples that had no visible delamination before gas production and 'X' data are samples shown in subsequent image sequences. ..... 78

Figure 6.6. Image sequence of the top view of a single, embedded, pre-delaminated β-HMX crystal during excitation. (a)-(b) The delaminated binder moved rapidly against crystal interface, (c)-(d) the β-δ phase change began at the left edge of the crystal, (e)-(f) initial gas production expanded the cavity of casting, (g) gas production ceased and the cavity shrank slightly, and (h) a second gas production event occurred and broke out into the plane of casting. ..... 79

Figure 6.7. Image sequence of the top view of a single, embedded, pre-δ-HMX crystal during excitation. Note the opaque white color of the crystal. (a) The initial δ-phase crystal, (b) first sign of delamination and binder motion, (c) first gas production event, (d)-(e) the cavity shrank and additional surface motion was recorded, and (f)-(h) the second gas production event and growth of the cavity until breakout. ..... 80

Figure 6.8. Image sequence of the top view of a single, embedded, recrystallized β-HMX crystal (sample #3). Note the flat facets, sharp corners, and clear initial appearance of the low-defect crystal. (a) No delamination or movement was observed for approximately 3 s, (b) initial delamination and melting occurred almost simultaneously, (c)-(d) gas was produced which expanded the cavity of casting, (e)

the gas products broke out into the plane of casting, and (f)-(h) after approximately 3 s of additional excitation the crystal melted and produced gas for a second time.... 81
Figure 7.1. Experimental schematic depicting a sample glued on top of a transducer, high-speed camera and light source, and the excitation signal generating equipment. ..... 85
Figure 7.2. The second run of a PETN agglomerate sample recorded at 500 fps with backlighting. ..... 88
Figure 7.3. Recrystallized PETN recorded at 500 fps with backlighting. ‘Before’ and ‘after’ images were taken with a Hirox microscope. ..... 89
Figure 7.4. First and second runs of I-RDX sample 1 at 500 fps with backlighting. ‘Before’ and ‘after’ images were taken with a Hirox microscope. ..... 91
Figure 7.5. Runs 1 and 3 of I-RDX sample 2 at 500 fps with backlighting. ‘Before’ and ‘after’ images were taken with a Hirox microscope. ..... 92
Figure 7.6. Two runs of 500 μm sieved RDX recorded at 500 fps with backlighting. ‘Before’ and ‘after’ images were taken with a Hirox microscope. ..... 93
Figure 7.7. CL-20 agglomerates recorded at 500 fps with backlighting. ‘Before’ and ‘after’ images were taken with top ring-lighting on a Hirox microscope. ..... 95
Figure 7.8. Analysis of the ‘hot spot’ size (outer-ring and inner dark area) and calculated spherical volume as observed from 34 video frames and most notably seen in Fig. 7.7(c)-(d). ..... 96
Figure 7.9. The second run of recrystallized CL-20 sample 1 recorded at 500 fps with backlighting. The ‘Before’ image was taken with backlighting and the ‘after’ image was taken with top ring-lighting on a Hirox microscope. ..... 97
Figure 7.10. Recrystallized CL-20 sample 2 recorded at 500 fps with backlighting. The ‘before’ image was taken with backlighting and the ‘after’ image was taken with top ring-lighting on a Hirox microscope. ..... 98
Figure 7.11. CL-20/TNT cocrystals recorded at 500 fps with backlighting. ‘Before’ image taken with backlighting and ‘after’ image taken with top ring-lighting on a Hirox microscope. ..... 100
Figure 7.12. A grade B class 3 HMX sample recorded at 500 fps with backlighting. Backlight Hirox microscope images are shown as ‘before’ and ‘after’. ..... 101

Figure 7.13. Simultaneous high-speed imaging and IR imaging of a δ-HMX sample with a fixed color scale. ..... 102
Figure 7.14. The accompanying maximum surface temperature plot for the δ-HMX sample from Fig. 7.12. The dashed red lines indicate the 8.106 s high-speed shadowgraphy recording interval which began at first motion with red circles indicating the selected frames. The transducer input was ended at about 20 s..... 103
Figure 7.15. A sample of recrystallized HMX which underwent two runs of testing at 500 fps with backlighting. ‘Before’ and ‘after’ images were taken with a Hirox microscope. ..... 104

# ABSTRACT

Author: Roberts, Zane, A. PhD
Institution: Purdue University
Degree Received: August 2019
Title: Heat Generation Mechanisms in Energetic Composite Materials Under Ultrasonic Excitation
Committee Co-Chair: Steven F. Son
Committee Co-Chair: Jeffrey F. Rhoads

Thermal dissipation of mechanical energy from periodic loading in energetic materials (EMs) leads to the creation of areas of intense, localized heating, called hot spots. The impact and shock conditions for the hot spot initiation of solid explosives have been extensively explored, but little work has focused on high-frequency contact loading. In order to design formulations to address unintentional initiation by mitigating heating in polymer-bonded explosives (PBXs) and other heterogeneous EMs, the mechanisms of heat generation which lead to the thermal initiation of energetic composites under ultrasonic excitation were explored. Heat generation mechanisms which may lead to unintentional initiation were identified through the diagnostic techniques of second harmonic generation (SHG) of δ-HMX (1,3,5,7-tetranitro-1,3,5,7-tetrazocine) crystals; X-ray phase contrast imaging (PCI) performed at the Argonne National Laboratory Advanced Photon Source; infrared (IR) thermography; and optical microscopy. This work concludes with high-speed mesoscale observations of dense layers of PETN (pentaerythritol tetraniterate), CL-20 (hexanitrohexaazaisowurtzitane), RDX (1,3,5-trinitro-1,3,5-triazine), and HMX which were damaged or driven to decomposition under acoustic insult using the non-intrusive imaging technique of shadowgraphy to detect hot spots within the transparent binder. Recommendations are formed which address binder adhesion, energetic material properties, and particle morphology on the vibration sensitivity of a PBX formulation.

# 1 INTRODUCTION

## 1.1 Motivation

The objectives of this work are to develop a detailed understanding of the formation mechanisms and dynamics of 'hot spots' or areas of intense, localized heating which can initiate energetic materials (EMs), such as explosives or propellants. Specifically, it is known that the thermal dissipation of mechanical energy from periodic loading may lead to the creation of hot spots, and in order to design formulations which address unintentional initiation and mitigate heating in polymer-bonded explosives (PBXs) and other heterogeneous EMs, the specific mechanisms of heat generation must be fully explored. Composite energetic materials have been shown to generate heat under certain ultrasonic excitations, sufficient enough to drive rapid reactions. An investigation of hot spots at the mesoscale requires quantifying the temperature (heating rate), size, and spatial distribution of initiation sites using a variety of diagnostic tools and to use statistical methods to investigate the factors driving these rare events. By observing the interaction of particles and polymer binder in simplified composite energetic systems, the fundamental mechanisms of this conversion of mechanical to thermal energy can be identified and quantified. An understanding of the underlying physics of each mechanism can help identify the most influential heating sources at high frequencies (100-1000 kHz) which can be carefully addressed with smart design decisions about binder and particle properties, such as adhesion, stiffness, morphology, porosity, and many others. An improvement in the sensitivity of munitions subjected to periodic insults, such as vibration, seen in both transportation and end-use will lead to safer, more reliable systems with increased capabilities in challenging environments.

## 1.2 Overview

A review of the literature on hot spots and previous vibration sensitivity work on explosives is provided in Chapter 2, as well as background information on the acoustic near-field produced by a transducer and the diagnostics and analysis tools used in these works, such as second harmonic generation (SHG), infrared (IR) thermography, shadowgraph imaging, and the analysis of variance (ANOVA) statistical methods used to analyze the data. Details of SHG experiments on HMX crystals are presented in Chapter 3. The effects of crystal proximity/interactions and

binder adhesion, on the creation of hot spots are presented in Chapter 4. Chapter 5 provides a synopsis of the conclusions from the in-situ X-ray phase contrast imaging experiments performed at the Argonne National Laboratory Advanced Photon Source. Chapter 6 explores HMX morphological effects on heat generation leading to initiation captured with high resolution optical microscopy. Lastly, a variety of energetic crystals with different melting points and morphologies in high solids-loaded mono-layers within a binder under ultrasonic insult are discussed in Chapter 7. Hot spots in these samples are captured with high-speed shadowgraphy and the applicability of knowledge to formulation design gained from studying the physics of single crystal configurations is addressed.

# 2 BACKGROUND

## 2.1 Hot Spots and the Ignition of Explosives Due to Periodic (Vibrational) Loading

The initiation of solid explosives, and in particular polymer-bonded explosives (PBXs) consisting of energetic crystals in a binder matrix, is commonly considered to be thermal in origin and energy from mechanical, electrical, or chemical processes, for example, can be dissipated as heat to form 'hot spots' [1–4]. Once formed, hot spots either lead to exothermic reaction, or fail to create an initiation site due to thermal diffusion [5]. In other words, a hot spot will grow provided that the rate of heating from both mechanical insult and chemical reaction at the small volume is greater than the heat lost to the surroundings [6]. Impact-induced hot spots have been estimated to be 0.1-10 μm in diameter with durations of around $10^{-5}$-$10^{-3}$ s and exhibit temperatures of approximately 400-500 °C [2, 6–9]. Others have estimated the size and critical temperature of hot spots ranging from impact-induced to shock-induced loading to span 0.1-1000 μm in diameter, inversely corresponding to 527-1527 °C in $10^{-8}$-$10^{-1}$ s. Hot spot durations and temperatures are also known to be material dependent [5]. Of particular note, hot spots can be formed on longer timescales and slower heating rates during high-frequency periodic loading, which is the focus of this current work.

PBXs have exhibited localized heating and, in some cases, subsequent reaction in response to ultrasonic excitation. The objectives of this work are to visualize hot spots in real-time using the techniques of second harmonic generation (SHG), infrared (IR) thermography, optical microscopy, and high-speed videography with both X-ray phase contrast imaging (PCI) and in the visible spectrum to quantify the effects of various crystal and binder configurations subjected to ultrasonic excitation and to elucidate the underlying heat generation mechanisms. In a review by Field [2], ten hot spot ignition mechanisms were proposed:

(i) adiabatic compression of trapped gas spaces;

(ii) other mechanisms involving cavity collapse, such as viscous or plastic heating of the surrounding matrix material or, for very high shock collapse pressure, hydrodynamic shock focusing;

(iii) friction between sliding or impacting surfaces, or between explosive crystals and/or grit particles in an explosive;

(iv) localized adiabatic shear of the material during mechanical failure;

(v) viscous heating of material rapidly extruded between impacting surfaces;

(vi) heating at crack tips;

(vii) heating at dislocation pileups;

(viii) spark discharge;

(ix) triboluminescent discharge; and

(x) decomposition, followed by Joule heating of metallic filaments.

Note that this list contains insults/mechanisms from many different stimuli and may not be comprehensive. The key mechanisms of energy conversion to heat during *periodic, mechanical loading* are most likely: (i) the adiabatic compression of trapped gas spaces (voids); (ii) viscoelastic or viscoplastic dissipation in the polymer binder; (iii) friction from sliding or impacting surfaces, especially at the crystal/crystal or crystal/binder interfaces; (iv) the shear of the material during mechanical failure; (v) viscous heating of material rapidly extruded between impacting surfaces; and (vi) the fracture of crystals or binder leading to additional friction. There is an underlying difficulty in separating the effects of each of these on the overall response and temperature rise of a system. For example, in PBX systems, heating could manifest at crack tips of a mechanically failing crystal and subsequent friction at crystal/crystal interfaces or adiabatic compression of the spaces opened due to the crack could continue to reinforce the hot spot. Also, the delamination (debonding) of the polymer binder from crystal surfaces due to poor adhesion or excessive strain from wave interaction or from viscoelastic heating induced thermal expansion creates more heat dissipation pathways. Other mechanisms such as frictional heating from a slapping or sliding binder at the crystal/binder interface can be activated in addition to such viscoelastic heating, as heat conduction weakens when the binder is periodically out of contact with the crystal. Amplified viscoelastic heating from a large amplitude binder motion may still be competing with frictional heating. These fatigue processes that take place in solids under vibrational insult result in a change of strength, plasticity, and external and internal friction [10].

Insult is defined as an action which imparts, with reference to the pristine or starting state of an energetic material, a morphological change or change in mechanical properties (damage), which may cause a change in performance or lead to accidental ignition [11]. Insult can be both mechanically or thermally dominated but these categories are always coupled; for example,

mechanical damage such as shearing and friction cause heat dissipation and melting at the mesoscale interface. Likewise, thermal damage such as expansion from heating can exert stresses outward and result in cracking which is more typical of mechanical insults [11].

The compression of trapped gas spaces and friction from sliding or impact have been considered to be the main contributing internal heat generation mechanisms leading to the formation of hot spots. The dropweight impact on crystals arranged in an annulus showed initiation from the center where compression of trapped gas creates hot spots, as do cavities collapsing from a shock wave [2, 12–14].

Investigations into the key heat dissipation mechanism of frictional heating have examined the minimum melting temperature of hard grit particles necessary to initiate the solid explosive pentaerythritol tetranitrate (PETN) during impact or rapid shearing to be greater than 430 °C [3, 4, 8, 9]. High melting temperature, high hardness grit particles (both higher than that of PETN) are necessary because frictional heating reduces once melting occurs at the surface [11].

If extreme conditions exist such that there is sufficient temperature rise, such as very high impact energy, viscous heating of a flowing, plastically deforming solid explosive or binder can create hot spots [8, 9]. High cyclic loading rates can generate the necessary heat to reach a critical temperature in the binder or at crystal interfaces, leading to the thermal decomposition of HMX (1,3,5,7-tetranitro-1,3,5,7-tetrazocine) and RDX (1,3,5-trinitro-1,3,5-triazine) explosive crystals [15–17]. The models of compressional plane waves interacting with a rigid, spherical HMX inclusion showed that viscoelastic heating on short timescales can approach the same order of heating (55 °C/s) [18] as situations considered to be frictional [19].

There is a need to identify the most significant heat generation mechanisms in PBXs subjected to ultrasonic insult, because hot spot formation in these systems is poorly understood. Such knowledge about particle/particle [1] and particle/binder [19] interaction is important for future design considerations, identifying the most important physics to capture in associated modeling efforts [18], and to help predict hot spot temperatures, locations, and sizes. Direct experimental access to the microscale processes is challenging, so experiments in simplified configurations can help isolate different phenomena [17] and allow appreciable access.

PBXs and composite energetic materials of interest are composed of explosive crystals embedded in an elastomeric binder, commonly hydroxyl-terminated polybutadiene (HTPB),

Sylgard (polydimethylsiloxane), or Estane 5703 [20–23] as in the ubiquitous PBX 9501. PBX 9501 consists of 95% HMX, 2.5% Estane, and 2.5% BDNPA/F. This formulation contains a bi-modal distribution of HMX particle sizes. A typical failure path under compression has been identified as large crystal detachment from the finer-grained material and binder [24].

In investigations of particle and binder interaction during periodic deformation, the extremely complex structure of a PBX has recently been simplified to discrete crystal inclusions within blocks of polymer binder. Mares *et al.* [16] established experiments in which contact piezoelectric transducers run at ultrasonic frequencies (~200 kHz and ~1 MHz), were used to excite a Sylgard 184 elastic binder system with discrete embedded energetic crystal and inert inclusions, while the surface temperature was observed via infrared thermography. Both ammonium perchlorate (AP) and HMX embedded particles were driven to chemical decomposition [15, 16] and a range of frequencies were investigated [16, 25]. A subsequent study by Miller *et al.* [26] examined the impact of AP crystal morphology on the transient thermal responses of embedded single crystals in a similar ultrasonic system. Heat generation rates were estimated by fitting the maximum surface temperature response to an analytical solution for a point heat source at a given depth d in a semi-infinite conductive medium given by

$$T_s(t) = \frac{q}{2\pi k d}\, erfc\left(\frac{d}{\sqrt{4\alpha t}}\right), \tag{2.1}$$

where $T_s$ is the increase in surface temperature, q is the heat generation rate, k and α are the thermal conductivity and diffusivity of the medium, respectively, *erfc* is the complementary error function, and t is the time elapsed since initiating heat generation through ultrasonic insult. A statistically significant difference in the probability for significant heating was found between the heat generation rates of spherical crystals as compared to highly irregular crystals and two primary mechanisms of energy conversion to heat were proposed. The first was a weak heating associated with the viscoelasticity of the surrounding binder [18] and the second was a stronger interfacial heating potentially due to higher stress concentrations at surface asperities or from frictional heat generation at a delaminated and vibrating interface.

Temperature rises from viscoelastic heat generation have been investigated theoretically for a rigid HMX sphere in Sylgard 184 subjected to high frequency compressional plane waves [18]. Analytical stress and displacement solutions were modified to account for viscoelastic effects of the medium surrounding the inclusion and significant heating of approximately 55 °C/s was predicted even in the absence of voids or delamination at the particle interface. This model,

however, was only expected to be adequate for the first few seconds of excitation. Mares *et al.* [18] conclude that viscoelastic heat generation can be at least comparable to frictional heat generation.

Systems of RDX/Sylgard 182 and sucrose/HTPB with countable inclusions have also been investigated thermally while subjected to high-amplitude, high frequency acoustic insult (20 kHz) and have shown preferential heating at certain crystals within the field of an ultrasonic horn [27]. The boundary conditions of this experiment consisted of a thin sample ~1.5 mm thick, clamped under a static pressure. Additionally, ultrasound was shown to selectively heat the compliant polymer binder adjacent to rigid crystal surfaces. Two possible explanations for this were given as stress from a significant acoustic impedance mismatch and frictional heating of the moving polymer surface, demonstrating that adhesion may be an important property of the binder. Furthermore, You *et al.* [28] continued with an examination of crystals coated in a solid film of polytetrafluoroethylene (PTFE) or liquid polyethylene glycol (PEG) in Sylgard 182 which served to delaminate the particle-polymer interface, causing frictional heating attributable to the relative motion between the two components during ultrasonic excitation. Sites of delamination of the solid inclusions generated intense hot spots within the polymer matrix.

Men *et al.* [29] exploited this fact to predictably capture the onset of thermally induced explosion of single HMX and RDX crystals and found that reactive gases expanded a cavity within the polymer and subsequently ignited in a ‘second stage’ due to the partial confinement provided by the binder, concluding that mechanical processes in the surrounding medium influence the chemical kinetics of explosions.

In the initial attempts to explore heat generation and temperature profiles in high-solids loaded rectangular and cylindrical composites, under the auspices of raising the temperature and thus the vapor pressure of the explosive for enhanced remote detection, mock explosives of ammonium chloride ($NH_4Cl$) in HTPB have been tested at lower frequencies (broadband white noise 10-1000 Hz) as the thermal and mechanical response of the samples were recorded [30–33]. One such experiment measured the steady-state temperature response over 60 min trials compared to a viscoelastic model. The mechanical response of the plates was recorded via scanning laser Doppler vibrometry. Three ratios of particles to binder were used: 50% , 65%, and 75% volume ratio [31]. Rapid heating occurred at internal and external defects in the plates. Heating appeared to be maximized for highly viscous materials, shown with 50 % solids loaded

plates, but high levels of heating were also observed in the pristine 75% solids loaded plates. These heating levels were above those predicted by the viscoelastic model. Likely, this was due to particle/particle interactions which may lead to significant stress concentrations, and a similar effect has been observed at ultrasonic frequencies testing a PBX 9501 cylinder [25]. Fixing the solids at 75% $NH_4Cl$ by volume, multiple excitation levels on a beam were also explored [30]. Classical beam theory accompanying a viscoelastic model predicted results consistent with the experiment and revealed a strong dependence of the thermal response on the stress and strain fields produced within the beam coupled with convection at the surfaces, which was shown to impact the thermal response.

More recently, mock explosive plates better approximating a standard PBXN-109 formulation have been tested to highlight the influence of thermal boundary conditions and formulation variation on the thermomechanical behavior of the particulate composite plates [34]. PBXN-109 consists of (by weight), 64.00% RDX, 20.00% Al, 7.346% HTPB, 7.346% dioctyl adipate (DOA, a plasticizer), 0.10% antioxidant 2246, 0.26% Danntocol DHE (a binding agent), 0.02% triphenylbismuth (TPB, the cure catalyst), and 0.95% isophorone diisocyanate (IPDI, the curative) [23]. The RDX constituent was replaced with an appropriately sieved range of sucrose particles. The plates were prepared with 85% solids loading varying the aluminum content by 0%, 15%, and 30% weight ratios. The increased aluminum content did not result in drastically increased heat generation. Additionally, an insulated boundary condition resulted in an expected temperature increase, and it was posited that bulk-scale heat transfer models did not account for this increase and that the trends are likely attributable to the particulate composite nature of the material [34].

The use of Sylgard in PBXs [35, 36] prompted a study by Elbeih *et al.* [37] which examined the mechanical sensitivities of 15 wt-% Sylgard 184 composites as compared to both loose crystals and select commercially available PBXs with differing binders. A large increase in impact energy and friction sensitivity was found for the 50% initiation threshold in dropweight and BAM (German Bundesanstalt für Materialprüfung Apparatus) friction tests [38] on RDX, HMX, and hexanitro-hexaazaisowurtzitane (CL-20) prepared Sylgard PBXs when compared to the same volume of pure explosive counterparts [37]. The use of Sylgard binder served to absorb the impact energy and decrease the shear forces between explosive particles during testing. Additionally, the sensitivity to impact and friction was decreased to a range lower than the three

tested commercially available PBXs. Studies such as these, which focus on certain properties of the binder to reduce sensitivity to shock and friction at the expense of adhesion may be misleading in some cases. A more important consideration could be the choice of binder and the adhesion to the particles to mitigate hot spot formation or damage from high frequency loading as potentially seen during transportation.

Sensitivity to impact and friction and other thermal and mechanical insults are heavily studied, however, the data on the vibration sensitivity of explosives are sparse and there have been few attempts to create a comprehensive function of initiation criteria. In the context of vibration of a solid explosive, both intermittent-contact and constant-contact cyclic loading forces have been studied [10]. The vibration sensitivity of explosives has been fit to a function of the material parameters and one type of vibration device in Loginov [10]

$$W_i = U\left(f, A, a, P_{dyn}, \frac{P_{dyn}}{P_{st}}, Q, t\right), \tag{2.2}$$

where $W_i$ (an upper limit of 100%) is the probability of explosion (later amended to degree of decomposition), a function of frequency *f*, amplitude *A*, acceleration *a*, dynamic load $P_{dyn}$, the ratio of the dynamic and static loads $P_{dyn}/P_{st}$, the vibration energy absorbed by the sample $Q$, and the total time of vibration $t$ (also amended in a later work by Loginov) [39]. Vibration sensitivity cannot be characterized by a single quantity because of the complicated relationship of impact and friction sensitivity. These tests were less than 30 s and performed at low frequencies in the range of 50-150 Hz. A variation of the frequency, amplitude, dynamic versus static load, and acceleration on five types of explosives showed an increase in the probability of explosion for all four increasing parameters. The tested explosives included fulminating mercury, lead azide, PETN, HMX, and RDX.

It was confirmed that the sensitivity of an explosive is higher under intermittent contact conditions ($P_{dyn}/P_{st} > 2$) than under constant contact conditions ($P_{dyn}/P_{st} < 2$) because the energy distributions in the sample are more non-uniform as are the force loading cycles. For low melting point explosives such as tetryl and trinitrotoluene (TNT), the full range of parameters cannot be explored because they flowed out of the test rig, melting at sufficiently high temperatures. Explosions began at lower parameters when using a test rig with a narrow hole into which particles could disperse and squeeze, therefore receiving more mechanical activation. The difference in strain rate, localized deformation, and non-uniformity of the stress distribution can account for the difference in sensitivity despite having the same energy input in different test

rigs. Each of the aforementioned mechanisms can contribute to the absorbed energy of the sample through many pathways and, over the time it is vibrating, work to accelerate its thermal decomposition.

Loginov also examined the criteria for estimation of an explosion hazard of high explosives (HEs) being manufactured or processed [39]. The deformation and thermal processes in heterogeneous solid and liquid explosives are localized on defects in crystal structure in solid HEs and in gas bubbles in liquid HEs [39, 40]. When analyzing an HEs sensitivity to vibration, sensitivity tests such as impact, fast shear, and long-term friction are unsuitable for direct correlation because these methods do not capture the physics seen in periodic loading such as periodic stress and deformation variation, the long timescales of the process, and small duration of each loading cycle [39]. Equation (2.2) was later amended with the time variable, and it also proved more expedient to use the degree or rate of decomposition as a criteria rather than the probability of explosion $W$ [39]. Safety coefficients were given considering the ignition temperature, energy imparted to the sample from vibrational processing (calculated from the frequency, eccentric mass of the electromechanical vibrator, and amplitude), and mass of the explosive.

The unsuitability of common sensitivity tests to predict the response of energetic materials to vibration/acoustic insult points to the need for a standardized vibration sensitivity test for munitions. However, even standard methods for determining explosive sensitivity which include dropweight impact (glass or steel anvil), electrostatic discharge (ESD), and BAM friction tests [41] are unrepeatable at different times and locations even with the same material. A collaborative paper from 3 U.S. Department of Energy laboratories and 2 U.S. Department of Defense laboratories (Lawrence Livermore National Laboratory; Los Alamos National Laboratory; Sandia National Laboratories; Naval Surface Warfare Center, Indian Head; and Air Force Research Laboratory, Tyndall Airforce Base) show large variations in testing among homemade and commercial explosive materials which were distributed from the same batch, some differences of which are significant from a safety standpoint. Most of the reasons for the nature of these differences are not well defined and this highlights the difficulty of small-scale safety testing and reporting sensitivity for what ideally should have been standardized tests. Linking dropweight sensitivity to vibration sensitivity is an active area of research [42]. It appears that in certain ultrasonic horn tests, the temperature profiles compared to dropweight can

be of similar durations, however, the rise time is much faster with dropweight and the peak temperatures are higher with ultrasound.

While it may not be possible to create a comprehensive function of parameters governing the initiation of a solid explosive due to vibration [10], it is possible to identify the most important heat generation mechanisms in certain situations and suggest practical formulation choices to minimize heating of an explosive under different regimes of periodic excitation (amplitude and frequency) and compare the results to more standardized tests, such as dropweight impact.

## 2.2 Transducer Near-Field Model

The current work will focus on the insult derived from a contact piezoelectric transducer operating at 210.5 kHz upon 'simplified' PBXs consisting of energetic crystals within a block of polymer binder. Thus, examination of acoustics and wave propagation in the near-field will facilitate understanding. In the following discussion, the wavelength λ of a material is defined as

$$\lambda = \frac{c}{f}, \tag{2.3}$$

where c is the wavespeed, *f* is the frequency in Hz, and wavenumber k is defined as

$$k = \frac{2\pi}{\lambda}. \tag{2.4}$$

Radiation from a plane circular piston approximates a transducer surface and a derivation from Kinsler *et al.* [43] of the near-field pressure follows. If the radiating surface of the piston moves uniformly with normal speed

$$U_0 e^{j\omega t}, \tag{2.5}$$

where ω is the frequency in rad/s, t is time, and j indicates a complex number, the pressure field can be obtained by a summation of infinitesimal elements of a surface, each acting as a baffled simple source of strength

$$dQ = U_0 dS. \tag{2.6}$$

For a simple source 'baffled' by a plane of infinite extent where the source is on or near a rigid boundary, the pressure amplitude will be twice that of a source in free space. The pressure generated by one of these elements is given by

$$P = \frac{\rho_0 c Q}{\lambda r}, \tag{2.7}$$

where $r$ is the distance from the source and $\rho_0$ is the density of the fluid. Including time variations,

$$P(r,t) = j\rho_0 c \frac{Q}{\lambda r} e^{j(\omega t - kr)}. \tag{2.8}$$

Thus, the total pressure is

$$P(r,\theta,t) = j\rho_0 c \frac{U_0}{\lambda} \int_S \frac{1}{r'} e^{j(\omega t - kr')}\, dS, \tag{2.9}$$

where r′ is the distance from the element $dS$ to the field point. This is difficult to solve for a general field point, but can be solved along a line perpendicular to the face of the piston along its center axis in the near-field as well as in the far-field. The axial response in the near field at $\theta = 0°$ for a piston of radius a, where $\sigma$ is the distance from the center face of the piston to the point $dS$ on its face, and $r$ is the distance from the center of the piston to the point:

$$P(r,0,t) = j\rho_0 c \frac{U_0}{\lambda} \int_0^a \frac{e^{-jk\sqrt{r^2+\sigma^2}}}{\sqrt{r^2+\sigma^2}} 2\pi\sigma dS. \tag{2.10}$$

Since the integrand

$$\frac{\sigma e^{-jk\sqrt{r^2+\sigma^2}}}{\sqrt{r^2+\sigma^2}} = -\frac{d}{d\sigma}\left(\frac{e^{-jk\sqrt{r^2+\sigma^2}}}{jk}\right), \tag{2.11}$$

is a perfect differential, the complex acoustic pressure is

$$P(r,0,t) = \rho_0 c U_0 \left\{1 - e^{-jk\left(\sqrt{r^2+a^2}-r\right)}\right\} e^{j(\omega t - kr)}. \tag{2.12}$$

The pressure amplitude along the piston axis is the magnitude of the above expression,

$$P(r,0) = 2\rho_0 c U_0 \left| sin\left\{\frac{1}{2} kr \left[\sqrt{1+\left(\frac{a}{r}\right)^2} - 1\right]\right\}\right|. \tag{2.13}$$

The axial pressure exhibits strong interference effects and the pressure extremes occur for values of $r$ inside the sine term satisfying multiples of $\pi/2$,

$$\frac{1}{2} kr \left[\sqrt{1+\left(\frac{a}{r}\right)^2} - 1\right] = m\frac{\pi}{2}. \tag{2.14}$$

Solution for $r$ yields

$$\frac{r_m}{a} = \frac{a}{m\lambda} - \frac{m\lambda}{4a}. \tag{2.15}$$

Which is also commonly given as the first maximum approaching the piston

$$r_1 = \frac{a^2}{\lambda} - \frac{\lambda}{4}. \tag{2.16}$$

This maximum is considered the end of the near-field as the pressure amplitude begins to decrease with $1/r$ dependence. Equations (2.13) and (2.16) are plotted in Fig. 2.1. The speed of

sound material property was chosen to be approximately that of Sylgard 184, around 1100 m/s, and the frequency and piston radius to be that of a Steiner and Martins, Inc. SMD10T2R111 transducer [44, 45]. The plot shows that for these parameters, only a single maxima is expected which varies around ~2-4 mm. A lower sound speed lengthens the distance of the first maximum, while a smaller transducer radius shortens the depth of the first maximum. Note that for a transducer attached to a viscoelastic block, the acoustic field can be complicated by non-propagating waves, shear waves, the finite nature of the block, the off-axis field, and non-normal (radial) behavior of the transducer.

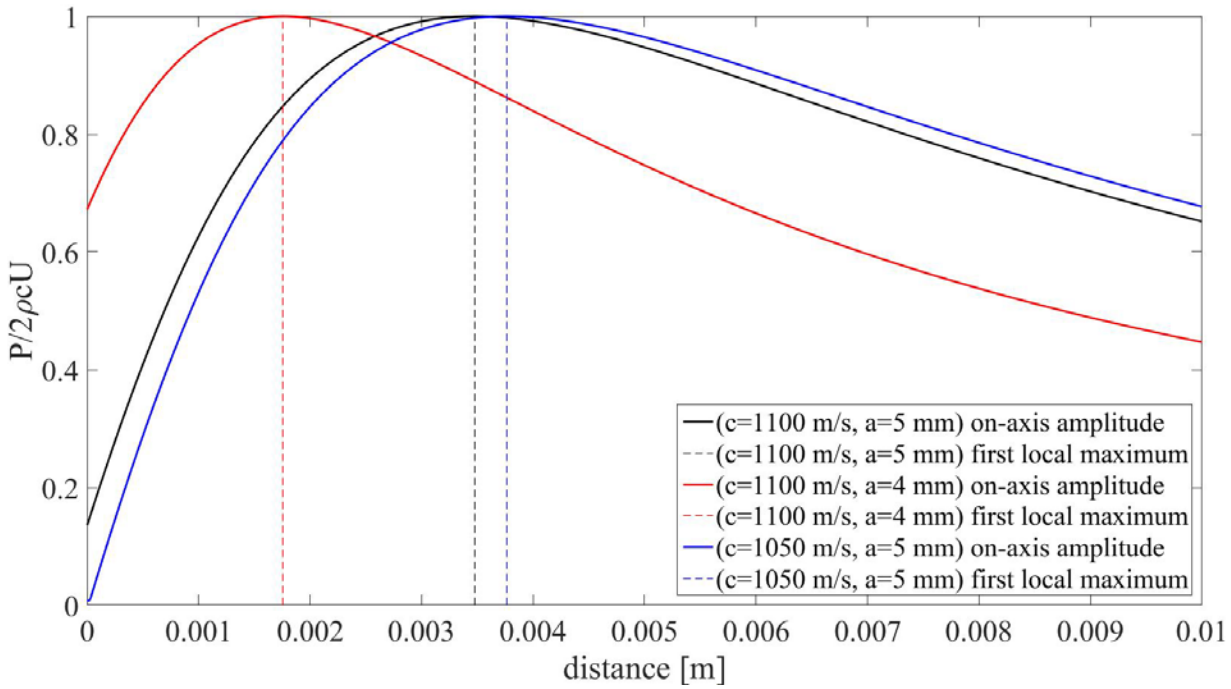


Figure 2.1. Plot of Equations (2.13) and (2.16) showing on-axis near-field normalized pressure while varying the parameters $c$ =1050-1100 m/s, $f$ = 210.5 kHz, and $a$ = 4-5 mm.

## 2.3 Select Non-Intrusive Temperature Diagnostics

### 2.3.1 Infrared Thermography

Hot spots are inherently difficult to observe and characterize due to their transient nature. Particular hurdles involve taking measurements at extremely high temperatures and pressures, and making observations at very small timescales and spatial locations. Temperature is one of the most difficult measurements to make accurately due to the small timescales, high heating

rates, and small spatial locations involved. IR imaging has been used as a non-intrusive temperature measurement to view hot spots from sand grit on a spinning surface [46] and impact induced initiation from grit friction [47]. Recently, hot spots have been observed using IR imaging in energetic systems that were excited via high-frequency, ultrasonic excitation [16, 25, 26, 28, 40]. Such excitation appears to be useful for improving the understanding of hot spot generation at longer timescales than those commonly seen in short-duration shock events. Limitations of this technique are that the temperature field can only be measured at a surface, typically above or below the embedded particles (not at the true particle location), and that reflections from the environment and emissivity of the surface under consideration must be taken into account. For example, in Mares *et al.* [16] and Miller *et al.* [26], the surface of the polymer binder was coated in soot from a candle to achieve an emissivity close to 1, and it is the author's opinion that this operation unintentionally created delamination sites on the crystal/binder interfaces in some samples due to the imposed temperature gradient. Other non-intrusive temperature indicators would be helpful in such experiments as they can help validate IR thermography measurements.

### 2.3.2 Second Harmonic Generation

At room temperature, the most stable and dense polymorph of HMX is the β-phase [20]. β-HMX crystals transform from a centrosymmetric to a non-centrosymmetric δ-phase when heated above ~170 °C. A laser source can interfacially or volumetrically generate frequency doubled light because of the nonlinear optical properties of the δ-phase crystal; this phenomenon is called second harmonic generation (SHG) [48–51]. SHG was first observed in HMX by Henson *et al.* [49] and has since been successfully used in a number of studies as a δ-phase indicator [21, 52, 53]. Dickson *et al.* [46] experimented with PBX 9501 with ordinary sand normally loaded against a transparent sliding disk. The samples were later probed via SHG, which found that some HMX had transitioned from β-δ phase, indicating that 170 °C had been met or exceeded during the experiment. Decomposition had also occurred in the vicinity of the embedded grit particles, as had melting. The dynamic use of SHG may provide new time-resolved information of the state of individual energetic crystals. As an *in situ* imaging technique implemented during ultrasonic experiments, SHG serves as an indirect temperature marker capable of revealing the localization of energy in energetic crystals. Figure 2.2 shows SHG of

HMX crystals which were captured by the author while transitioning on a hot plate just before a reduction of signal from melting.

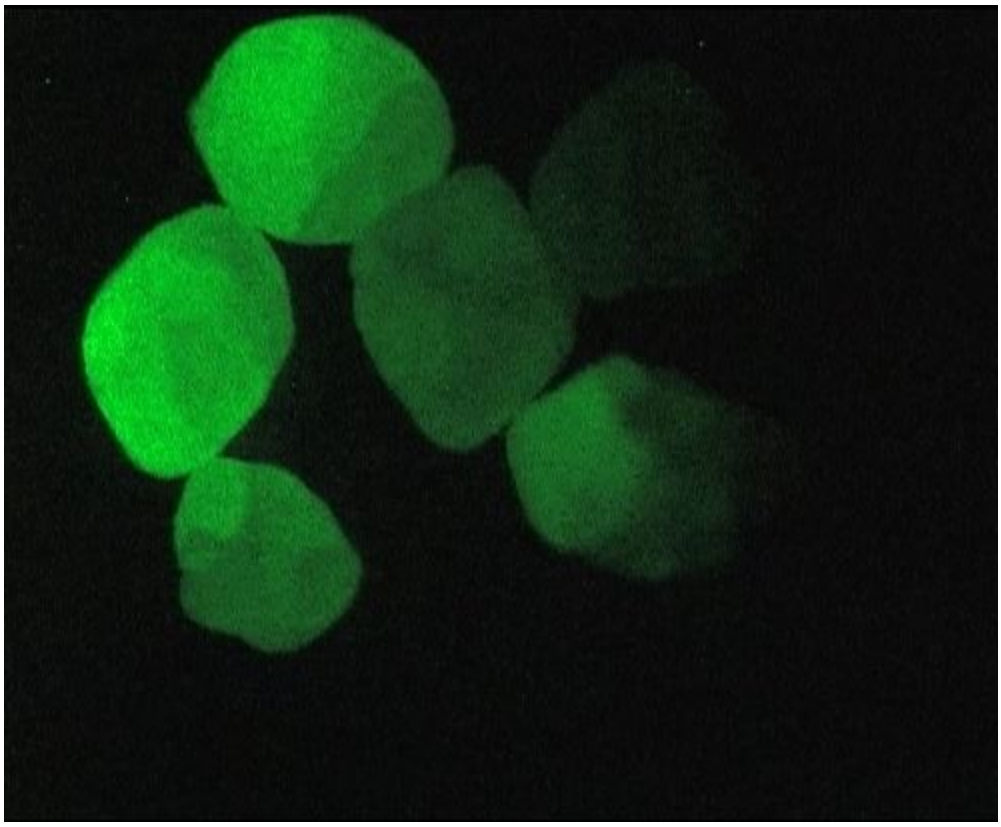

Figure 2.2. Dynamic SHG of 500 μm HMX crystals on a hot plate. A 40 kHz, 1064 nm wavelength laser was converted to 532 nm green light.

While SHG techniques have been used in dropweight experiments of δ-HMX containing materials [52, 53] and in slow heating experiments of single crystals to investigate the nitroplasticiser influence on nucleation rate [21], they are yet to be used to investigate the interaction among various explosive crystals and/or any surrounding binder material under periodic insult, which is a key component of hot spot generation [1]. Given the crucial need to investigate possible frictional or viscoelastic heating mechanisms at crystal/crystal and/or crystal/binder interfaces for PBX munitions undergoing mechanical deformation, the author's work seeks to observe how hot spots created by ultrasonic excitation affect crystals embedded within a binder and to verify IR thermography measurements via the indirect temperature markers of both phase change and decomposition.

It was noted in prior work that individual crystals should have no geometric features,

such as cracks or microinclusions, whereat initial phase change nucleation can be specifically pinpointed [20, 21]. As such, care should be taken when drawing conclusions about hot spot locations from SHG origination on a single crystal. However, it is possible to better understand the underlying physics of an experiment from the observation of crystal phase transitions when considering the inclusion positions and duration of insult (excitation).

First demonstrated by Franken *et al*. [54] and famously, or infamously, copy edited out, SHG is presented following the derivation by Pedrotti *et al.* [55]. The polarization $\vec{\boldsymbol{P}}$ of a linear medium by an electric field $\vec{\boldsymbol{E}}$ is given by,

$$\vec{\boldsymbol{P}} = \varepsilon_0 \chi \vec{\boldsymbol{E}}, \tag{2.17}$$

where $\varepsilon_0$ is the vacuum permittivity (electric constant) and $\chi$ is the susceptibility. With small departures from linearity, the susceptibility can be written using a Taylor series expansion

$$\chi = \chi_1 + \chi_2 E + \chi_3 E^2 + \cdots, \tag{2.18}$$

and the polarization is thus

$$P = \varepsilon_0(\chi_1 E + \chi_2 E^2 + \chi_3 E^3 + \cdots), \tag{2.19}$$

or

$$P = P_1 + (P_2 + P_3 + \cdots). \tag{2.20}$$

Second harmonic generation results from the first of the small, nonlinear terms

$$P_2 = \varepsilon_0 \chi_2 E^2, \tag{2.21}$$

in which the second-order polarization term is proportional to the square of the electric field. This term makes no contribution to polarization in an isotropic optical material or a centrosymmetric material (one having a center of symmetry such as β-HMX). For example, if an inversion center is present, that is, if the radial coordinate *r* is changed to *-r*, the atomic arrangement of the crystal remains unchanged and responds the same way to the applied field except for a change in sign

$$P_2 = \varepsilon_0 \chi_2 (+E)^2 \quad \text{and} \quad -P_2 = \varepsilon_0 \chi_2 (-E)^2. \tag{2.22}$$

Because the electric field is squared, $P_2 = -P_2$ which can only be true if $P_2 = 0$. For a non-centrosymmetric medium, such as δ-phase HMX, subjected to an electric field

$$E = E_0 \cos \omega t, \tag{2.23}$$

where ω is the frequency. The second-order polarization term becomes

$$P_2 = \varepsilon_0 \chi_2 {E_0}^2 cos^2 \omega t = \varepsilon_0 \chi_2 {E_0}^2 \left[\frac{1}{2}(1 + cos 2\omega t)\right], \tag{2.24}$$

after substitution of the double-angle trigonometric identity. Finally,

$$P_2 = \frac{1}{2}\varepsilon_0\chi_2{E_0}^2 + \frac{1}{2}\varepsilon_0\chi_2{E_0}^2 cos(2\omega t), \tag{2.25}$$

shows a term dependent on double the frequency, or equivalently, half of the wavelength.

### 2.3.3 Shadowgraphy and Schlieren

Shadowgraphy is closely related to Schlieren imaging techniques and is a way to non-intrusively capture high contrast images of temperature gradients or other density changes (manifested as changes in refractive index) within a transparent solid or fluid [56–59]. Unlike Schlieren, shadowgraph techniques require no knife edge to cutoff a portion of the refracted light after passing through lenses or mirrors. Shadowgraphy is less sensitive than Schlieren methods, but have been used to great extent because of their simplicity of implementation. Shadowgraphy requires no more than a point light source with an optional lens for a parallel beam and a flat screen on which the image is projected, rather than producing a focused image. Shadowgrams are known to produce more dramatic images in special cases such shock waves, even though it is less sensitive in general [56]. This is attributable to the response of shadowgraphy to the second spatial derivative (Laplacian) of the refractive index

$$\frac{\partial^2 n}{\partial x^2}, \frac{\partial^2 n}{\partial y^2}. \tag{2.26}$$

The refractive index is given as $n=c/v$ where n is the refractive index, c is the speed of light in a vacuum, v is the local light speed, and x and y are the spatial Cartesian directions. Conversely, Schlieren imaging illuminance levels respond to the first spatial derivative of the refractive index

$$\frac{\partial n}{\partial x}, \frac{\partial n}{\partial y}. \tag{2.27}$$

Shadowgraphy displays ray displacement while Schlieren displays the deflection angle ε.

Below is a calculation of the light-ray deflection by a refractive index gradient ($dn/dy$) [56]. A planar light wave propagating in the z-direction is refracted at an angle $\Delta\varepsilon$ covering a distance in time $\Delta z/\Delta t$. The equation

$$\Delta\varepsilon = \frac{v_2\Delta t - v_1\Delta t}{\Delta y} = \frac{\frac{c}{n_2}\Delta t - \frac{c}{n_1}\Delta t}{\Delta y}, \tag{2.28}$$

follows. Combined with the expression for time

$$\Delta t = \Delta z\frac{n}{c}, \tag{2.29}$$

we arrive at

$$\Delta\varepsilon = \frac{n}{n_1 n_2}\frac{(n_1 - n_2)}{\Delta y}\Delta z. \tag{2.30}$$

As the finite differences approach zero, $n_2$-$n_1$ becomes $\Delta n$, and $n/(n_1 n_2)$ simplifies to $1/n$

$$\frac{d\varepsilon}{dz} = \frac{1}{n}\frac{dn}{dy}. \tag{2.31}$$

Using the small angle approximation $d\varepsilon = dy/dz$

$$\frac{\partial^2 y}{\partial x^2} = \frac{1}{n}\frac{dn}{dy}. \tag{2.32}$$

Which relates the curvature of a refracted ray to the refractive index gradient and Schlieren images can be found by integrating the ray curvature in the following way,

$$\varepsilon_y = \frac{1}{n}\int \frac{\partial n}{\partial y} dz. \tag{2.33}$$

For a 2-D object of thickness L in the z-propagating direction (and refractive index varying in the y-direction), the angle of deflection is

$$\varepsilon_y = \frac{L}{n}\frac{\partial n}{\partial y}. \tag{2.34}$$

So the gradient of the refractive index is responsible for the angle of ray deflection, not the index itself, and for a high density area light rays deflect toward the center, while for a low density (decreasing refractive index) region where a hot spot exists in a transparent binder, light rays will deflect away making a darker image.

## 2.4 Analysis of Variance Methods for Determining Statistically Significant Differences

Hot spots are inherently random events with great dependence on local porosity, morphology, interfacial damage, non-uniformity of the insult, and many other conditions, therefore, the use of statistics can help draw meaningful conclusions about important PBX property information which could reduce heating in response to ultrasonic excitation and to aid in future design decisions [19]. Phenomenologically guided work can benefit from large sample sizes with controlled variations, or ‘treatments’ and statistically significant differences can be identified with analysis of variance (ANOVA) which will be done in Chapter 4.

Residuals should first be examined to determine if the model has a good fit. The residual is

$$Res = y - \mu, \tag{2.35}$$

where y is an observed value in one of the treatment groups and μ is the sample mean for that group, called the predicted value. The residuals can be plotted against the group means μ for a residual versus predicted plot. When the residual variation is approximately bell-shaped about a residual of 0, the ANOVA model can be considered appropriate.

When looking at several sample sets (and the calculated sample means from different populations), one can examine the means to make a decision about whether or not the means of the populations from which they come are equal to one another. The null (0) hypothesis states that all of the samples are taken from populations with the same population means. The alternative (a) hypothesis is that at least two of the population means are different. If the sample means are different enough, then it would be determined that those differences are too great to be due to sampling error. Several assumptions are made about the populations that were sampled: (1) the samples come from normal populations, (2) the samples are independent, and (3) the standard deviations (or variances) are the same.

When examining a two-factor ANOVA, a comparison of main effects is useful to determine whether there is any interaction between the treatments. Examining interaction between two treatments is an added benefit upon performing a standard ANOVA test twice, once for each type of treatment. In two-factor ANOVA, for example, crossed lines in a main effect plot indicate interaction between the treatments because the factors do not have a compounding effect, but rather, cancel. To calculate the p-values, the following equations are used from Devore [60]. There are I by J treatments with K replications for each treatment type. When calculating, this can be stated as I rows by J columns with a constant K numbers of items in each cell. A star (*) in place of a subscript denotes summation over all values of that subscript and a horizontal bar indicates averaging. For example, the average of measurements obtained when factor A is held at level i

$$\bar{X}_{i*} = \frac{\sum_{j=1}^{J} x_{ij}}{J}, \tag{2.36}$$

and the grand mean is

$$\bar{X}_{**} = \frac{\sum_{i=1}^{I}\sum_{j=1}^{J} x_{ij}}{IJ}. \tag{2.37}$$

The fundamental identity which can be used as a check of the following calculated sums of squares is

$$SST = SSA + SSB + SSAB + SSE, \tag{2.38}$$

where the sum of squares total (SST) and degrees of freedom (df) is

$$SST = \sum_{i=1}^{I}\sum_{j=1}^{J}\sum_{k=1}^{K}\left(X_{ijk} - \bar{X}_{***}\right)^2, \qquad df = IJK - 1. \tag{2.39}$$

the sum of squares error (SSE) and degrees of freedom (df) is

$$SSE = \sum_{i=1}^{I}\sum_{j=1}^{J}\sum_{k=1}^{K}\left(X_{ijk} - \bar{X}_{ij*}\right)^2, \qquad df = IJ(K-1). \tag{2.40}$$

the sum of squares row A (SSA) and degrees of freedom (df) is

$$SSA = \sum_{i=1}^{I}\sum_{j=1}^{J}\sum_{k=1}^{K}(\bar{X}_{i**} - \bar{X}_{***})^2, \qquad df = I - 1. \tag{2.41}$$

the sum of squares column B (SSB) and degrees of freedom (df) is

$$SSB = \sum_{i=1}^{I}\sum_{j=1}^{J}\sum_{k=1}^{K}\left(\bar{X}_{*j*} - \bar{X}_{***}\right)^2, \qquad df = J - 1. \tag{2.42}$$

and the sum of squares interaction (SSAB) and degrees of freedom (df) is

$$SSAB = \sum_{i=1}^{I}\sum_{j=1}^{J}\sum_{k=1}^{K}\left(\bar{X}_{ij*} - \bar{X}_{i**} - \bar{X}_{*j*} + \bar{X}_{***}\right)^2, \qquad df = (I-1)(J-1). \tag{2.43}$$

Each of the four mean squares (MSA, MSB, MSAB, and MSE) is defined by

$$MS = SS/df. \tag{2.44}$$

The null (0) and alternative (a) hypotheses to be tested are $H_{0A}$ vs. $H_{aA}$, $H_{0B}$ vs. $H_{aB}$, and $H_{0AB}$ vs. $H_{aAB}$. The f statistic by which we make our decision against a critical value (F) is the ratio of the variance between the samples divided by the variance within the samples. A difference in population means, causing a difference between sample means, will result in a larger f, thus indicating that the alternative hypothesis is the correct choice. The test statistic value f and the rejection region for a two-way ANOVA are as follows

$$f_A = \frac{MSA}{MSE} \geq F_{\alpha,I-1,IJ(K-1)}, \tag{2.45}$$

$$f_B = \frac{MSB}{MSE} \geq F_{\alpha,J-1,IJ(K-1)}, \tag{2.46}$$

$$f_{AB} = \frac{MSAB}{MSE} \geq F_{\alpha,(I-1)(J-1),IJ(K-1)}, \tag{2.47}$$

where the subscripts of F represent the α confidence level (usually chosen to be 0.05 for 5%), degrees of freedom of the numerator (variance between samples), and degrees of freedom of the denominator (variance within samples), which are necessary for lookup in a table. If the calculated f value is greater than the tabulated F based on the degrees of freedom and confidence level, then the null hypothesis is rejected and we conclude that there is a significant difference in the populations which were sampled. In other words, if the associated p-value is smaller than the α level of significance, we can reject the null hypothesis.

# 3 PHASE CHANGES IN EMBEDDED HMX IN RESPONSE TO PERIODIC MECHANICAL EXCITATION

## 3.1 Introduction

It is well known that energy can be spatially localized when explosives are mechanically deformed; however, the heat generation mechanisms associated with this localization process are not fully understood. In this chapter, mesoscale hot spot formation in ultrasonically-excited energetic materials has been imaged in real-time. More specifically, periodic, mechanical excitation has been applied to Dow Corning Sylgard 184/HMX composite materials using contact piezoelectric transducers resulting in heating at various crystal locations. A thermally-induced phase transition from a β to δ non-centrosymmetric crystal structure for HMX results in the frequency doubling of incident laser radiation and can be used as a temperature proxy. In light of this, a high-repetition-rate 1064 nm Nd:YAG laser has been used to illuminate discrete HMX crystals, and a 532 nm filter has been applied to capture only the light emitted from the δ-phase SHG. The visualization of δ-phase initiation and growth is useful for determining both heat generation mechanisms and heating rates at crystal/crystal and/or crystal/binder interfaces and contributes to the understanding and prediction of hot spots.

Note that portions of this chapter were presented as “Phase changes in embedded HMX in response to periodic mechanical excitation” at the Society of Experimental Mechanics 2016 conference, and are reproduced from the book chapter of “Challenges in Mechanics of Time Dependent Materials, Volume 2, Proceedings of the 2016 Annual Conference on Experimental and Applied Mechanics” [15].

## 3.2 Experimental Methods

### 3.2.1 Sample Preparation

Grade B, class 3 β-HMX crystals manufactured by BAE Systems (lot BAE13E071-132) were selected as inclusions in the composite samples. The HMX was sieved to be greater than 425 μm to avoid influences of crystal size on the SHG signal [16, 20, 48]. In addition to being easily visible in the binder, coarser HMX crystals have the additional benefit of tending to phase transition at a lower temperature than finer crystals [48]. Samples included four HMX crystals

carefully arranged to be in close proximity and lying on the same plane within a Sylgard 184 silicone elastomer. Crystal proximity is an important factor in dropweight sensitivity testing [1], and for this reason, a system of multiple crystals was selected for this study. One of the four crystals in each sample was prepared as δ-phase for ease of laser alignment and focusing on the SHG signal, an idea similar in concept to Czerski *et al.* [53]. It also served as a point of reference and comparison in 'before' and 'after' optical microscope images. δ-HMX was created from the sieved β-HMX by heating the crystals on a plate at approximately 200 °C for several minutes until the crystals visibly changed to an opaque white color and increased in size. A 7% volume increase from β to δ-phase is noted by several authors [48, 52] when creating δ-HMX by different heating procedures. This phenomenon was clearly observed throughout the course of the experiment described herein. δ-HMX was cast into the Sylgard within a day, and tests were performed within four weeks to avoid possible reversion to β-phase or an alternate HMX phase and to avoid binder stiffening from aging [61]. Smilowitz *et al.* noticed that δ-HMX spontaneously transformed to α-HMX at room temperature after a time [21], and Czerski *et al.* expressed similar concerns [52].

Sylgard has been used in PBXs [35, 37] and was chosen as the binding material in this study due to its optical transparency at both the visible and near-infrared wavelengths. LX-13, XTX-8003, and XTX-8004 are all 80:20 mixes of energetic crystals to Sylgard 182 (boasting a longer pot life than Sylgard 184) with different specifications of PETN particle size, but XTX-8004 uses RDX instead of PETN [35]. All of the samples were cast simultaneously in Sylgard at a 10:1 wt. ratio of base to curing agent. As in prior work [16, 26], to facilitate the embedding of discrete crystals, multiple casting and curing steps were performed. At each casting step, liquid Sylgard was degassed under vacuum and then cured at 65 °C for 12 hrs [20, 22, 23, 28, 61]. First, a 'base layer' of 1 ± 0.2 mm was cast and cured. HMX crystals were then placed onto the base layer and totally encapsulated in a secondary layer of Sylgard. Finally, small rectangular sections were cut from this composite with a razor blade and placed into a variable-height mold with exterior dimensions of 6.6 × 8.9 mm. Each mold was then filled with binder to two different heights: 4.5 mm (short) and 8.1 mm (tall). Fig. 3.1 presents a dimensioned illustration of a single-particle short sample.

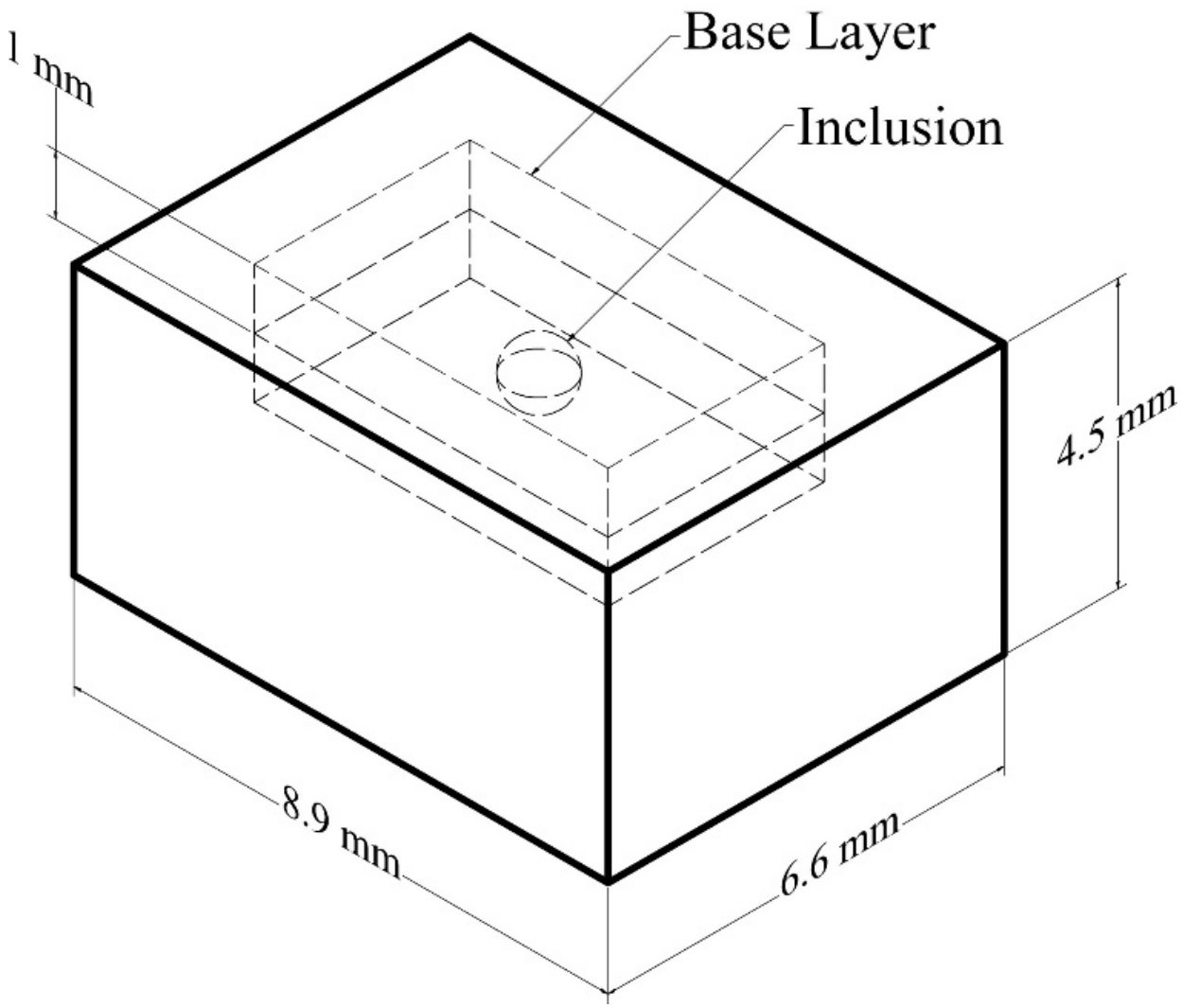


Figure 3.1. An illustration of the final dimensions and casting steps of a short Sylgard sample.

### 3.2.2 Mechanical Excitation and Second Harmonic Generation Measurement

A Steiner & Martins, Inc. SMD10T2R111 piezoelectric, ultrasonic transducer which has a nominal resonant frequency of 215 kHz was selected to conform to previous works [16]. As seen in Fig. 3.2, each sample was attached to a transducer with Devcon Flow-Mix 5 Minute epoxy and allowed to cure at room temperature. It was determined from the infrared imaging of a soot coated sample that a frequency of 210.5 kHz achieved the highest temperature increase for the system. A sinusoidal signal was sent to the transducer with a Keysight Technologies N9310A

RF Signal Generator at -3.0 dBm. In combination with a Mini-Circuits LZY-22+ High Power Amplifier, this supplied an on-sample power level of 10 W for a duration of approximately 20 s.

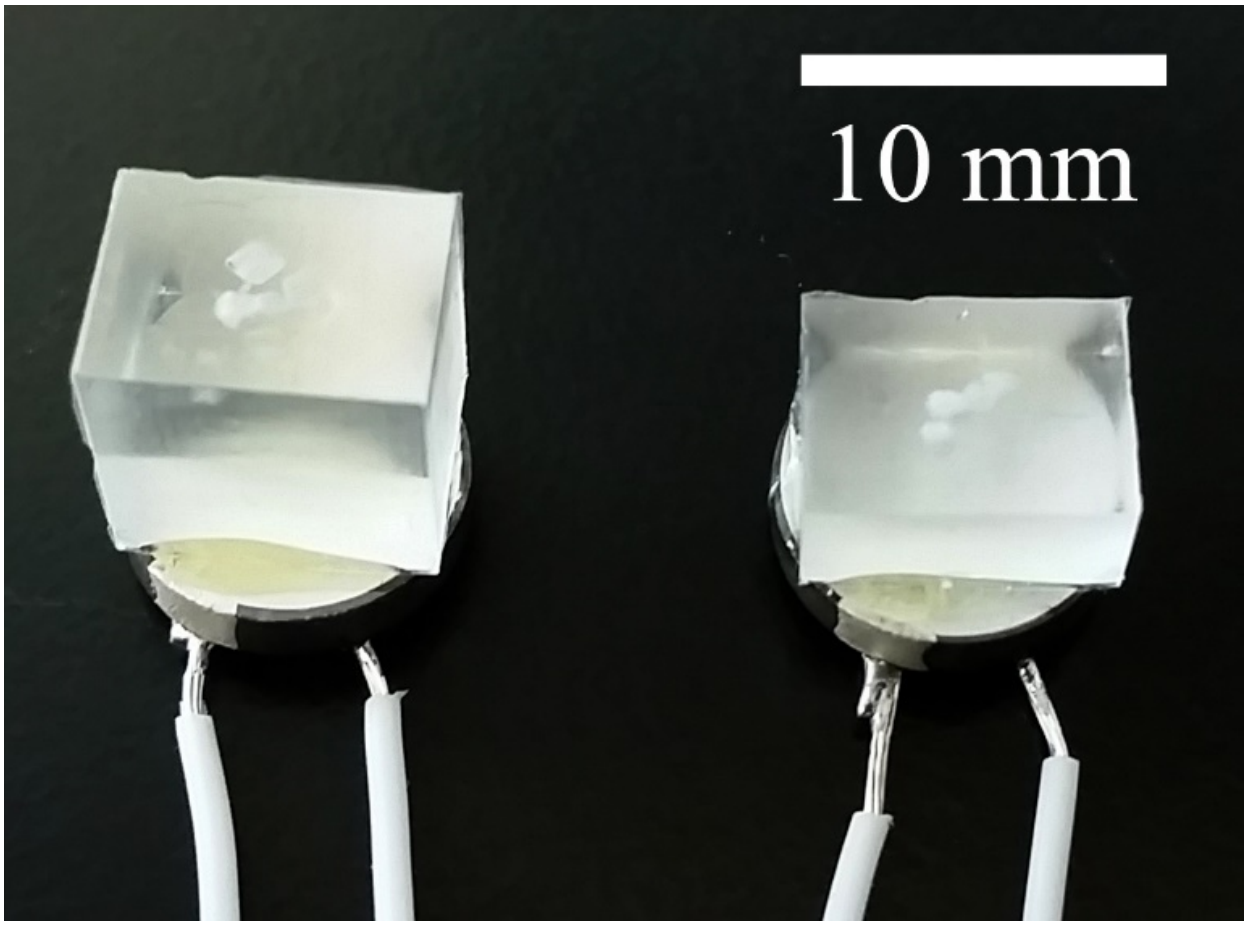


Figure 3.2. Representative tall (left) and short (right) samples attached to the piezoelectric transducers.

HMX crystals within the Sylgard samples were illuminated by a 1064 nm wavelength Nd:YAG laser with a pulse repetition frequency of 40 kHz. After beam expansion, the power was measured to be 5.6 W with a $1/e^2$ diameter of 1.5 mm. Because the influence of laser heating was a concern [52], the power level and diameter were chosen as the minimum values required for an easily-observable SHG signal capable of illuminating all four crystals. This was a lower power and smaller spot size than the lasers reportedly used in other SHG works [49, 52, 53]. The laser alone was verified to be insufficient to cause phase change at these timescales and the beam passed directly from the side through the Sylgard block without being incident on the transducer.

Images capturing SHG light were taken at 30 fps with a Canon XL2 3CCD MiniDV Camcorder on a low-light setting with an EF 100 mm f/2.8 macro lens. A 532 nm notch filter was inserted between the camera and the illuminated sample, as shown in Fig. 3.3. Experiments were conducted in a darkened room to ensure that the only light reaching the camera would be from the SHG at 532 nm.

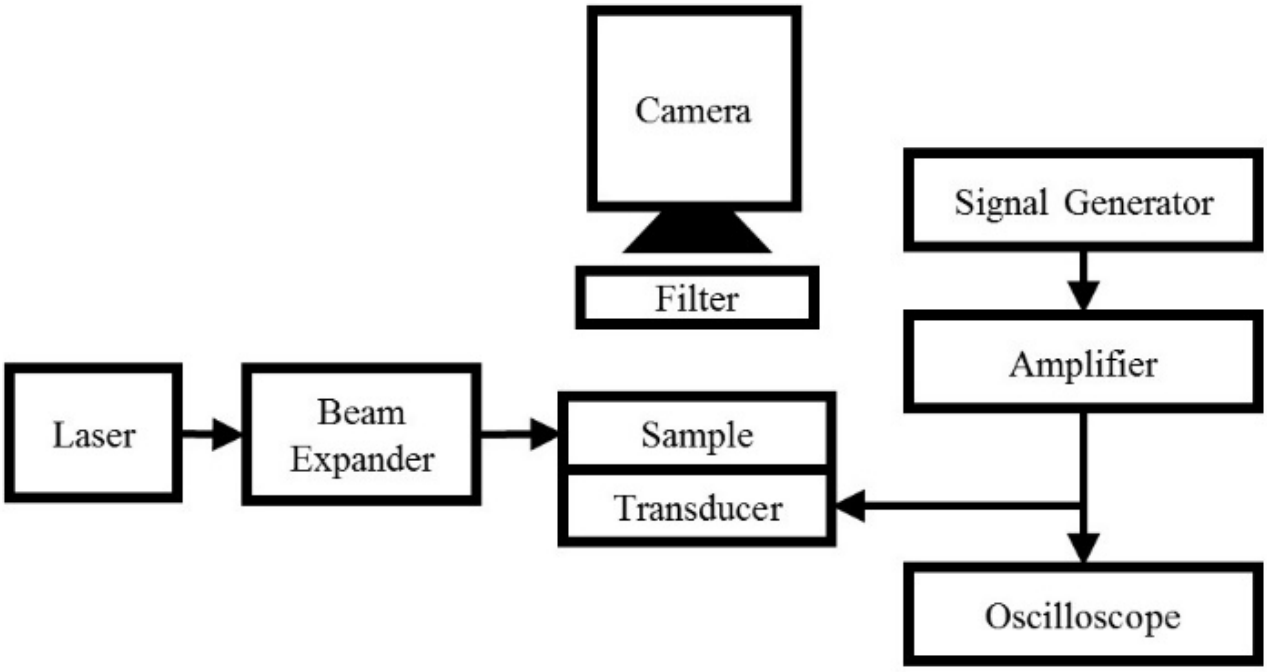


Figure 3.3. Schematic showing the relative positions of the camera and laser.

The camera could detect and register some near-infrared radiation, and so prior to each test, the laser was aligned without the 532 nm filter in place. This ensured that the beam illuminated all of the crystals within the Sylgard block. After alignment, the environment was darkened after several minutes and the trial began. Excitation time was monitored with an oscilloscope, and if SHG light was seen before ~10 s, the individual trial was allowed to continue for additional time up to approximately 20 s. The laser gate was opened approximately one second before the test began so that its contribution to heating was minimized. ‘Pre-test’ and ‘post-test’ images were taken with a Hirox KH-8700 digital microscope.

## 3.3 Results and Discussion

In Fig. 3.4, Fig. 3.6 and Fig. 3.7, real-time observations of the dynamic phase change of individual HMX crystals in a Sylgard binder are presented. The samples were illuminated by 1064 nm wavelength radiation from the left and some shadowing effects of the frequency doubled 532 nm light were present when phase changes occurred. Radiation may have been blocked by some δ phase-changing crystals that scatter light significantly. Consequently, in some samples, green SHG light was not sustained. In Fig. 3.4, Fig. 3.6 and Fig. 3.7, frame (b) corresponds to 0 s, which is defined as the time at which the transducer was powered. Frame (c) corresponds to the first SHG emission, which varied from 6.9 s to 10.6 s. Note that the captured SHG light contrast and saturation have been enhanced here, and an outline has been added in these stills around individual crystals so that the SHG is more easily seen. Frame (g) corresponds to the termination of each test, after which both the transducer and laser were turned off. All of the video frames presented are from the results of the ultrasonic excitation of the short samples. For all of the cases involving the tall samples, except for one which received over 20 s of excitation, the induced heating was insufficient to result in a phase transition of the embedded crystals.

In the first example, the uppermost crystal in Fig. 3.4(c) emitted initial SHG light. The highly-reflected green light proceeded to grow in intensity and propagate leftward across the crystal over the next few seconds. Figure 3.4(e) captured the most intense reflection of SHG light. The SHG signal at the point of maximum intensity on the upper crystal is shown versus time in Fig. 3.5. As observed in Fig. 3.4(h), the uppermost crystal has a cracked and opaque appearance. It also appears to have noticeably increased in volume as should be expected for δ-HMX [48, 50, 52]. The lower crystals in the figure have not changed significantly.

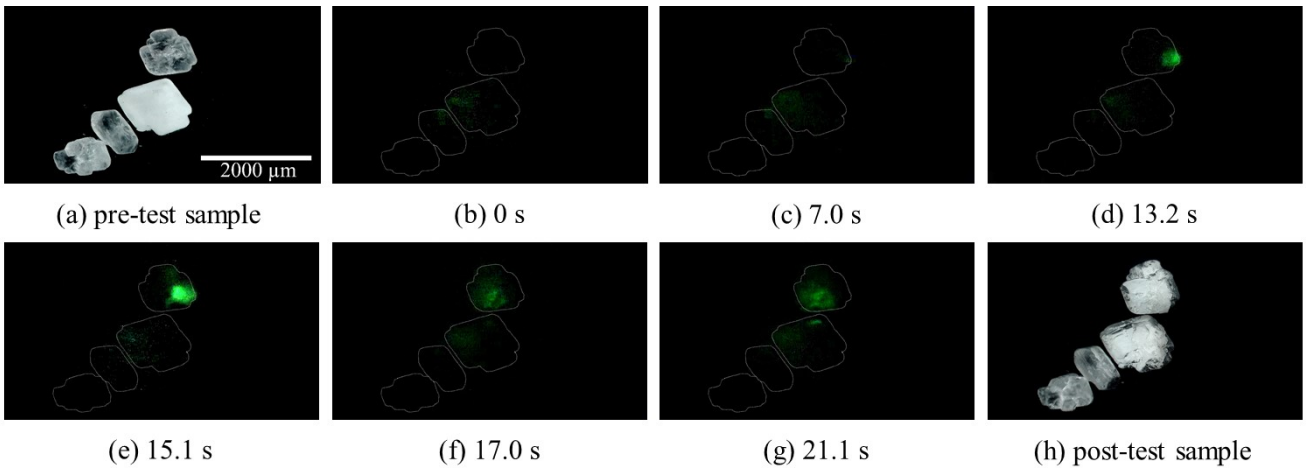


Figure 3.4. Selected frames showing a high reflectance of SHG green light during propagation across one of the embedded β-HMX crystals.

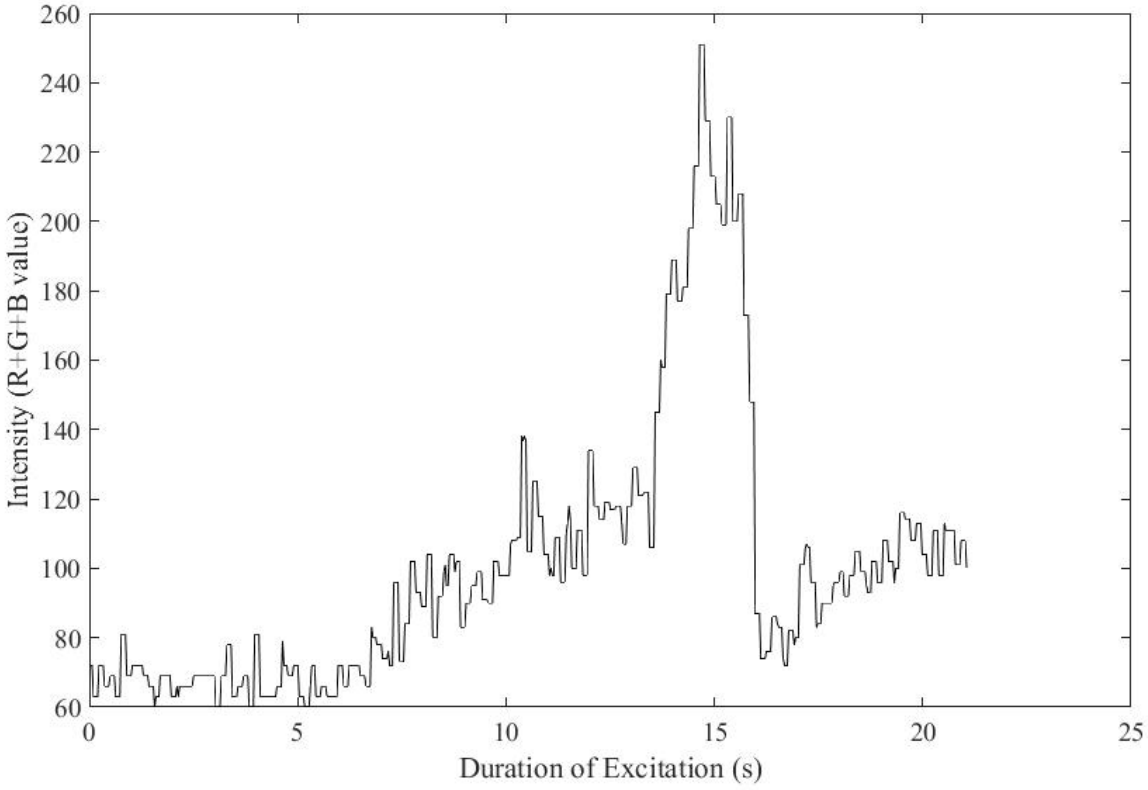


Figure 3.5. Plot of intensity versus excitation time at the point of maximum observed SHG light in a region of interest in the video comprising Fig. 3.4.

Figure 3.6 illustrates another instance of a single crystal undergoing phase transformation. This was the typical case in these experiments wherein not all of the crystals changed phase even after 21.0 s of excitation. At time 0 s, SHG green light from the δ-HMX inclusion in Fig. 3.6(b) is reflected off of the left side of the crystal. Additional SHG light began in Fig. 3.6(c) with a bright point suddenly appearing on the smaller, lower-left crystal. This point dimmed while the rest of the crystal slowly faded to green in Fig. 3.6(d), and was followed by the bright point reappearing in Fig. 3.6(e).

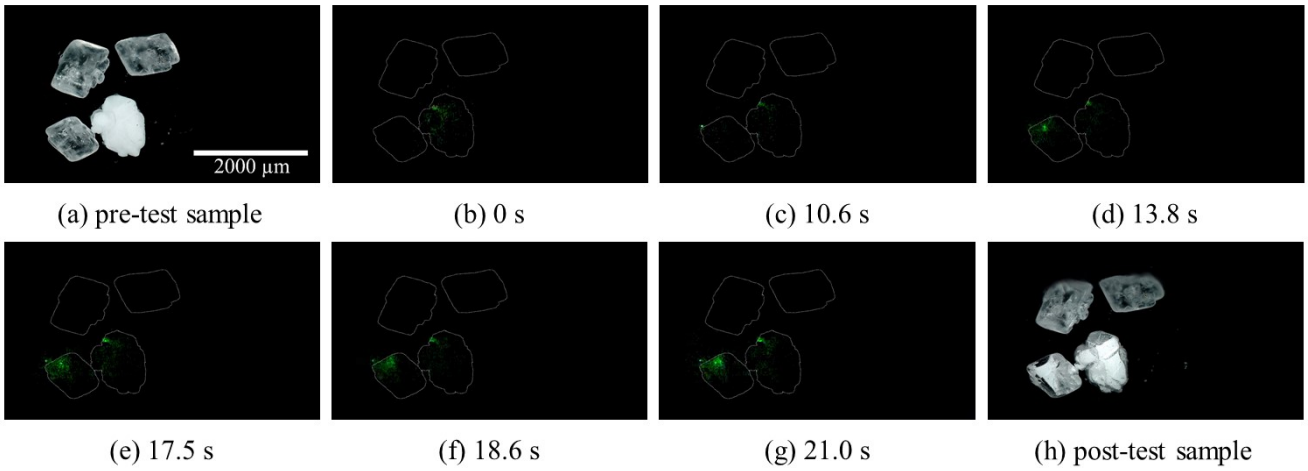


Figure 3.6. Selected frames showing a representative SHG response of a single-crystal transition event.

A sample that underwent a decomposition event is presented in Fig. 3.7. Additional SHG light was first seen after 6.9 s in Fig. 3.7(c) located where an adjacent δ-HMX crystal fragment was in contact with the original β-HMX. This began with bright interfacially-generated green light. All of the crystals in the binder experienced a phase transition in this trial. After 14.7 s, in Fig. 3.7(f), the sample visibly shifted under the camera. This was due to the sudden decomposition of HMX in which a gas pocket subsequently burst open the binder in the plane that was formed during casting as shown in Fig. 3.7(h).

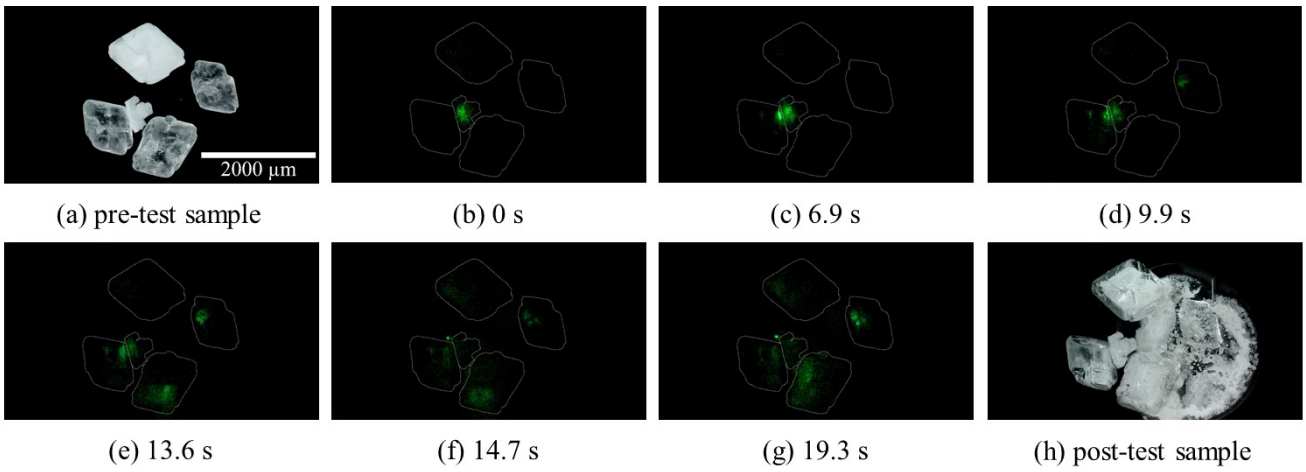


Figure 3.7. Selected frames showing SHG response of embedded HMX crystals which resulted in decomposition.

Of the nine short samples tested, examination of the post-test microscope images revealed additional δ-HMX in all but one sample. Not all of the δ-HMX crystals demonstrated SHG, most likely due to a combination of shadowing effects or an insufficient irradiance near the edge of the beam. In four of the eight samples that experienced a phase transition, only a single crystal changed, while the other four samples experienced multiple phase-changed crystals. Three samples with multiple phase-changed crystals decomposed, two of which broke the surface of the Sylgard layer resulting in a low, but audible report.

## 3.4 Conclusions

SHG of HMX crystals in a binder under ultrasonic stimulation has been shown to provide a real-time indication of the crystal phase and was therefore used as a temperature marker. For the experimental configuration presented in this chapter, different mechanisms may be responsible for heating. In the near field of the transducer, and around inclusions, there are expected to be non-uniform stresses and deformations in the plane of interest. Although the on-axis plot of normalized pressure in Fig. 2.1 shows a single maxima 3.5 mm into the sample using these excitation parameters, there are lobes at different angles from the normal created by wave interference effects. These areas of concentrated stresses could be considered hot spots with points of intense heating. This heating would raise the temperature of the nearby HMX crystals

resulting in a phase change once they reached 170 °C. Other crystals in the binder are expected to have lower temperatures than 170 °C when SHG light is initially detected.

Surface asperities, crystals in close proximity, as well as points of contact between crystals may be responsible for localized frictional or viscoelastic heating as passing waves induce stress in the binder [2, 3, 26]. Mechanical energy dissipated in this way may also induce delamination at the crystal/binder interface resulting in increased frictional effects. SHG results akin to those presented in this work seem to indicate δ-phase propagation from interfaces. Smilowitz *et al.* suggests that SHG light observed from nucleation sites cannot be associated with crystal morphology or defects [21]; however, their experiment explored uniform heating over hours and does not address how a rapidly-deforming binder would interact with crystal features.

There were results presented in this work in which a single HMX crystal experienced SHG, regardless of the size of the other crystals in the same binder. There were also long periods of excitation after an initial phase change during which no other crystals transitioned. Using the results from Saw [48], which show that larger HMX crystals change phase first, one can interpret single-crystal transitions as being indicative of hot spots formed from focused acoustic energy. The smaller individual crystal was likely near a point of high stress concentration in the near-field of the transducer, while the others were not. This experimental technique is limited by the fact that the HMX inclusions must reach temperatures on the order of 170 °C. This fact was expounded in the taller samples where crystals located farther away from the near-field effects of the transducer did not experience any phase change. Given the combined effects of being further away from the near-field and resistive heating, no temperature information was gained from the HMX crystals in the tall samples. Conclusions cannot necessarily be drawn from where the SHG began to occur on, or in, individual crystals [21, 50], but this work has shown that the transitioning crystals are an indication of hot spot locations.

The acoustic insult of composite energetic particle and elastic binder systems in similar configurations [16] have been shown to drive ammonium perchlorate (AP) and HMX crystals to decomposition. In the present work, the decomposition of HMX crystals is indicative of reaching 290 °C [48] after which on a hot plate the crystals would normally form an amorphous structure and burn. In the work of Mares *et al.* [16], IR thermography quantified the radiation emitted from the surface of similar composites, but failed to capture the exact temperature at hot spot

locations. The technique of SHG employed herein has provided more information about particle temperatures within the binder and has shown that the inclusions are capable of reaching 170 °C and above. Mares *et al.* reported observing a maximum surface temperature rise over 2 s of excitation of 57.93 °C with an estimated HMX particle temperature of 74.24 °C [16]. This is consistent with the ~20 °C/s temperature rise obtained using the SHG results presented in the current work. You *et al.* reported a hot spot temperature for polyethylene glycol (PEG) coated sucrose in a polydimethylsiloxane (Sylgard 182) binder which reached ~327 °C with a reported 22,000 °C/s heating rate and approached the dynamic range limit of their camera [28]. While this is curiously above the melting temperature of sucrose, it is in the range of HMX decomposition temperature indicated in the current work with low-power excitation.

Future work in this area should address how the heating mechanisms associated with acoustic interactions compare to that in shock and impact studies. Additionally, future work should focus on the effect of crystal proximity and the time to initial SHG. Investigations should examine how energy deposited from passing acoustic waves affects the rate of heating and SHG kinetics over time [50]. SHG should also be used to validate temperature measurements of encapsulated crystals. Others have shown that the δ-phase transition may be a precursor, or linked, to ignition [52], and therefore the phase transition phenomenon is an important consideration in munitions subjected to shock, vibration, and heating.

# 4 THE EFFECTS OF CRYSTAL PROXIMITY AND CRYSTAL BINDER ADHESION ON TEMPERATURE IN ULTRASONICALLY EXCITED COMPOSITE ENERGETIC MATERIALS

## 4.1 Introduction

Insight has been gained with ultrasonic experiments on ‘simplified’ PBX samples consisting of a solid inclusion in a block of elastomeric binder [15, 16, 19, 26–28]. Longer duration hot spots from the lower heating rates seen in ultrasonic experiments are useful for investigating the temperatures and locations of heating, and also to approximate some loading conditions experienced during transportation and use. While Sylgard serves to desensitize an explosive to impact and friction [37] or is sometimes selected over other binders such as HTPB due to ease of handling, a closer look at Sylgard binder adhesion [62, 63] to particles is needed to further understand the susceptibility of some composite energetic materials to generate heat from vibrational loading. Currently, studies of particle/particle interactions in simplified PBX systems have been phenomenologically guided or have considered relatively few samples, and are yet to be systematically examined. In an attempt to isolate the proposed heat generation mechanisms of frictional and viscoelastic heating at crystal/crystal and crystal/binder interfaces, a systematic study was conducted with HMX crystals arranged as discrete inclusions within Sylgard 184 binder.

The objectives of this chapter are to more fully understand the influence of different heat dissipation mechanisms in periodically insulted composite energetic materials, such as PBXs and solid propellants, by examining evidence of hot spots induced by heating from the motion of a polymer binder near or against an HMX crystal surface. Groups of three embedded crystals, or ‘triads’, were arranged in two geometries with the crystals either in contact or slightly separated. Additionally, samples with good crystal/binder adhesion as well as ones mechanically debonded using compression were considered. The samples were excited ultrasonically with a contact piezoelectric transducer and the top surface of each sample was monitored via IR thermography. This work was performed in collaboration with A. D. Casey and portions of this chapter are reproduced from “The effects of crystal proximity and crystal binder adhesion on temperature in ultrasonically excited composite energetic materials” in the Journal of Applied Physics volume 122, issue 24, paper 244901, 2017, with the permission of AIP Publishing [19].

## 4.2 Experimental Methods

### 4.2.1 Sample Preparation and Characterization

Each experimental specimen contained three HMX crystals embedded on a single plane, 1 mm deep within a block of neat Sylgard 184 binder, made following a three-step procedure. β-HMX crystals (BAE Systems grade B, class 3) were selected for inclusion and sieved to between 500-850 μm with similar sized crystals grouped together. The binder material was chosen to be Sylgard 184 due to its optical transparency and to conform to previous works [15, 16, 26]. Sylgard was mixed in a 10:1 base to curing agent ratio by weight. A 'base-layer' of nominally 1 mm thickness was created with an aluminum-polycarbonate mold and degassed under vacuum (achieving a gauge pressure of approximately -90 kPa) to remove trapped bubbles. The base-layer and all of the subsequent layers were cured in an oven at 60 °C for 12 h to avoid variations in mechanical properties of the binder [61, 64].

A second layer of approximately 1-2 mm of Sylgard was poured over the 1 mm base-layer and HMX crystals were deposited. These crystals sank to the cured interface and the mixture was degassed under vacuum. It was evident that good binder/crystal adhesion would be achieved as small bubbles were drawn away from the crystal locations. HMX crystals were arranged with forceps into groups of three, called 'triads', and this mixture was then cured, encapsulating the particles. Rectangular sections containing the embedded HMX triads were cut from the cured 'dual-layer' with a razor. 'Contacting triad' samples were verified to have at least two points of contact between the three crystals from both side and top microscope views. 'Separated triad' configurations contained HMX crystals spaced within the binder by 108-825 μm edge-to-edge with an average separation of 380 μm as measured with a Hirox KH-8700 digital microscope and shown in Fig. 4.1. Finally, 'debonded-contacting' and 'debonded-separated' samples were created by manually compressing 24 of the 48 total pristine dual-layer samples under the microscope until at least half of the Sylgard had delaminated, or pulled away, from the embedded crystal surfaces without cracking the crystals. Dual-layer rectangular cutouts were manipulated with pliers from both sides until this was achieved, as shown in Fig. 4.2.

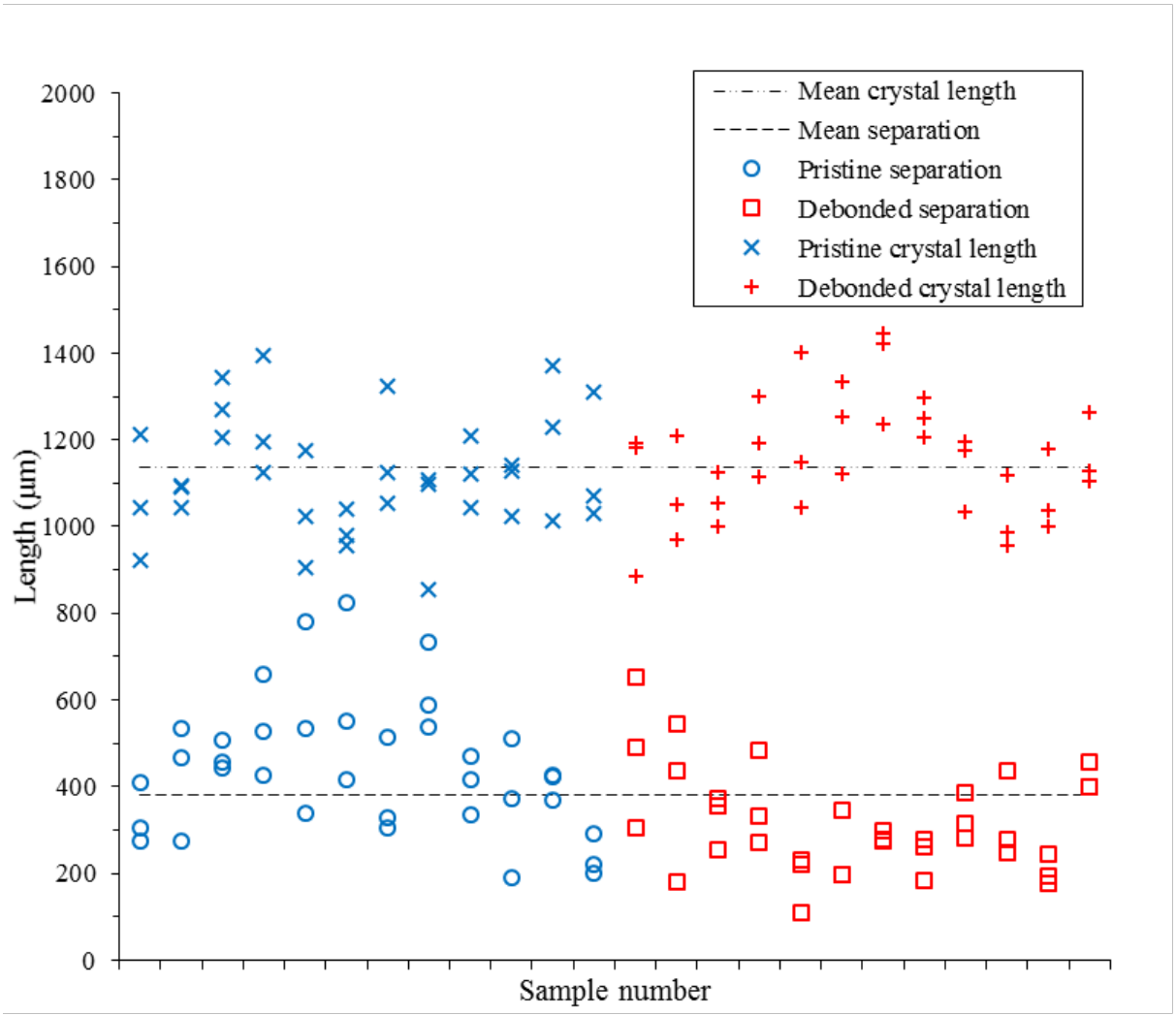


Figure 4.1. Separated triad and debonded-separated triad minimum edge-to-edge separation distances and maximum crystal lengths (three values each per sample) are shown alongside the mean values for all of the samples. Debonded samples were created from a population of ideally pristine samples to achieve approximately the same separation distance and crystal lengths for later statistical analysis. Crystal locations did not change within the binder after debonding, nor were the crystals damaged.

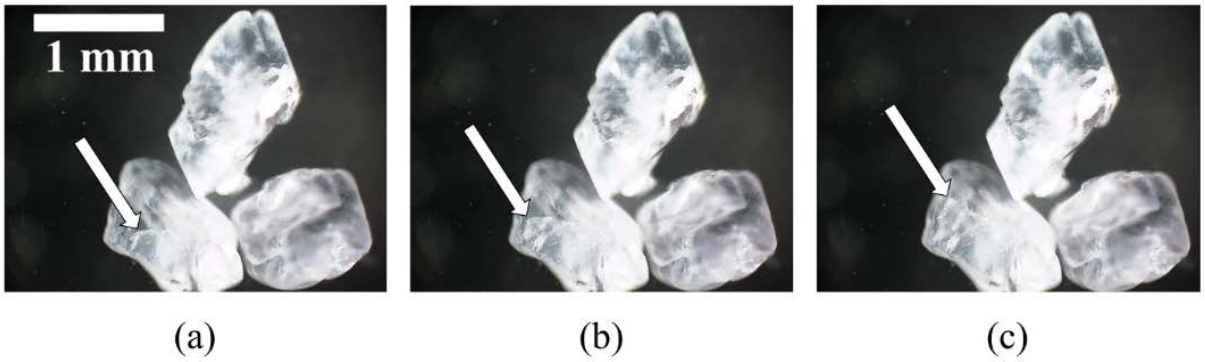


Figure 4.2. Image sequence showing the mechanical debonding of Sylgard binder from the HMX crystals in a debonded-contacting triad sample configuration. The arrow shows an edge of the delaminated area which moved across the surface of a crystal as a compressive force was applied from the top and bottom of the frame. All three crystals were debonded.

Finally, dual-layer cutouts containing encapsulated particles were placed into aluminum molds with the 1 mm thick side down to obtain the final dimensions of 8.9 mm × 6.6 mm × 4.5 mm. Clear packaging tape covered the bottom of the aluminum molds to give the final Sylgard block top surfaces a smooth finish without blemishes. This was necessary because any surface defect would be captured by the IR camera during testing. Sylgard for the mold underwent an identical mixing, pouring, degassing, and curing procedure as before.

### 4.2.2 Mechanical Excitation and Infrared Thermography

One Steiner & Martins, Inc. SMD10T2R111 PZT ultrasonic transducer was used for all of the tests. This was used to ensure repeatability of insult which should reduce variation in heating for later statistical analysis. Sonotech Soundsafe ultrasonic couplant was used between the Sylgard sample bottom surface and the transducer. Uniformity of the couplant was extremely important and it was visually confirmed before every run that there were no trapped bubbles and that the sample laid flat on the transducer. Samples were removed, reattached, and allowed to cool for approximately 3 min after every run for 5 runs of each sample to equally apply the inherent randomness of this process. The transducer was excited with a sinusoidal signal from an Agilent N9310A RF signal generator (210.5 kHz at -3.0 dBm) and amplified by a Mini-Circuits LZY-22+ high power amplifier (+43 dB, 24 V power supplied from a Keysight E3634A DC

Power Supply) at approximately 10 W of output power for 4 s. It was determined in previous studies [15, 16, 26] that 210.5 kHz achieved the highest temperature increases for this system and was near a resonant frequency of the transducer. The excitation time of 4 s was chosen so that the HMX crystals did not reach high enough temperatures to transition to δ-phase [48], entirely debonding the crystal, or decompose, preventing multiple runs with the same sample [15]. Excitation time was monitored with a Tektronix DPO 4043 oscilloscope. The temperature of the top surface of the Sylgard was monitored with a FLIR A325sc infrared camera with a FLIR T197200 close-up 2× lens recording at 30 fps. The starting frame of each run was determined from the onset of heating evident in the transducer wire leads. Thermal sensitivity of the camera was reported by the manufacturer to be < 0.05 °C at 30 °C with an accuracy of ±2 °C or ±2% of the reading. An experimental schematic showing the equipment and camera orientation along with a photograph of a sample is depicted in Fig. 4.3.

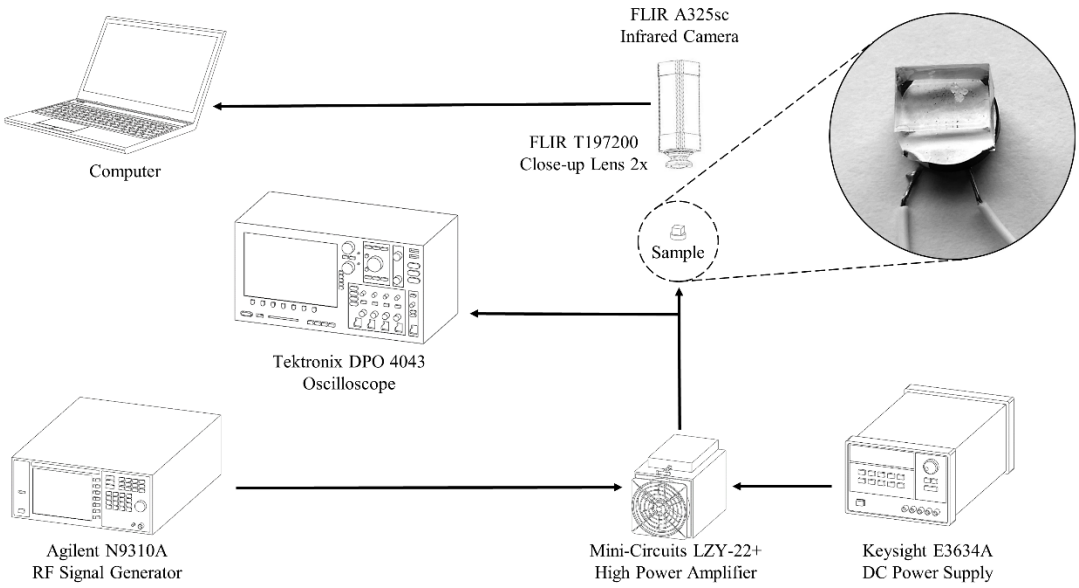


Figure 4.3. Experimental schematic depicting a contacting triad sample, infrared camera, and the excitation signal generating equipment.

## 4.3 Results and Discussion

The maximum temperature rise on the top surface of the samples over 4 s of excitation is shown in Fig. 4.4. The 4 sets of 12 samples were run 5 times each and the maximum and minimum temperature among runs at any time is bounded by a patch of 20% opacity. Samples with high run-to-run variance are graphically shown as a larger patch. For the contacting triad tests recorded in Fig. 4.4(a), 9 of the 12 samples had evidence of an intense heat source that conducted to the top surface of the Sylgard blocks above the inclusion locations and 3 samples had weak or bulk heating. Microscope images of the contacting triad samples were superimposed with corresponding first-run infrared videos and the spot of maximum temperature appears directly above crystal points of contact in 6 cases. Representative runs are shown in Fig. 4.5. Superimposed videos of the debonded-contacting samples in Fig. 4.4(c) revealed strong heating above crystal points of contact in 6 of the 12 samples, 1 sample for which strong heating appeared to coincide above the location of 3 crystals simultaneously, and 5 cases for which heat appeared to conduct from a single crystal location. For the debonded-separated samples in Fig. 4.4(d), superimposed videos showed heating above all 3 crystal locations simultaneously in 3 of the 12 samples, above 2 crystal locations in 3 samples, and above 1 crystal location in 6 samples.

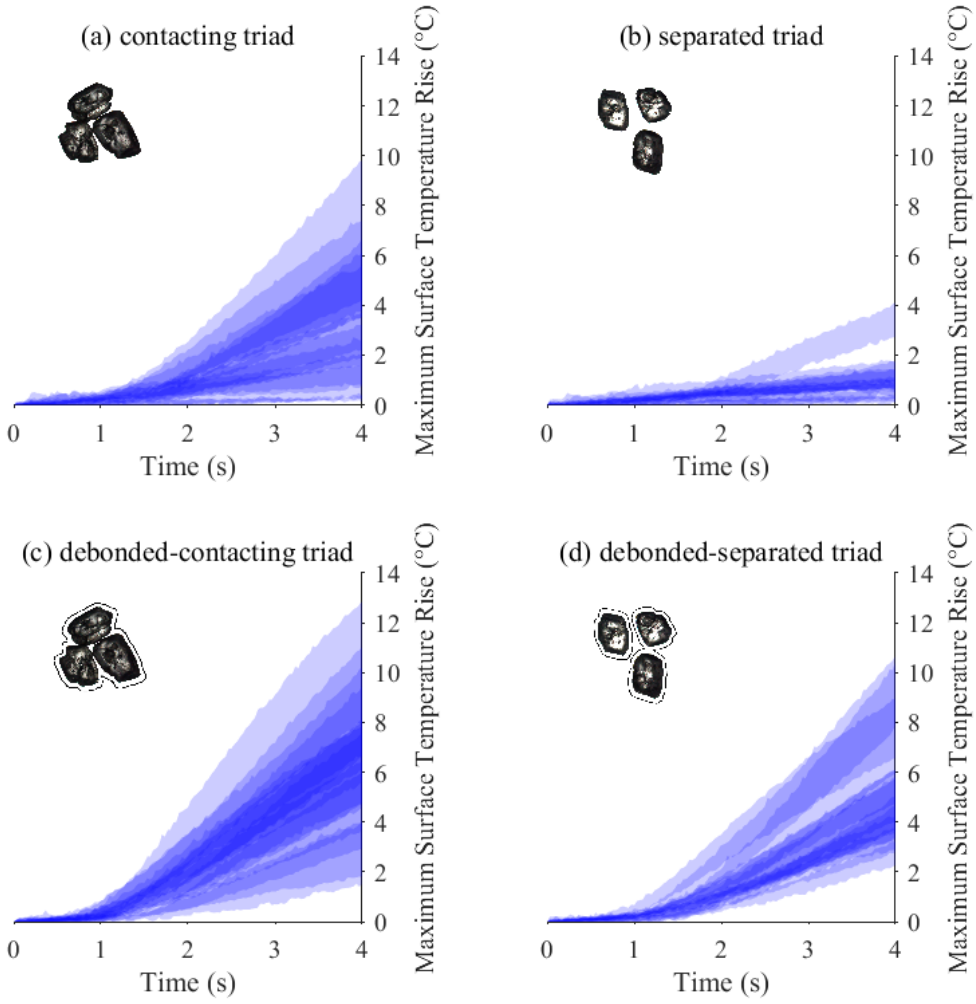


Figure 4.4. Maximum surface temperature rise versus time for 12 samples of each configuration: (a) contacting triad, (b) separated triad, (c) debonded-contacting triad, and (d) debonded-separated triad. For each sample, the temperature was recorded over 4 s for 5 runs and the maximum and minimum temperature rise at any time for each sample are bounded by a patch of 20% opacity. The data for the 12 samples of each set are overlaid on each other, where overlapping patches for samples achieving the same temperature rise with time result in darker hues. Schematics of typical crystals are shown for clarity.

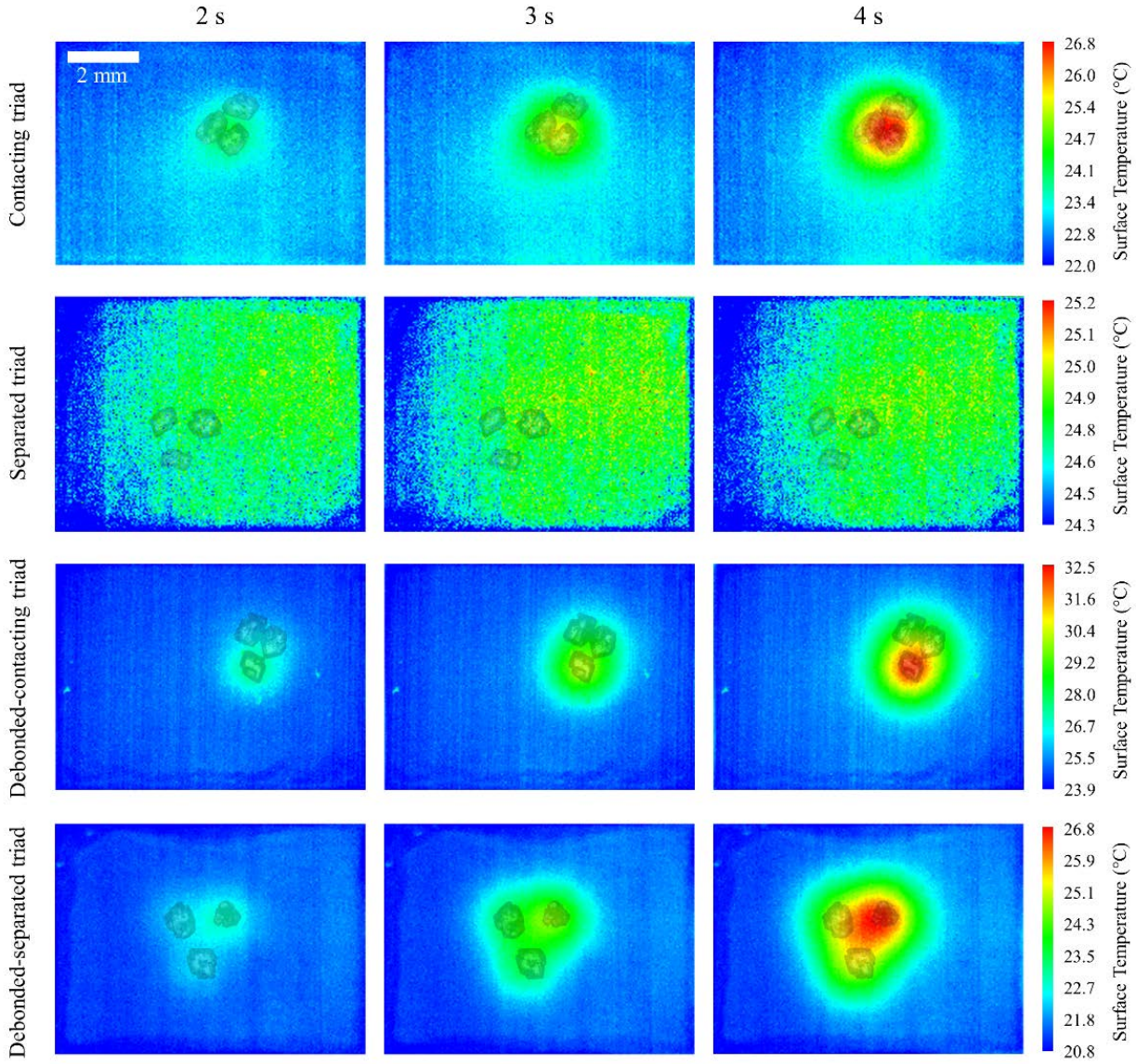


Figure 4.5. Infrared thermography image sequences for representative contacting triad, separated triad, debonded-contacting triad, and debonded-separated triad samples with backlit microscope images of crystals superimposed at 25% opacity after 2 s, 3 s, and 4 s. The temperature scale was fixed for each sequence by the temperature field of the final frame. Contacting triad images show a representative intense localized spot of maximum temperature appearing above crystal points of contact. Separated triad images show bulk heating of the sample with no apparent localized heat source. Debonded-contacting triad images show localized heating above a single inclusion location. Debonded-separated triad images show a case with heating from all 3 inclusion locations.

Contrasting this, the separated triad tests resulted in flat temperature profiles as illustrated in Fig. 4.4(b). There was no evidence of localized heating around the inclusion locations except for one outlier sample. The outlier sample was characterized by above average edge-to-edge crystal separation distances and below average crystal lengths (sample 6 in Fig. 4.1), but the temperature rises were consistent with those of a debonded-separated sample. This heating could be attributable to debonding of the binder at a crystal interface prior to testing, likely due to rough handling, or that poor degassing or crystal morphology provided weaker adhesion, allowing debonding during the 4 s test. The temperatures achieved were similar to those of blank Sylgard samples with no inclusions, where only viscoelastic heating of the binder and thermal conduction from the transducer heating up are expected to contribute to the observed surface temperature. No correlation is seen between the rise in surface temperature of the separated triads with the values of crystal separation distance or crystal size. It should be noted that the range of crystal sizes used here do not reflect a bi-modal distribution seen in standardized formulations and that a greater range of sizes may show heating dependence. As will be seen in subsequent chapters, surface morphology plays a more critical role in determining the chance of delamination and rapid heating.

The temperature profiles for the debonded-contacting and debonded-separated triads in Fig. 4.4(c) and Fig. 4.4(d), respectively, are similar to those of the contacting triad samples, inasmuch that every sample showed evidence of localized heating at a point. Furthermore, only one run from two different samples failed to reach above a 2.0 °C increase after 4 s of excitation. Debonded-contacting triads in Fig. 4.4(c) had higher average heating and the highest surface temperature achieved by any sample set at 12.9 °C.

The run-to-run trends in maximum surface temperature rise for samples of all 4 types had approximately equal numbers of cases in which the temperature increased, decreased, and remained constant over the 5 runs. It was interpreted that debonding/damage was not occurring with subsequent runs and that most of the variance can be attributed to the repositioning of the sample on the transducer after every test. One exception to this was the contacting sample for which the 4 highest temperature rises were recorded in Fig. 4.6, which increased with subsequent runs. Mean maximum temperature rises after 4 s, shown in Fig. 4.6, were higher for contacting triad configurations ($\mu$ = 3.6 °C) than for separated triad configurations ($\mu$ = 1.2 °C). The mean values for all of the runs of debonded-contacting triads ($\mu$ = 6.0 °C) and debonded-separated

triads (μ = 5.2 °C) at the conclusion of the test were higher than either of the nominally pristine adhesion counterparts.

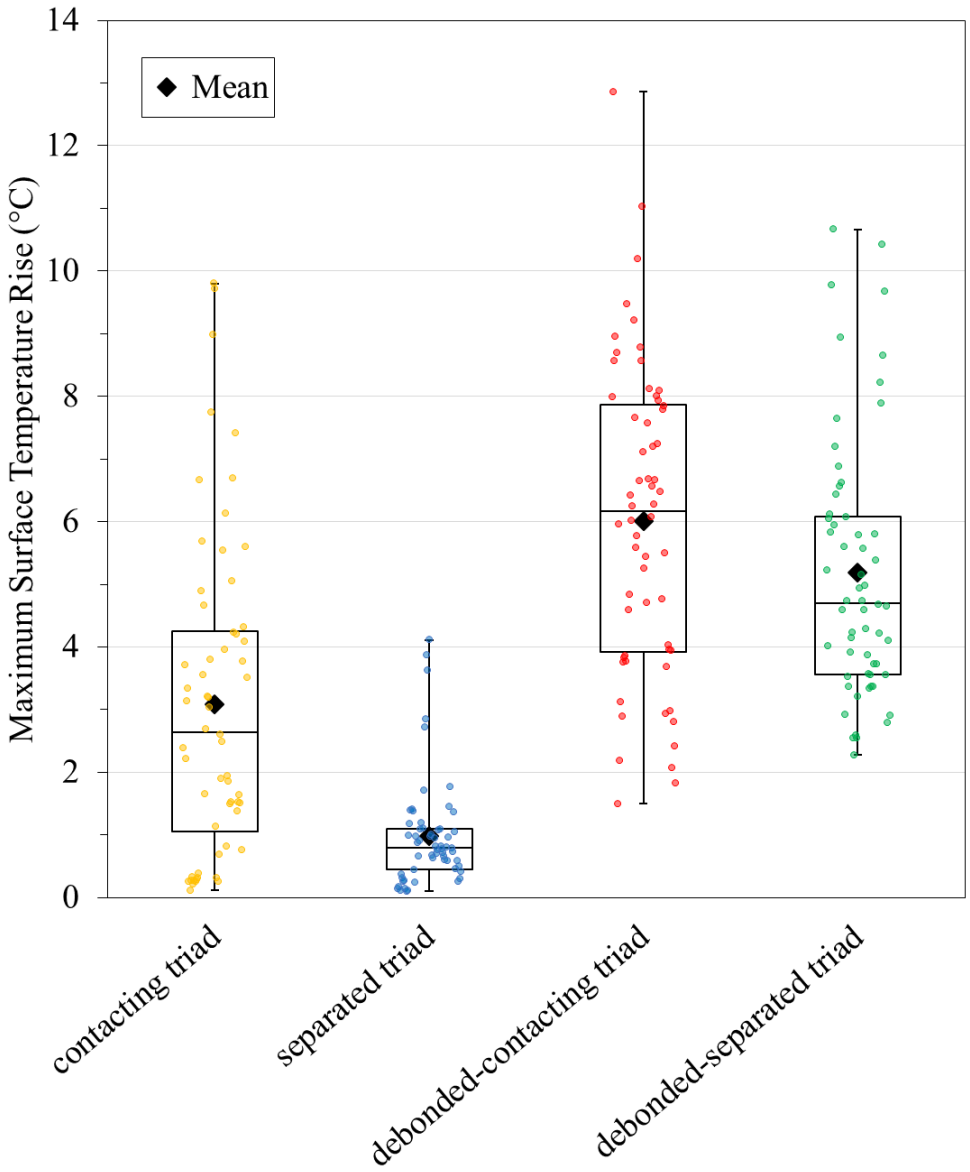


Figure 4.6. Dot-box plots of the maximum surface temperature rise at 4 s of excitation for the 4 configurations of contacting triad, separated triad, debonded-contacting triad, and debonded-separated triad. Means at 3.1 °C, 1.0 °C, 6.0 °C, and 5.2 °C, respectively, are represented by a solid diamond. All 5 runs of each of the 12 samples among the 4 sample types are presented. X-axis locations of the dots are arranged by sample number which sometimes results in clusters of data points. Note that these are the last data points from Fig. 4.4.

## 4.4 Statistics

A two-way ANOVA of separation distance (contacting triad, separated triad) and crystal adhesion (pristine, debonded) factors on temperature at 4 s of excitation was conducted on the 48 averaged values of the 5-run subgroups. Data for the averaged sample temperatures appear to fulfill the normality and constant variance ANOVA assumptions by examination of quantile-quantile and residual plots, respectively. Residual plots are shown in Fig. 4.7, Fig. 4.8, and Fig. 4.9 per Equation (2.35). A model has good fit when the residual variation is approximately bell-shaped about a mean residual of 0. A main effect plot is shown in Fig. 4.10 and quantile-quantile plot is shown in Fig. 4.11. The full data set and the 5 trial average data set are plotted together. Two-way ANOVA was performed following Equations (2.36)-(2.47) using I = 2, J = 2, K = 12 (each one of these K is an average of 5 observations) for a total of 48 values. The average was taken because the 5 observations of one sample were by definition not independent and an assumption of ANOVA is that the data are independent and identically distributed (IID).

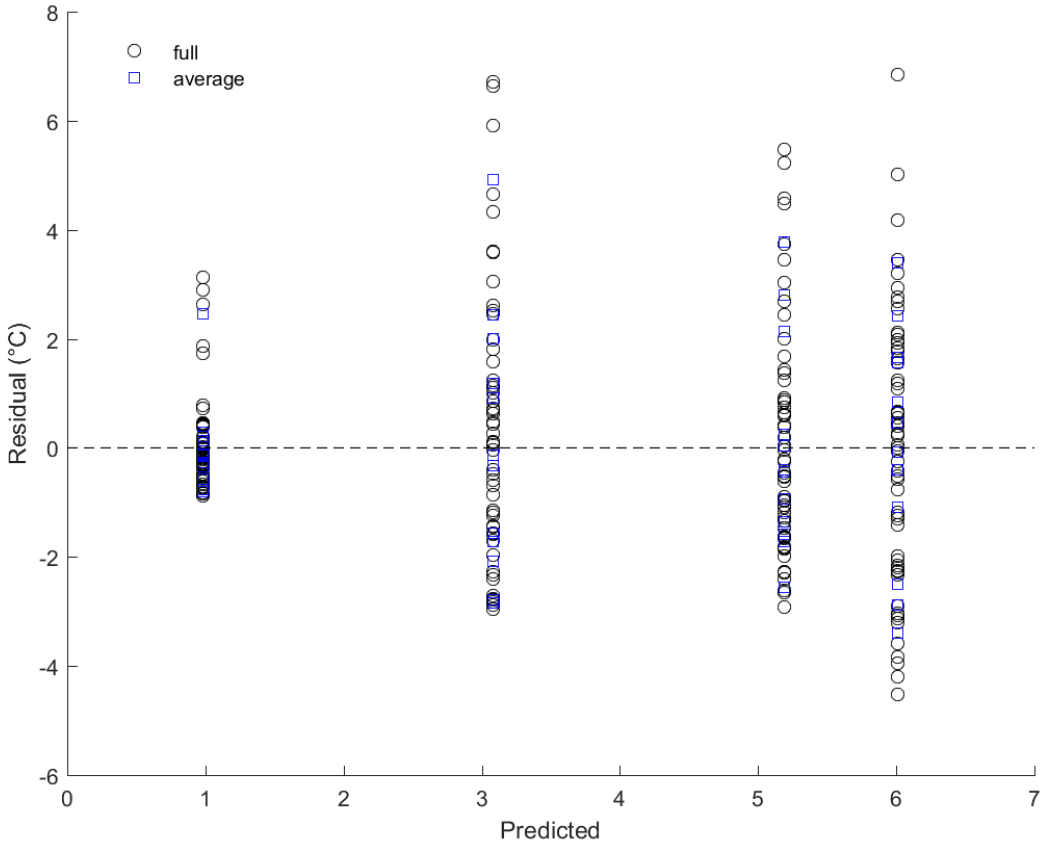


Figure 4.7. Residual estimates of experimental error vs. predicted responses (the overall means as shown in Fig. 4.6, are for separated, contacting, debonded-separated, and debonded-contacting, equaling 1.0 °C, 3.1 °C, 5.2 °C, and 6.0 °C, respectively). The full data set and the 5 test average data set are plotted together.

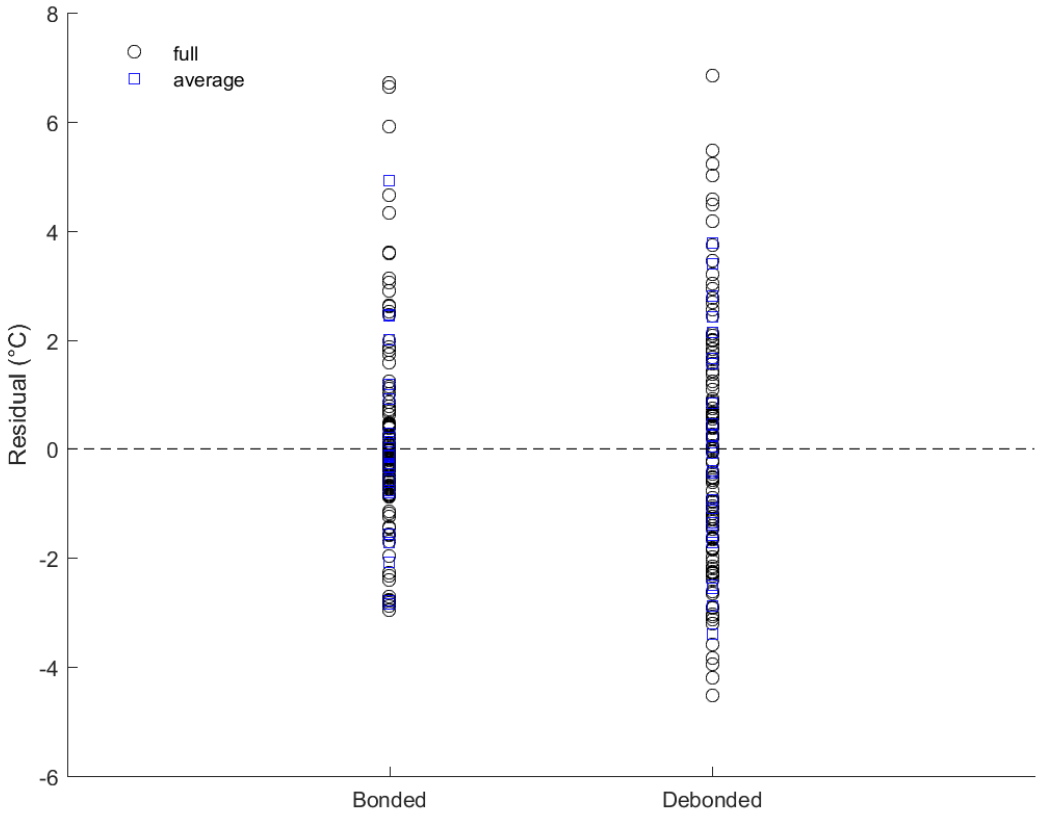


Figure 4.8. Residual estimates of experimental error for both the full data set and the 5 test averaged data set are plotted as crystal adhesion (bonded and debonded) groups.

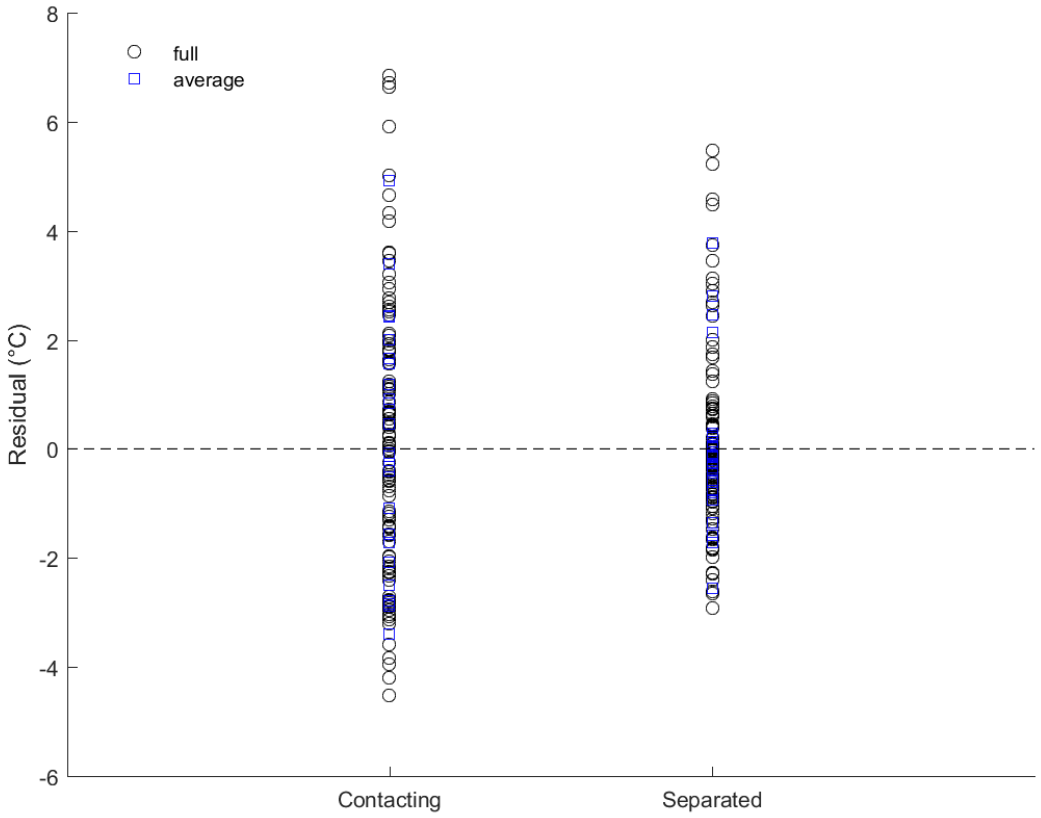


Figure 4.9. Residual estimates of experimental error for both the full data set and the 5 test averaged data set are plotted as separation distance (contacting and separated) groups.

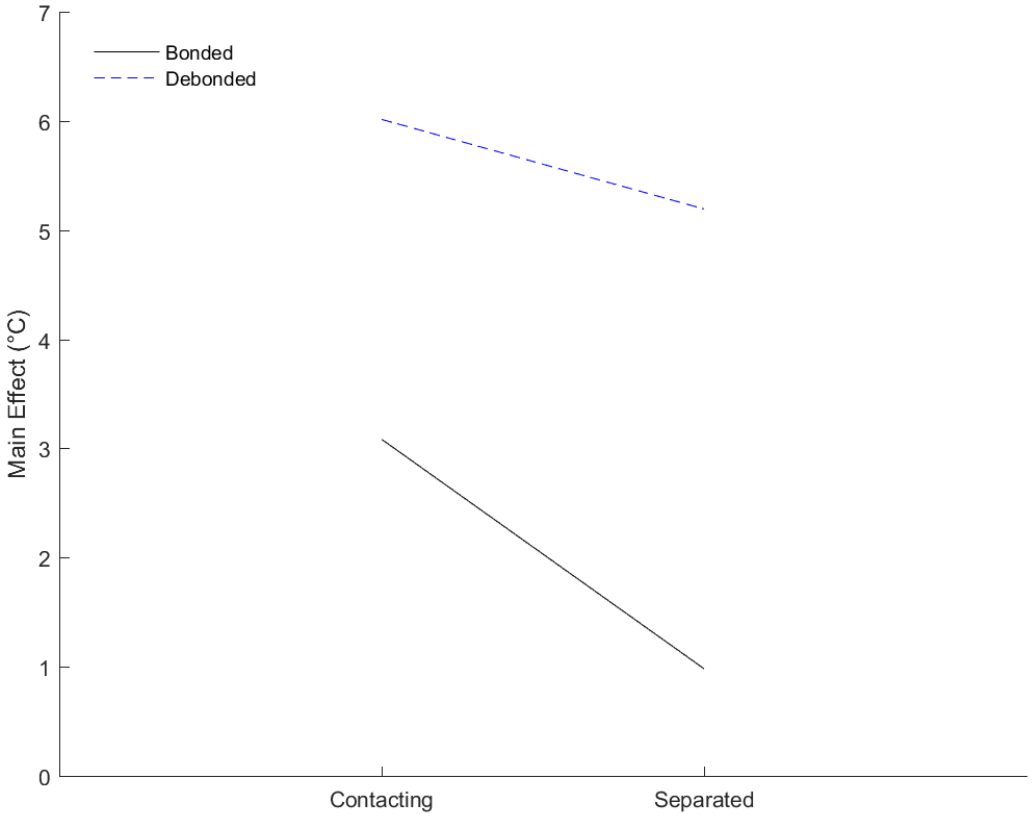


Figure 4.10. Main effect with dependent variable (maximum temperature rise after 4 s) on the y-axis and two independent variables as the x-axis (crystal separation) and in the legend (adhesion). Note that the lines do not cross, indicating no interaction between degree of adhesion and geometry. The temperature is higher for contacting crystal samples in both the bonded and debonded cases.

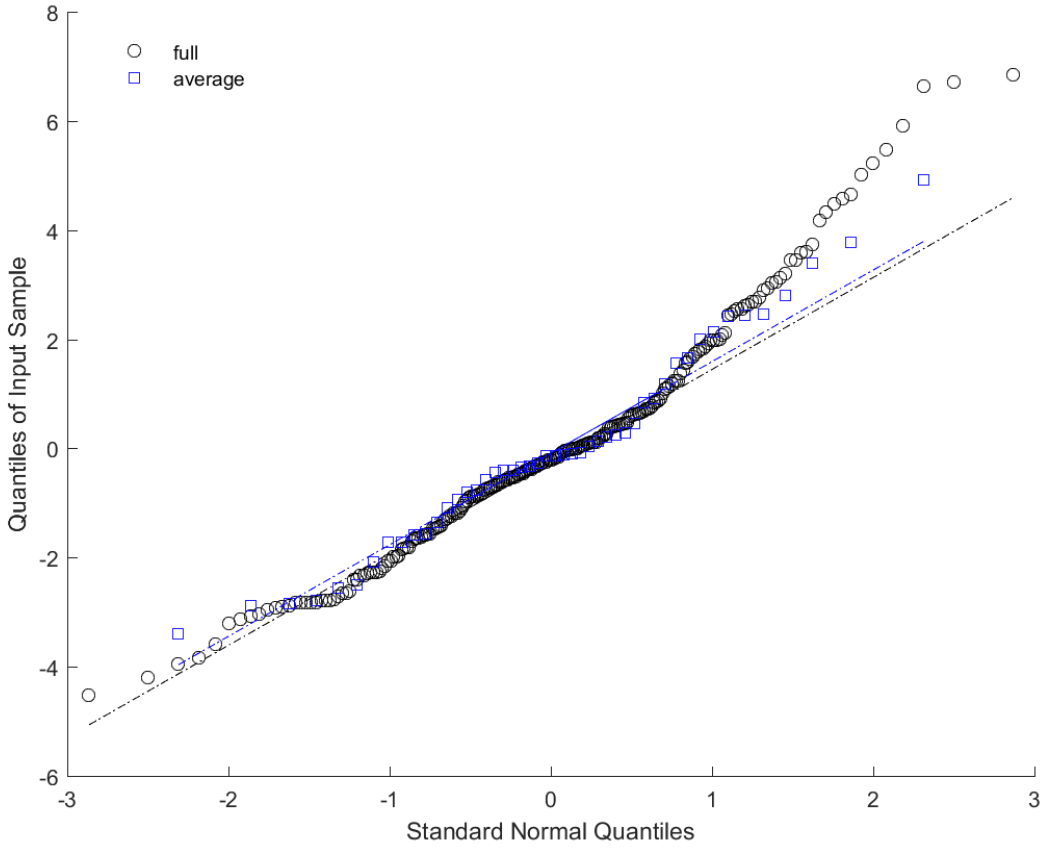


Figure 4.11. Quantile-quantile plot of sample data versus standard normal. Normality can be assumed because the data are reasonably linear by inspection.

Typically, a p-value of $p < 0.05$ indicates strong evidence against the null hypothesis ($H_0$), which would be that there is no difference in temperature rise due to the tested effects of separation distance and crystal adhesion. The F ratio is reported as well as the degrees of freedom between groups and degrees of freedom within groups which were used to determine the p-value. A significant main effect of separation distance on temperature was found, $F(1, 44) = 6.91$, $p = 0.0118$. The null hypothesis was rejected and it was concluded that separation distance has a statistically significant effect on temperature rise. A significant main effect of binder adhesion was also found, $F(1, 44) = 41.28$, $p < 0.0001$. The interaction between the effects of separation distance and binder adhesion on temperature rise was not significant, $F(1, 44) = 1.33$, $p = 0.2553$.

Arguably, a nested model was an equally good approach for the statistical analysis of the experimental data. In this model, the effect of sample number (#1-12) was nested under adhesion effects and adhesion effects were, in turn, nested under separation distance effects. Each sample number had five replications which were not averaged. An added benefit to this approach was that because the sample number was considered a factor, its effect and the relative uncertainty explained by its inclusion could be estimated. Applying ANOVA, the separation distance, $F(1, 192) = 5.00$, $p = 0.0265$, and adhesion, $F(2, 192) = 15.41$, $p < 0.0001$, p-values indicate a statistically significant effect of both factors on the surface temperatures. As before, adhesion was the more significant of the two. A large sample-to-sample p-value, $F(44, 192) = 0.72$, $p = 0.8980$, indicates good sample repeatability and further illustrates that any observed difference in the surface temperature comes from the adhesion or separation distance factors and not from uncontrolled sample-to-sample variations. Had the p-value been low, this would indicate that the effect of sample number was significant.

The higher temperatures reached in the contacting triad configurations, as compared to the separated triad configurations, provides evidence that frictional heat generation occurs at points of crystal contact or that a small area of delamination of the particle/binder interface was initiated from the first run. The low temperatures and lack of obvious heat source of the separated triad samples suggests that viscoelastic heating in the binder and around the inclusions is minimal to negligible. Debonding could allow the binder to move relative to the crystal interface in a sliding or slapping motion and the high frictional heat dissipated can be compounded by heating at particle/particle contact points. Additionally, amplified viscoelastic heat dissipation potentially occurred at debonded locations due to a larger amplitude motion of the binder. There was a possibility that trapped gas spaces created by delamination were repeatedly compressed and contributed to heating, although degassing steps during crystal encapsulation were taken to prevent this.

## 4.5 Conclusions

The thermal responses from ultrasonic tests at 210.5 kHz on a simplified PBX system of three HMX crystals embedded in Sylgard 184 binder were presented. High temperatures achieved in contacting triad as compared to separated triad configurations provide evidence that frictional heating is much stronger than viscoelastic heating in the system under consideration.

Mechanically debonded samples of the same triad geometries (contacting, separated) reached even higher temperatures, as friction can occur when the binder moves relative to the interface and viscoelastic heat dissipation may be amplified by large amplitude motion of the binder. Frictional heat dissipation from points of particle/particle contact and a delaminated and moving binder interface (also a mode of friction) are compounded in the debonded-contacting triad samples which reached the highest average and highest overall maximum surface temperatures.

A two-way ANOVA shows the significance of the effect of separation distance, $p = 0.0118$, and adhesion, $p < 0.0001$, with no interaction of the factors, $p = 0.2553$, on the final 5-run average temperatures of the 48 samples. A nested ANOVA model of the full data set also shows a strong effect of geometry, $p = 0.0265$, and adhesion, $p < 0.0001$, on temperature rise with a high sample-to-sample p-value, $p = 0.8980$.

These results suggest that polymer binder adhesion to energetic crystals is important to mitigate heating from high frequency (~100-1000 kHz) periodic mechanical excitations. The significance of frictional heat generation over viscoelastic heating in these systems may influence future design considerations related to the selection of binder materials for composite energetic materials. Viscoelastic/viscoplastic heating, even in the low solids loaded systems presented here where the potential for significant heating exists, appears minor for these conditions, although it could play an important role during initial heating. Future work should aim at exploring polymer binders other than Sylgard 182/184, investigate damage from the vibration of higher solids loaded systems, and systematically study binder adhesion at particle/binder interfaces and the effect of bonding agents.

# 5 IN-SITU X-RAY OBSERVATIONS OF ULTRASOUND-INDUCED EXPLOSIVE DECOMPOSITION

## 5.1 Introduction

In collaboration with Jesus Mares Jr. formerly of Purdue University, ultrasonic experiments were also performed at Argonne National Laboratory at the Advanced Photon Source using the experimental setup described in the literature [65]. This chapter will briefly describe what was learned from the single crystal and high solids loaded mono-layer samples. Note that portions of this chapter are reproduced from "In-situ X-ray observations of ultrasound-induced explosive decomposition" in Applied Materials Today volume 15, pages 286-287, 2019, with the permission of Elsevier [66]. This chapter is included for context and includes an excellent visualization of HMX melting under ultrasonic insult, rapid binder motion against a crystal interface, delamination initiated during a test, and video evidence showing that high heating rates can be achieved, enough to drive HMX to decomposition. This section also documents the first time a high-solids loading HMX sample was tested (more than ~10 crystals).

## 5.2 Experimental Methods

Samples were fabricated by fully embedding HMX particles within a rectangular block of Sylgard 184, creating a simplified model of a cast-cured PBX. All of the Sylgard 184 material used in this study was doped with 0.01% by mass of iron oxide ($Fe_2O_3$) particles (nominally 44 μm) in order to increase the contrast between the binder and HMX for the purpose of X-ray imaging.

X-ray phase contrast imaging (PCI) was performed with a Photron SA-Z high-speed camera with scintillator to convert the X-ray images into visible light images, a 5× magnification microscope objective and tube lens, and a 45° mirror. The experimental schematic is shown in Fig. 5.1.

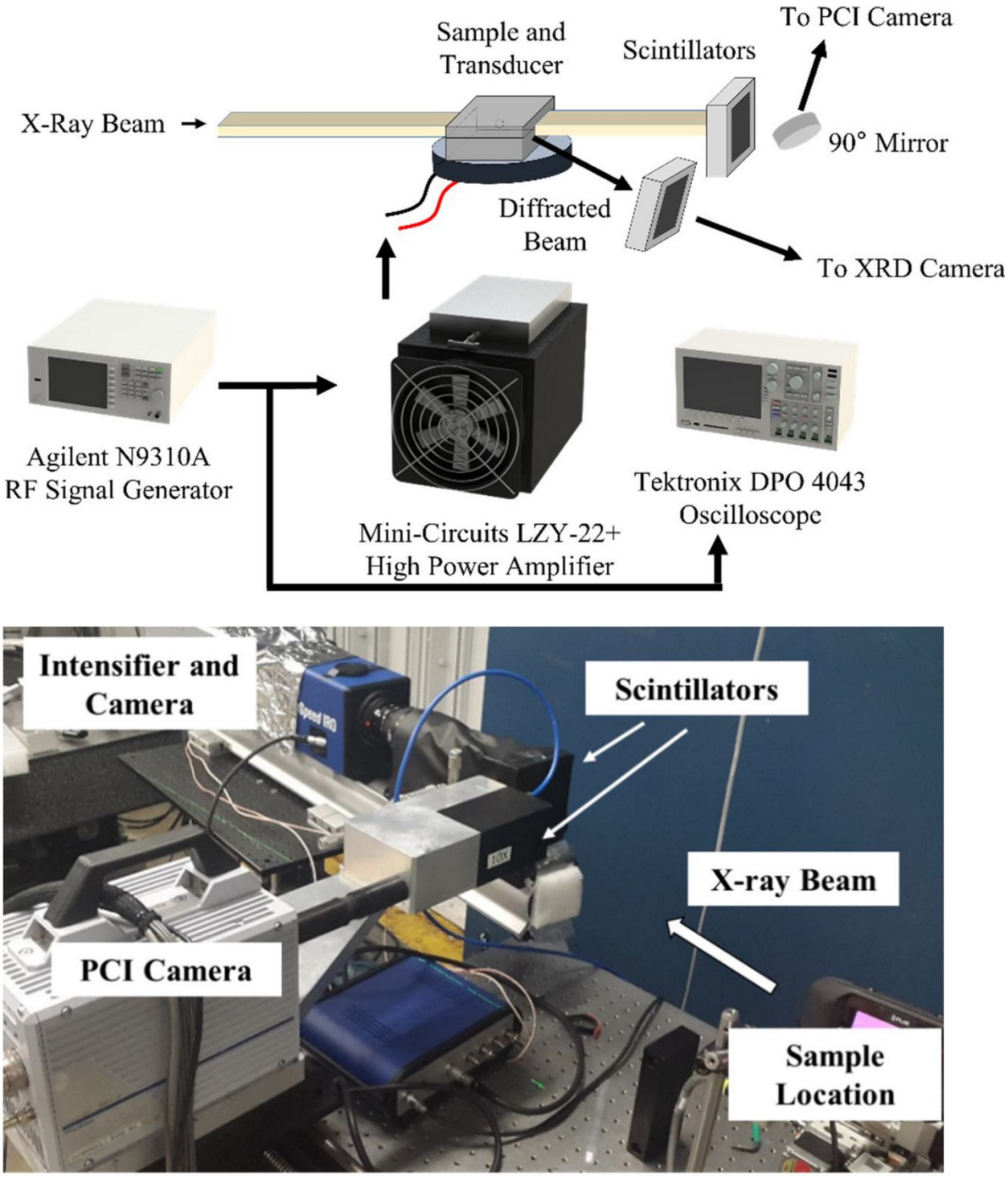


Figure 5.1. A diagram and depiction of the X-ray PCI imaging setup at Argonne National Laboratory Advanced Photon Source, beamline 32-ID-B.

## 5.3 Results and Discussion

Figure 5.2 shows the expansion of the binder and motion against the crystal visualized at 90 kHz with high-speed X-ray PCI. The images were taken as bursts of 256 frames every 1 s due to the restriction of limiting the total time of on-sample radiation to about 12.5 ms to prevent sample heating and scintillator damage. Dark shapes in the binder in Fig. 5.2 are iron oxide agglomerates. The particle shifted upward throughout the test as clearly seen in Fig. 5.2(a) versus Fig. 5.2(f). This effect was attributed to the bulk heating accompanied by thermal expansion of the binder nearest the transducer interface at the bottom of the frame. A distinct cyclic motion at the particle/binder interface was observed at the bottom right crystal interface where cracking occurred in Fig. 5.2(d)-(e). The cyclic motion continued until the end of excitation after the 10 s burst.

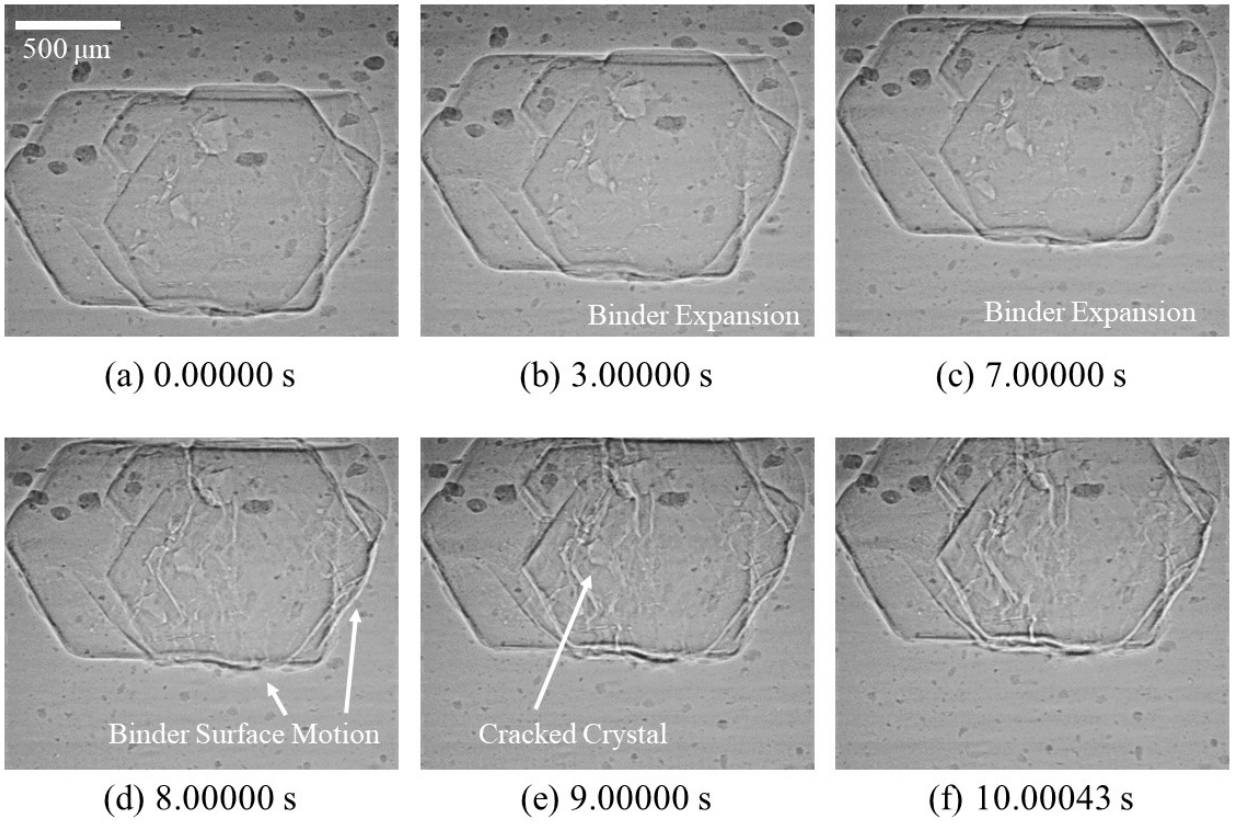


Figure 5.2. Select frames of a single HMX crystal subjected to ultrasonic excitation recorded at 90 kHz in 1 s bursts.

Figure 5.3(a) shows delamination nucleating at a sharp point on the HMX crystal, which spread across the surface with a periodic motion. The crystal cracked and increased in size in Fig. 5.3(c) signifying β-δ phase transformation at an elevated temperature of 170 °C. A liquid motion was observed in Fig. 5.3(d) indicating HMX melting, followed by more binder surface motion in Fig. 5.3(e). Expansion from cavity pressurization by decomposition gas products is observable on the right side of the crystal in Fig. 5.3(f)-(g). Finally, Fig. 5.3(h) shows where the binder surrounding the crystal ruptured and all cyclic motion ceased.

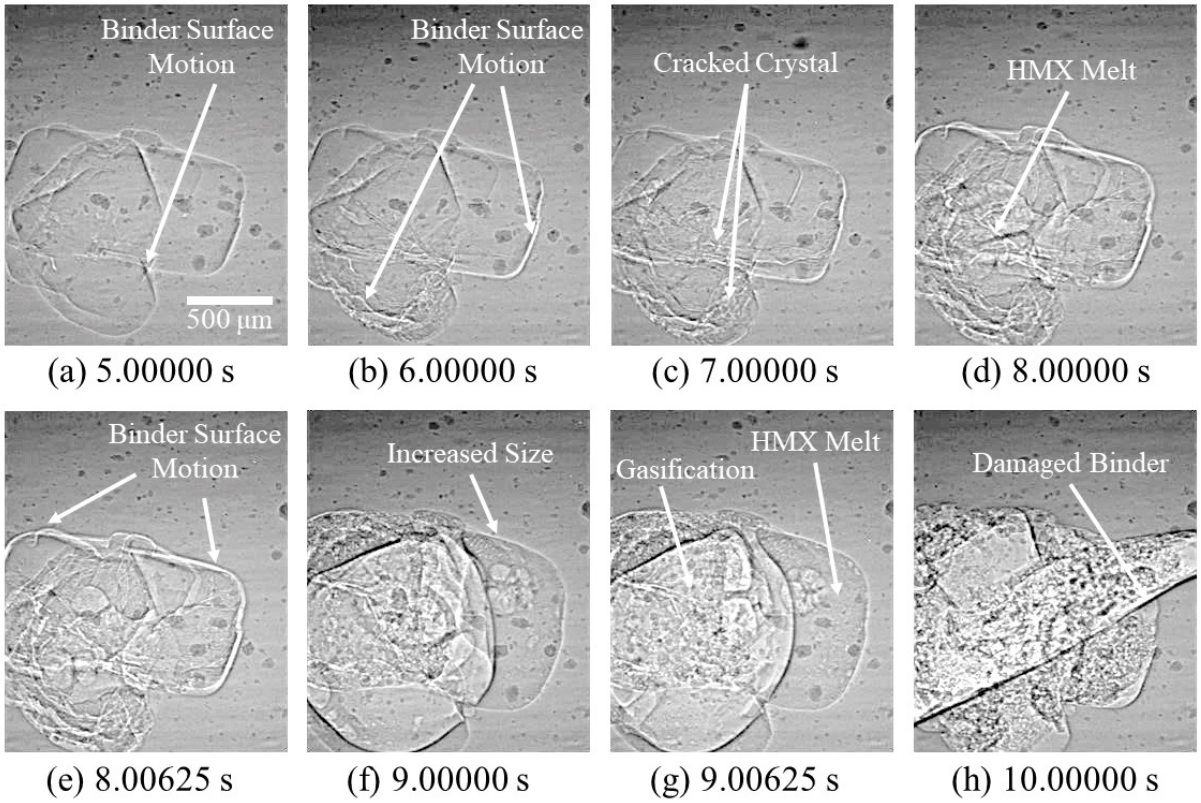


Figure 5.3. Select frames showing the delamination, increased size from phase change, cracking, melting, and thermal decomposition (gas production) of a single HMX crystal under ultrasonic excitation recorded at 80 kHz in 1 s bursts.

The sample in Fig. 5.4 exhibited similar events such as binder surface motion, crystal cracking with an increase in size indicating δ-phase HMX, melting, and then decomposition with gas products which broke out of the binder. One key difference are the 256 frames captured at the 5 s burst mark which showed ‘boiling’ of the HMX melt within the binder cavity. Gasification and melt existed within the cavity and were observed to flow in a rapid, cyclic

motion in Fig. 5.4(f)-(g) as acoustic energy continued to heat the liquid energetic material, resulting in sudden decomposition by the next burst at 6 s.

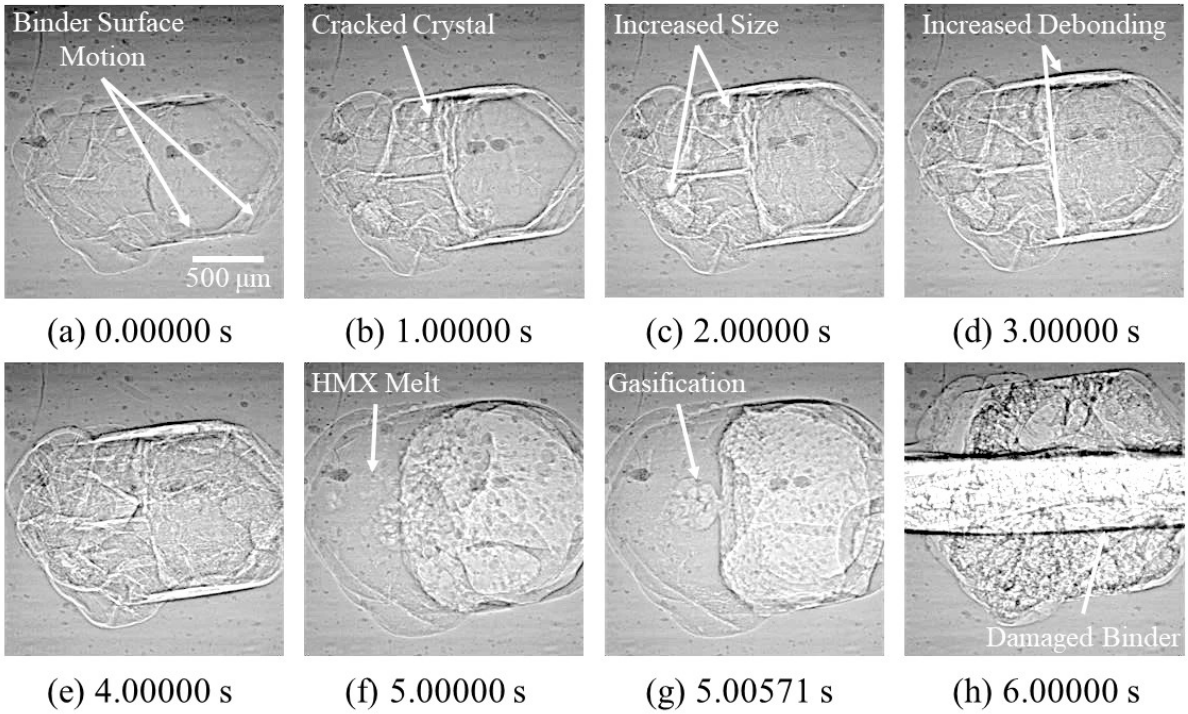


Figure 5.4. Select frames showing the delamination, increased size from phase change, cracking, melting, and thermal decomposition (gas production) of a single HMX crystal under ultrasonic excitation recorded at 70 kHz in 1 s bursts.

A limited number of ultrasonic tests were run on low density single layers of HMX and showed that a site of intense, localized heating (hot spot) was likely at the center of a ring of δ-phase converted particles. This plane of HMX particles was oriented orthogonal to the incident ultrasonic insult, into the viewing axis of the beam/camera. Throughout the duration of ultrasonic excitation of the sample, regions or individual HMX particles exhibited evidence of the formation of HMX melt and gasification for various lengths of time. At each of these locations, which are highlighted in frames 5.5(b)-(f), the formation of HMX melt and gasification was evident at five different locations. In almost all of these cases, these regions had quenched in the next burst of captured images. However, other locations were undergoing transition to an HMX melt which progressed to observable gasification shown in Fig. 5.6. This process of HMX

delamination/melt/gasification and subsequent quenching occurred at multiple localized regions until the application of the ultrasonic excitation to the sample was terminated. A similar response to the high-frequency mechanical excitation was also observed in a second single-layer sample. Due to the configuration of the experiment, with the camera axis in-line with the plane of particles, it was difficult to inspect the dynamic response of the multiple HMX particles for specific particle–particle interactions or record the precise locations at which delamination, melt, or gasification occurred.

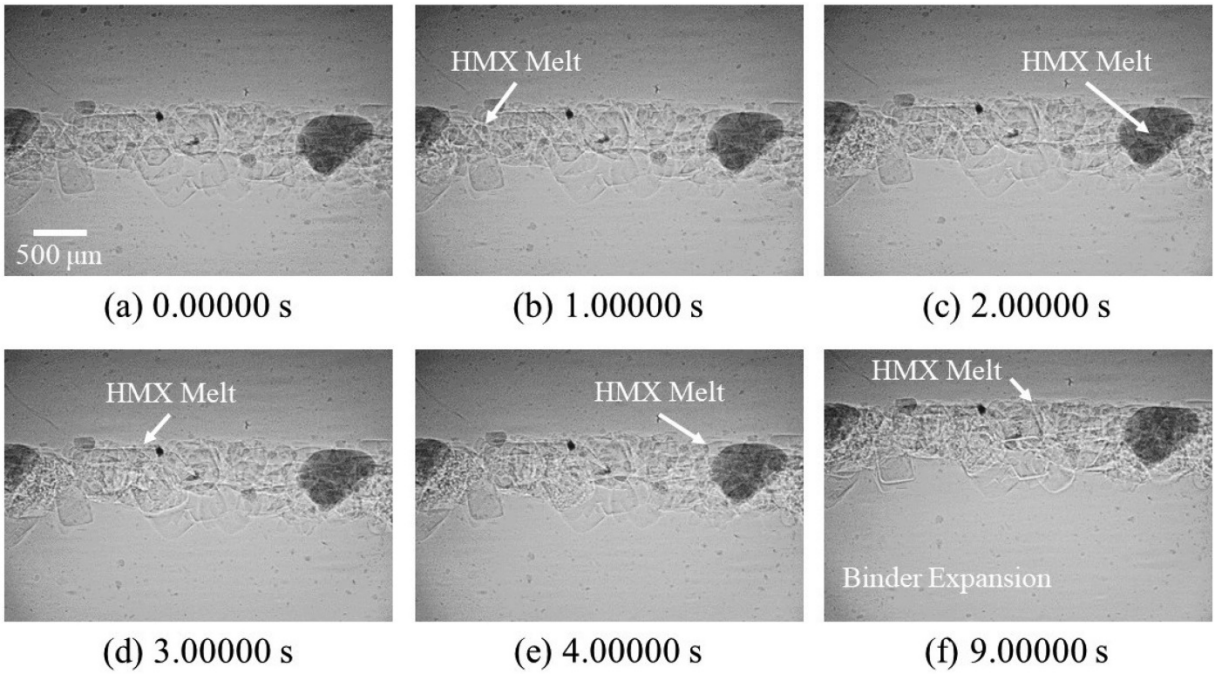


Figure 5.5. Select frames of the X-ray PCI of a multi crystal sample imaged from the side during ultrasonic excitation recorded at 20 kHz in 1 s bursts.

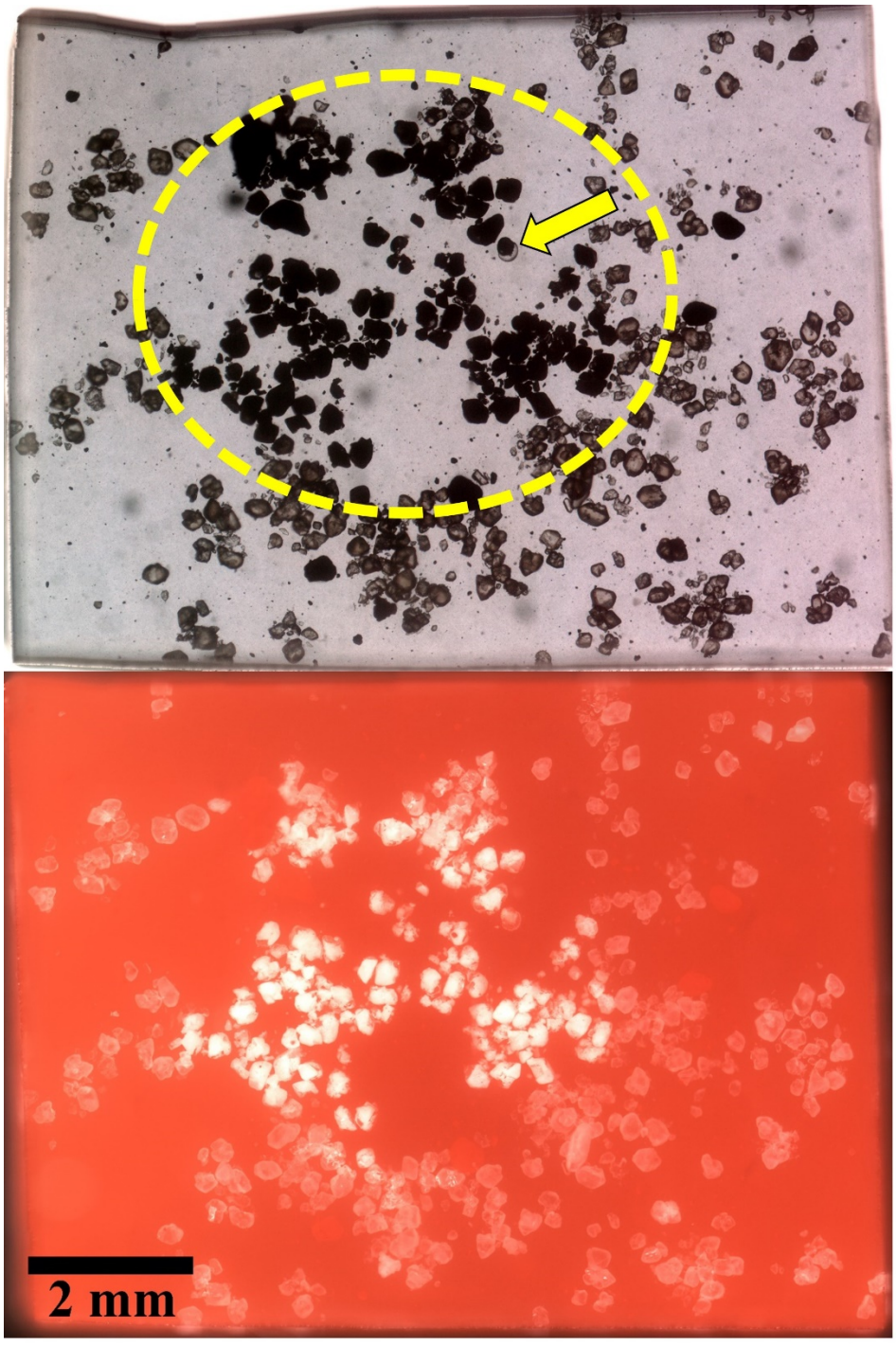


Figure 5.6. Post-test microscope images of the high-solids loaded HMX sample from Fig. 5.5. Both backlighting and top ring-lighting are shown. A circle is drawn around the area of δ-HMX crystals and a possible site of gas production is identified.

## 5.4 Conclusions

Results from the previously demonstrated experiments suggest that the ultrasonically driven chemical decomposition of polymer-encapsulated HMX crystals may occur through a series of three primary heating mechanisms. The initial heating of the regions near the embedded crystals was likely caused by the viscoelastic dissipation mechanical energy as thermal energy at the incident (near) side of the crystal to the transducer. This was analytically and numerically demonstrated by Mares *et al.* [18]. This heat combined with the heat conducted by the transducer. Secondly, the thermal expansion of the binder along with the dynamic stresses along the particle/binder interface caused delamination of the binder from the crystal, allowing for a frictional heating mechanism at the crystal interface via the cyclic motion from the applied mechanical excitation as analyzed in Chapter 4. Localized regions of intense heating (hot spots) on the HMX particle were then driven to chemical decomposition, which allowed for the final additional heat generation mechanism of exothermic reaction.

Delamination of the viscoelastic binder material from the crystal surface due to the thermal expansion and dynamic stresses of the binder appears to be crucial in order for an additional frictional mechanism to occur. As such, the coefficient of thermal expansion of the binder, other mechanical properties of the binder such as stiffness (elastic modulus), and the adhesion between the energetic material and binder materials are of extreme importance in order to suppress this phenomenon of ultrasonically driven decomposition.

# 6 MESOSCALE OBSERVATIONS OF THERMAL DECOMPOSITION OF ENERGETIC COMPOSITES UNDER ULTRASONIC EXCITATION

## 6.1 Introduction

The objectives of this chapter were to investigate the conditions for, and locations of, hot spot initiation of energetic crystals embedded within a polymer binder subjected to periodic, mechanical excitation from a contacting transducer operating at 210.5 kHz. Crystal and binder interactions and events such as solid-solid phase change and gas production were observed in real-time via optical microscopy. HMX crystals of five types (β-HMX, pre-delaminated β-HMX, δ-HMX, recrystallized β-HMX, and rounded recrystallized β-HMX) exhibiting distinct morphologies were encapsulated within a transparent Sylgard 184 binder and subjected to high frequency insult from a contacting piezoelectric transducer and observed via high-resolution optical microscopy. Note that portions of this chapter are reproduced from "Mesoscale observations of thermal decomposition of energetic composites under ultrasonic excitation" in the Journal of Applied Physics volume 125, issue 21, paper 215114, 2019, with the permission of AIP Publishing [67].

The objectives of this current work are to more fully understand the influence of the considered heat generation mechanisms in periodically insulted composite energetic materials, such as PBXs and solid propellants, by examining evidence of hot spots (delamination, melting, phase change, and multiple stages of gas production) induced by heating from the motion of a polymer binder near or against varying HMX crystal surfaces. Pathways of energy dissipation are identified and steps which could be taken to mitigate against this heating are discussed.

## 6.2 Sample Preparation

Samples were prepared with BAE Systems grade B class 3 HMX sieved to 500-850 μm. The crystals were encapsulated in Sylgard 184 (polydimethylsiloxane), an optically transparent elastic binder suggested for use in PBXs, [35, 37] in two steps. First, a 1 mm layer of Sylgard was mixed at a 10:1 base to curative ratio, and cured at 60 °C for 12 hrs. Next, crystals were arranged on the surface of the 1 mm layer and encapsulated with approximately 3 mm of

additional Sylgard before curing in the oven again. Care was taken to subject the embedded crystals to vacuum before final curing in order to draw bubbles away from the crystal interface and facilitate good binder contact. Finally, approximately 5 mm × 7 mm Sylgard rectangles with encapsulated HMX 1 mm below the top surface were obtained using a razor blade.

In addition to production-grade β-HMX, the following three types of HMX crystals of the same size range were encapsulated: δ-HMX which was created by heating the crystals above 170 °C for several minutes before encapsulating and was characterized by a rough, cracked surface due to the approximately 7% volume expansion accompanying the transition, [48, 68] recrystallized β-HMX with few surface or internal defects, and recrystallized β-HMX which was agitated in acetone for 1 min to remove sharp corners and round the flat sides. An example of the rounding process is shown in Fig. 6.1. Additionally, pre-delaminated production-grade β-HMX samples were created by manually compressing the cured Sylgard rectangles until the binder was observed to peel off of the crystal surface without damaging the encapsulated crystal. Images of representative HMX crystals of each type are shown in Fig. 6.2.

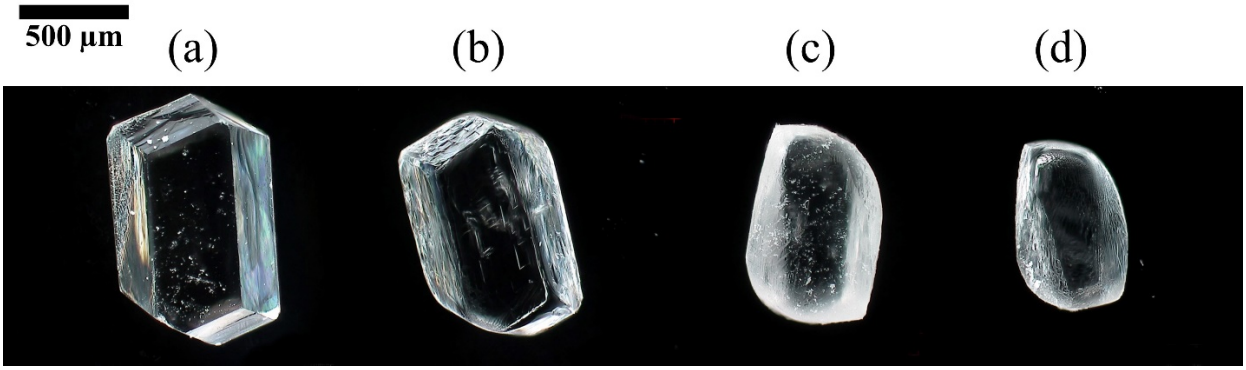


Figure 6.1. Recrystallized HMX (a) before agitation in acetone, (b) after 1 min, (c) 2 min, and (d) 3 min.

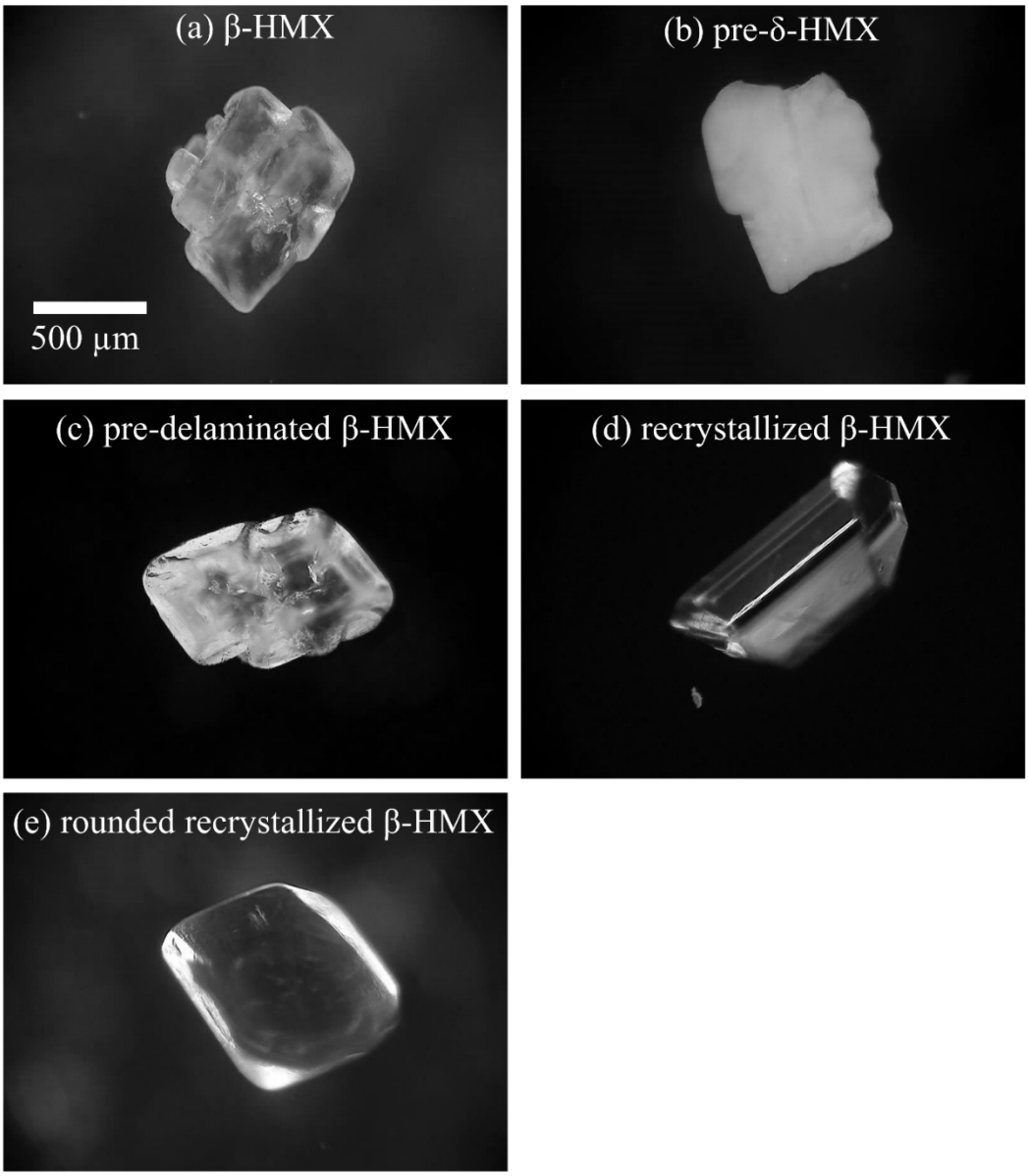


Figure 6.2. Images of representative HMX crystals embedded in Sylgard used in this study. These stills were taken from actual test samples.

Recrystallization of the β-HMX was performed using a Soxhlet extraction process to remove impurities, immersion in cyclohexanone for 6 hrs to remove RDX contaminant (maximum 2% RDX per MIL-DTL-45444C), and finally the crystals were dissolved in 3:1 acetone:nitromethane and stirred for several hours before allowing slow evaporation and crystallization on the bottom of a glass container.

An Agilent N9310A RF signal generator and Mini-Circuits LZY-22+ high power amplifier powered by a Keysight E3634A DC power supply, detailed in depth in Roberts *et al*. [19], provided a 10 W sinusoidal signal at 210.5 kHz to a Steiner and Martins SMD10T2R111WL PZT transducer. Strong coupling between the piezoelectric transducer and the Sylgard sample containing the embedded HMX crystal was found to be extremely important to induce crystal/binder delamination and for high heat generation at the inclusion location. Cyanoacrylate (Loctite gel control superglue) was used to adhere the Sylgard sample to the surface of a transducer that had been blackened with a permanent ink marker (Sharpie). A Hirox KH-8400 optical microscope with 140× lens recorded video at 24 fps with a resolution of 800 × 600 pixels (1.4 μm/pixel). Due to the inexact start time of the recordings, excitation begins tens to hundreds of milliseconds into each video. Tests were terminated after 15 s, about when heating from the transducer begins to influence ultrasonically driven heating at the particle location (Fig. 6.3). The insets show the sample at 0 s, 4.00 s, 8.00 s, and 15.00 s. Microscope videos were captured from a top view with the blackened transducer oriented behind the crystals. Side view videos were typically lower quality due to the increased depth of binder and did not reveal information about whether the delamination first takes place on the near side of the crystal to the transducer or at surface asperities exclusively.

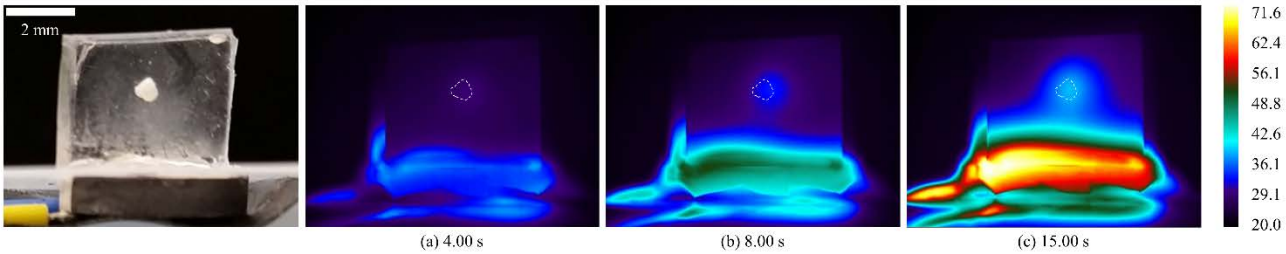


Figure 6.3. Side view from a FLIR A325sc infrared camera of a pre-delaminated β-HMX sample which transitioned to δ-phase. The transducer is also shown as well as a white dashed outline around the crystal location. The sample was modified to have a particle embedded 1 mm from the side wall to obtain a more differentiated temperature pattern. This image sequence was used to determine the end time of 15 s, about when heat conducted from the transducer first tangibly influenced the ultrasonically driven heat at the particle location.

## 6.3 Results and Discussion

The initial time of events observed in each of the 15 samples among four sample types during excitation are given in Fig. 6.4 and Fig. 6.5. The fifth sample type, rounded recrystallized β-HMX, had no response in any of the 15 samples within the 15 s tests. The point markers indicate times at which samples showed evidence of delamination characterized by a visibly moving binder against the crystal, β-δ phase change indicated by an increase in size and opacity of the crystal, gas production seen as expansion of the cavity and bubbles forming in an HMX melt within the Sylgard, and additional gas production events up to three times in some tests.

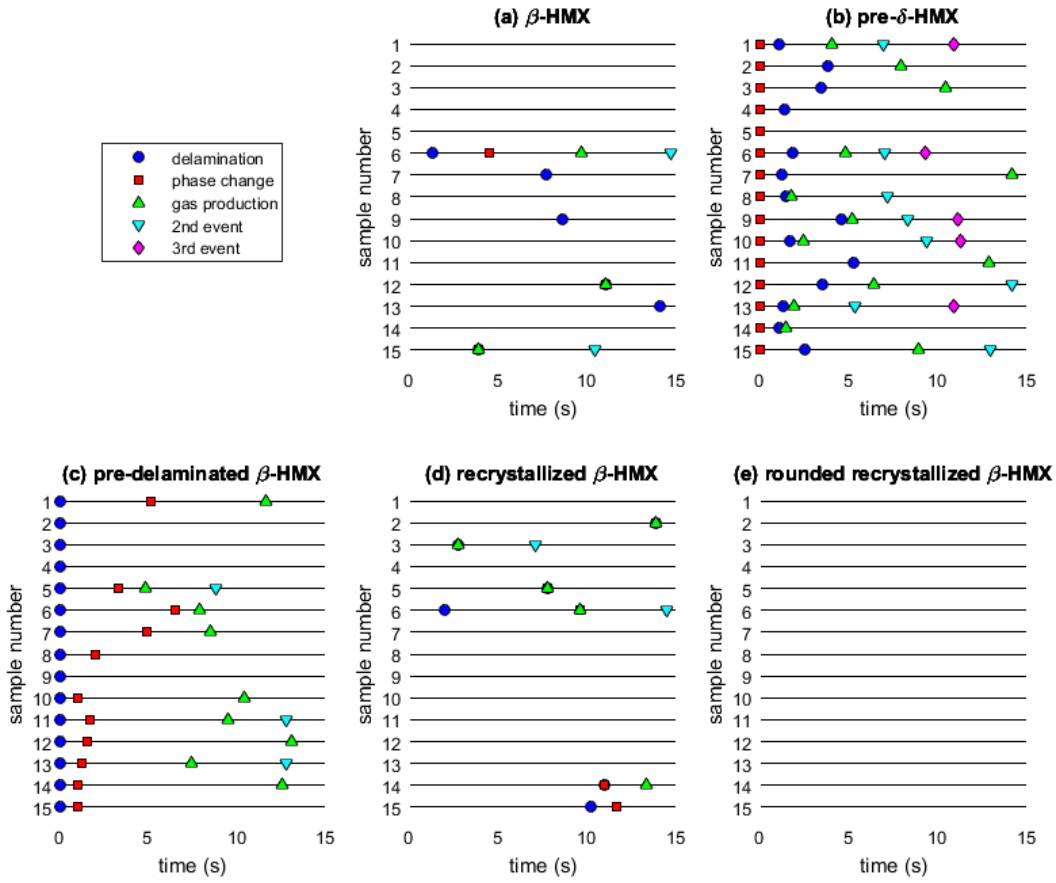


Figure 6.4. Timelines of events observed for different HMX samples. Another visualization of this data is given in Fig. 6.5.

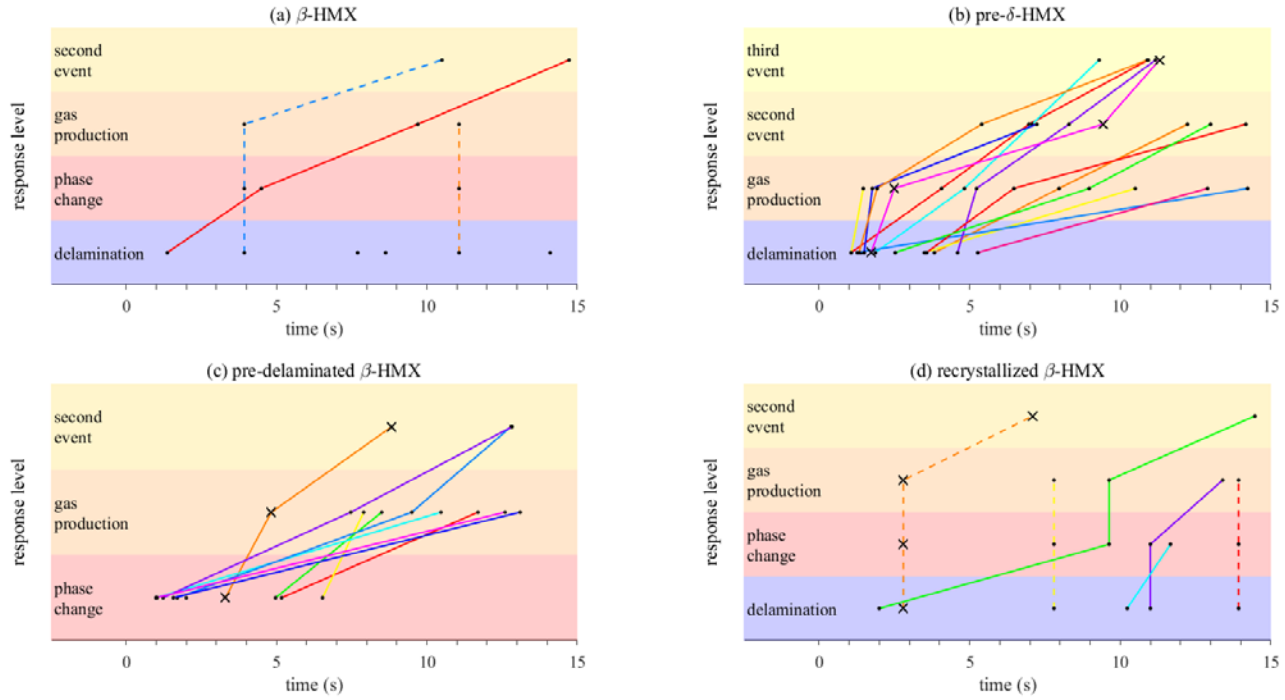


Figure 6.5. Time of events observed during the 15 s duration tests for 15 of each embedded, single crystal HMX samples: (a) β-HMX, (b) pre-δ-HMX, (c) pre-delaminated β-HMX and (d) recrystallized β-HMX. Rounded recrystallized β-HMX had no responses within 15 s. The events beyond initial delamination, phase change, and gas production included re-solidification, melting, and additional gas production before breaking out of the cavity/plane of casting in some cases. Dashed lines represent samples that had no visible delamination before gas production and 'X' data are samples shown in subsequent image sequences.

The scarcity of events in production-grade β-HMX samples in Fig. 6.5(a) was contrasted by the pre-delaminated β-HMX samples shown in Fig. 6.5(c). A delaminated and moving binder interface was characteristic of energy dissipated frictionally, or by the compression of created voids. Heat generated at the outer surface locations on a crystal was enough to drive the HMX to thermal decomposition, as evidenced by the melting and gas production of the pre-delaminated β-HMX shown in Fig. 6.6. Gaseous products expanded the cavity of casting and in some cases broke out of the binder in the plane of casting after one or more gas production events, sometimes audibly. It was not always the case that the binder was observed to delaminate and move rapidly against the crystal surface before the HMX underwent the β-δ phase change characteristic of reaching 170 °C, or thermal decomposition, which occurs at 290 °C at slower heating rates [48].

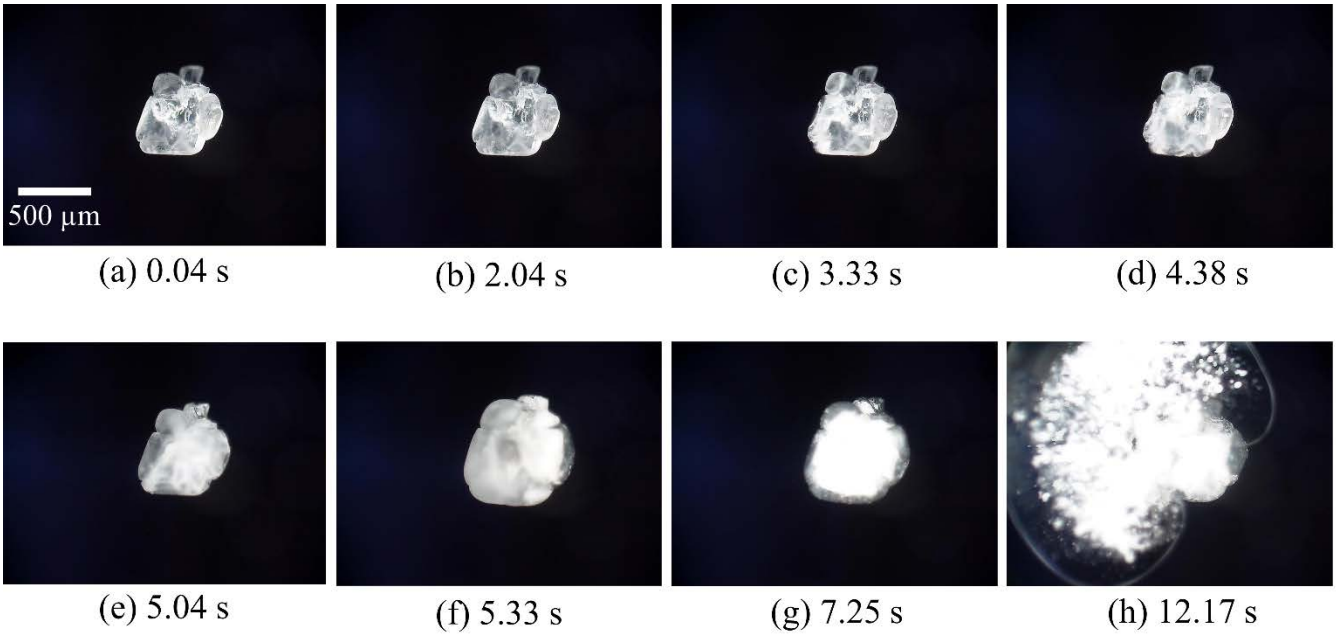


Figure 6.6. Image sequence of the top view of a single, embedded, pre-delaminated β-HMX crystal during excitation. (a)-(b) The delaminated binder moved rapidly against crystal interface, (c)-(d) the β-δ phase change began at the left edge of the crystal, (e)-(f) initial gas production expanded the cavity of casting, (g) gas production ceased and the cavity shrank slightly, and (h) a second gas production event occurred and broke out into the plane of casting.

Defects in crystal morphology provided nucleation points for binder delamination [69] in pre-δ-HMX samples having a rough, cracked surface. A pre-δ-HMX sample is shown in Fig. 6.7 and all of the events for samples of this type are shown in Fig. 6.4(b). Most δ-phase crystal/binder interfaces delaminated immediately upon excitation, and gas production events were more prevalent than with any of the varieties of β-HMX samples. The second and third events after initial gas production appear to be HMX solidifying after having melted and then re-melting and producing gas again. This could happen multiple times during a 15 s test and was usually terminated when the gas broke out into the plane of casting, quenching the reaction. This was further evidence that friction was a main heat generation mechanism because once having melted, friction between the moving binder and the crystal would be significantly reduced, allowing the temperature to drop enough for the HMX to re-solidify before starting the process again. Had significant viscoelastic heating been present in the rapidly deforming binder, heat conduction would have still been able to reach the melted HMX and continue to drive the reaction.

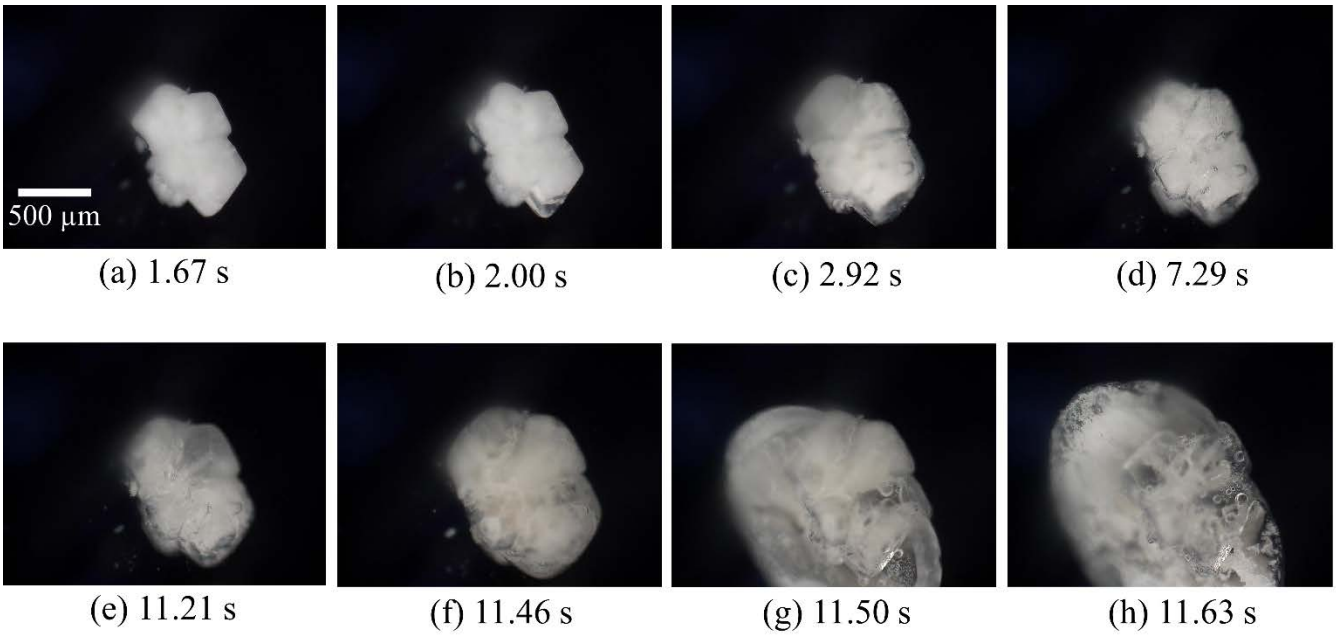


Figure 6.7. Image sequence of the top view of a single, embedded, pre-δ-HMX crystal during excitation. Note the opaque white color of the crystal. (a) The initial δ-phase crystal, (b) first sign of delamination and binder motion, (c) first gas production event, (d)-(e) the cavity shrank and additional surface motion was recorded, and (f)-(h) the second gas production event and growth of the cavity until breakout.

The recrystallized β-HMX in Fig. 6.8(d) was characterized by flat facets; sharp edges and corners; and a clear, low porosity crystal. Some videos of the recrystallized β-HMX showed no visible delamination before the crystals transitioned to δ-phase, melted, and produced gas, as early as 2.80 s, as shown in Fig. 6.8. The lack of visible binder motion before melting and gas production provided evidence that there was another pathway for heating, such as viscoelastic heat generation in the binder near the crystal, enough to drive the HMX to thermal decomposition, as supported by Mares *et al.* [18]. Two β-HMX samples, indicated by dashed lines, also achieved gas production without prior crystal-binder delamination being observed. Rounded recrystallized β-HMX lacked any delamination, phase change, or gas production events and again highlights the influence of crystal morphology on either frictional heat generation from a delaminated and moving binder or localized viscoelastic heat generation without visible delamination. The smooth, corner-less surface did not allow delamination to initiate or propagate

or for concentration of stress in the binder near any sharp crystal points as may be the case for other types of β-HMX.

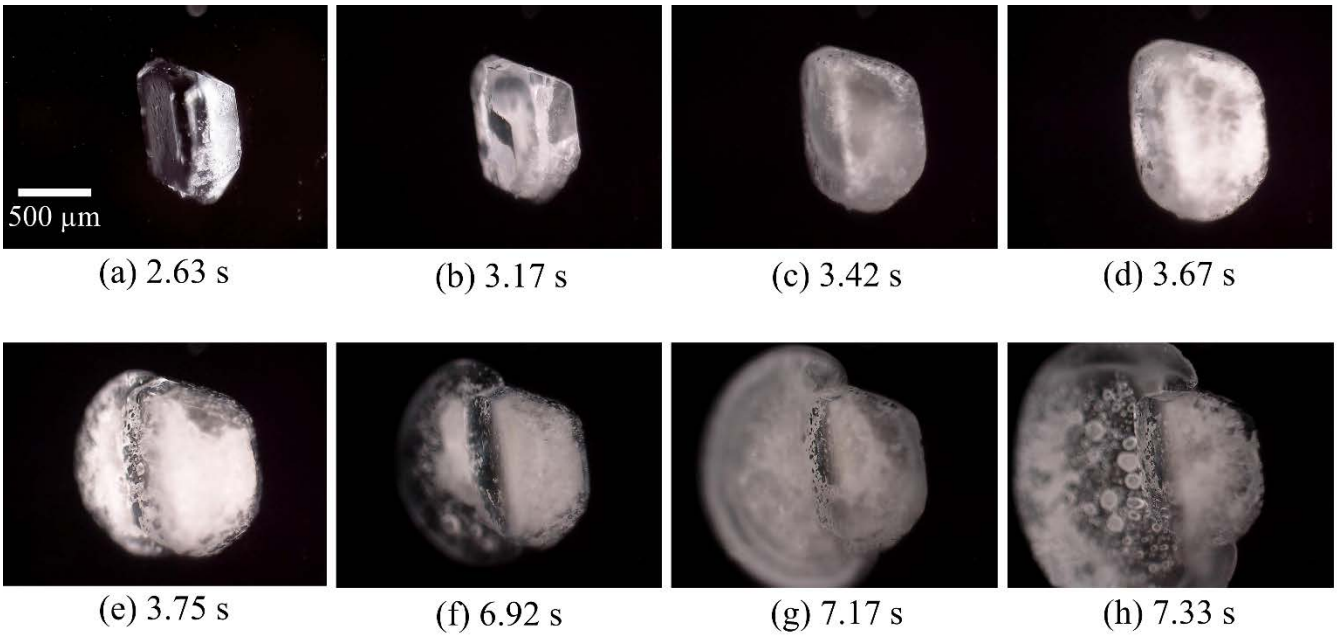


Figure 6.8. Image sequence of the top view of a single, embedded, recrystallized β-HMX crystal (sample #3). Note the flat facets, sharp corners, and clear initial appearance of the low-defect crystal. (a) No delamination or movement was observed for approximately 3 s, (b) initial delamination and melting occurred almost simultaneously, (c)-(d) gas was produced which expanded the cavity of casting, (e) the gas products broke out into the plane of casting, and (f)-(h) after approximately 3 s of additional excitation the crystal melted and produced gas for a second time.

## 6.4 Conclusions

These experiments show evidence of both frictional and viscoelastic heat generation mechanisms contributing to the decomposition of HMX crystals embedded within Sylgard 184 binder and subjected to ultrasonic excitation. Production-grade β-HMX crystals did not typically delaminate or heat enough to undergo decomposition unless the crystal/binder interface had been damaged (mechanically pre-delaminated) which has been shown previously [19].

Crystals which were thermally damaged before encapsulation, called pre-δ-HMX here, showed rapid motion of the binder immediately upon excitation due to the many delamination nucleation points on the crystal surface, leading to quick debonding. The impact sensitivity of δ-

HMX is known to be higher than that of β-HMX due to chemical rather than physical differences alone [68] and δ-HMX is seen to form just before ignition [52, 53]. In this present situation, δ-HMX appears also to be more sensitive to ultrasonic excitation leading to decomposition earlier because of the propensity to delaminate, and β-HMX crystals appear to change phase to δ-HMX and melt just before decomposition. It is expected that frictional heat generation from the binder motion contributes largely to the melting and gas production in the pre-δ-HMX and pre-delaminated β-HMX samples because viscoelastic heat generation in the binder would require conduction to heat the crystal and an intermittently contacting binder or melted interface may decouple this particular source. Additionally, δ-HMX had up to three gas production events during a single test, which, in agreement with current literature stating that the binder confinement influences the chemical kinetics of the explosion [29], also suggests that heating terminates upon interfacial melting of the crystal, indicative of a frictional mechanism.

Recrystallized β-HMX decomposed as quickly as 2.80 s without any visible binder delamination, which is indicative of viscoelastic heating forming a hot spot in the binder next to the crystal, possibly near sharp corners. This was contrasted by the rounded recrystallized β-HMX samples in which no events were recorded, highlighting the significance of surface morphology on initiating binder delamination and possibly influencing viscoelastic heat generation and localization. Correlations could be made between the less sensitive rounded, low porosity HMX presented here and reduced sensitivity-RDX (RS-RDX) seen to be less sensitive to shock stimuli in cast PBX configurations. RS-RDX has similar rounded characteristics, as shown in SEM images, although the authors Lochert *et al*. [70] indicate that there remains to be an analytical technique to identify and classify an RDX as insensitive other than measuring the shock sensitivity of cast PBXs, or how reduced shock sensitivity translates to other reduced sensitivity benefits.

These results indicate that formulations that address the initiation sensitivity of PBXs to contact ultrasonic insult by increasing binder adhesion to mitigate heating may only address one of the available pathways of energy dissipation. Additionally, the counterintuitive results that rough morphology creates nucleation points for delamination rather than to help adhesion, and that the low-defect recrystallized β-HMX could react even without visible delamination, indicate that crystal and binder selection should be a joint design decision. Rounded recrystallized β-HMX appears to be insensitive to initiation for these ultrasonic excitation conditions and times.

A PBX consisting of rounded particles, in contrast to faceted crystals, coupled with a binder having strong adhesion, would be expected to result in decreased vibrational heating and have a low probability of explosion. Future work should focus on the location of initial ultrasonically initiated delamination with respect to transducer orientation and explore other energetic crystals having different melting temperatures, decomposition temperatures, and morphologies.

# 7 HIGH-SPEED MICROSCOPY OF ULTRASONICALLY INITIATED POLYMER BONDED EXPLOSIVES

## 7.1 Introduction

The objectives of this chapter are to develop a detailed understanding of the formation mechanisms and dynamics of hot spots during periodic, mechanical insult of PBXs, specifically in the high frequency range of 100-1000 kHz. Furthermore, the applicability of knowledge gained from studies of mechanisms present in single crystal configurations is addressed and expanded upon using a shadowgraphy technique to observe hot spots near multiple energetic crystals embedded within a transparent binder. Hot spots appear as darkening areas within the transparent binder due to the refraction of light induced by a reduction of density through temperature gradients.

Testing a variety of energetic materials highlights important properties which influence heat generation leading to the ignition of PBXs. Previous ultrasonic studies have focused on fully dense PBX 9501 [25], and countable embedded inclusions of AP [16, 26], HMX [15, 16, 19, 29, 42, 67, 71], and RDX [16, 28, 29, 42].

High solids-loadings and bimodal distributions of particle sizes better approximate standard formulations in ultrasonic tests. A variety of secondary explosive crystals with different melting temperatures, morphologies, and decomposition rates are tested to explore the parameter space and recommendations are formed based on damage/heating observations and the likelihood of several samples to be driven to decomposition. This study includes comparisons between PETN agglomerates, recrystallized PETN, ‘insensitive’ I-RDX, RDX, CL-20 agglomerates (hexanitro-hexaazaisowurtzitane), recrystallized CL-20, TNT/CL-20 cocrystals, HMX, δ-HMX, and recrystallized HMX.

## 7.2 Sample Preparation and Testing Procedures

PETN agglomerates were sieved >500 μm from detonating cord. Recrystallized PETN crystals were shattered into approximately 500 μm sized particles. Eurenco I-RDX, marketed as an RDX variation less sensitive to shock initiation in cast formulations, was sieved for the largest particles sizes present, > 250 μm [70, 72]. δ-HMX >500 μm was created on a hot plate by raising

production-grade β-HMX to approximately 200 °C for several minutes and removing the crystals after visible transformation to δ-phase had occurred. Phase change was identified by a 7% volume increase and change to an opaque white coloring [48]. Grade B class 3 β-HMX crystals from BAE Systems were used, which have a bi-modal size distribution. Recrystallized β-HMX was created by the process described in Roberts *et al.* [67]. TNT/CL-20 cocrystals of 1:1 molar ratio were also sieved to >500 μm [73, 74].

Melting points of the tested explosives ranked from lowest to highest are: (TNT) 80 °C, (PETN) 140 °C, (RDX) 205 °C with decomposition, (CL-20) 247 °C with decomposition, (HMX) 285 °C with decomposition and a solid-solid phase transition at 170 °C [73, 75].

Shadowgraphy (backlit imaging) was performed with a Vision Research Phantom v5.1 operating at 500 fps, 200 μs exposure time, and 1024×1024 color pixel resolution recording. The camera was equipped with an Infinity K2 lens with CF-2 objective and 2× TX Tube magnification, as shown in Fig. 7.1. An LED Streamlight Microstream flashlight was used for backlighting of the sample. The front face of some samples were recorded simultaneously with a FLIR A320sc infrared camera with a FLIR T197200 close-up 2× lens at 30 fps. Note that this implementation is a modified shadowgraphy set-up because the camera directly captures the object instead of the projection of the light rays on a screen.

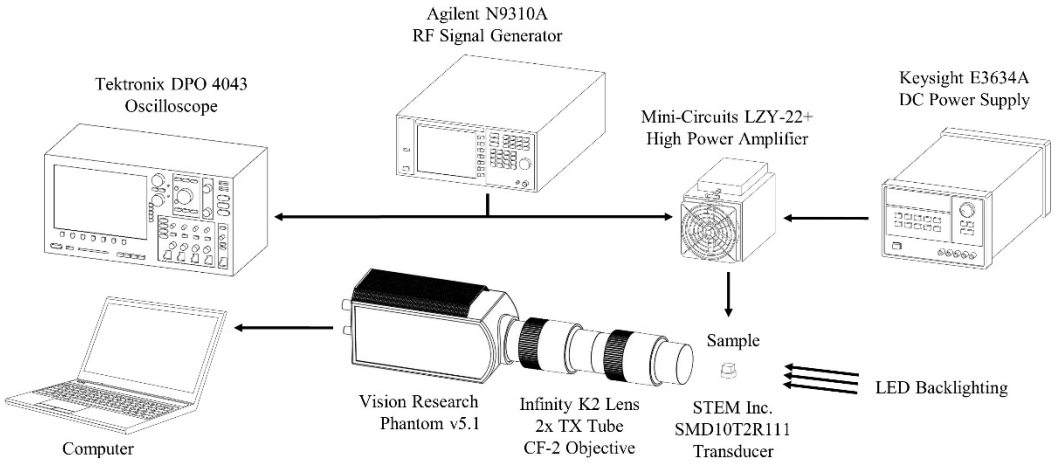


Figure 7.1. Experimental schematic depicting a sample glued on top of a transducer, high-speed camera and light source, and the excitation signal generating equipment.

Samples were cast in two halves starting with ~3 mm of Sylgard 184 mixed in a 10:1 base to curative ratio and then degassed under vacuum and cured at 60 °C for 12 hrs. Crystals were deposited on top of another ~3 mm liquid layer of Sylgard, which then sank to the middle interface. Another degassing step to remove bubbles near the crystal surfaces was performed before curing at 60 °C for another 12 hrs. Final crystal-centered samples were cut with a razor blade to the dimensions of 7.25 mm (height) × 9.75 mm (width) × 5.50 mm (depth) with respect to the camera orientation.

The direct observation of thermally induced explosions is difficult due to the unpredictability of time of explosion. Therefore, image sequence timing started at the first detection of motion, allowing 1-10 s to elapse before recording began. The camera captured about 8 s of footage at this frame rate and resolution. Multiple runs were performed on most of the samples with an approximately 10 min cool-down time between runs to allow heat dissipation in the sample and also prevent de-soldering of the transducer leads during extended operation. The bottom of the Sylgard/energetic composite samples were attached to the transducer with Loctite Gel Control super glue with the transducer oriented at the bottom of each image. ‘Before’ and ‘after’ images were taken with a Hirox KH-8700 microscope and stitched together with Microsoft Image Composite Editor.

## 7.3 Results

Spatially small, intense thermal gradients identified as hot spots were visualized by ‘lensing’ and darkened areas in the binder and regularly formed on the near-side interface (closest to the transducer) of inclusions and at crystal/crystal contact points, even deep within the sample. Hot spots were seen to move along delaminated and melted crystal/binder interfaces and gas products escaped through these paths.

### 7.3.1 PETN

Preliminary single agglomerate PETN samples demonstrated that over many runs, and even within the same test, the agglomerate would melt, re-solidify, and melt again in a cycle. This phenomenon was also seen in high solids-loaded PETN agglomerate samples which could be cycled to melt and re-solidify multiple times. During cycles, decomposition could occur which was identified as an expansion of the binder pockets where the melt was contained.

Typically, after the transducer excitation was turned off, the melt remaining in the binder cavity would take several seconds to revert to a solid state, indicative of latent heat in the sample requiring a cooling down period. Five out of the six PETN samples tested resulted in a breakout of the melt and an accompanying expansion of the binder cavities due to pressurization from the decomposition gas products. The lone sample not resulting in any decomposition was run four times with only lensing, melting, and some minor cavity expansion observed. The PETN agglomerates were porous, and once melted, only occupied a portion of the cavity formed during encapsulation. During the tests the melt layer rapidly moved and bubbled within the binder cavity, but 500 fps was generally fast enough to capture the bulk motion of the liquid PETN. Since the samples were cast and cured with particles between them, the weak interface is vertically oriented in the image sequences shown here.

Figure 7.2 depicts the second run of a PETN agglomerate sample. During the first run, the upper most central inclusion melted as did the surrounding two inclusions. During the second run, first motion was detected in Fig. 7.2(a) with frame Fig. 7.2(b) showing the first melt occurred at a new location. The melt was indicative of achieving a temperature of 140 °C. In Fig. 7.2(c)-(d) agglomerates around the initial hot spot began to melt. Furthermore, in Fig. 7.2(e) the first sign of gas products broke out with melt from the binder cavities along the weak vertical interface. Figure 7.2(f)-(h) show the melt and decomposition products escaped through the top surface of the sample, with accompanying audible sound.

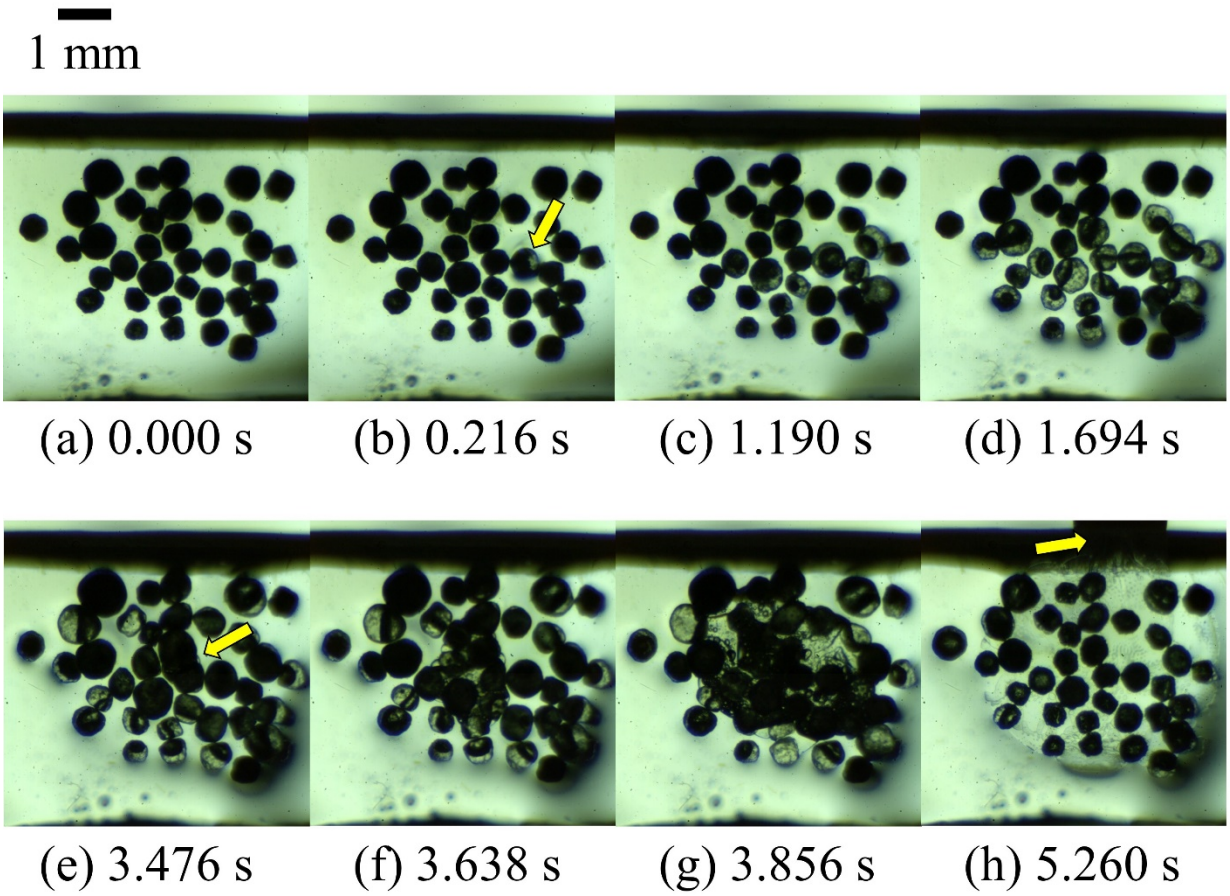


Figure 7.2. The second run of a PETN agglomerate sample recorded at 500 fps with backlighting.

Two samples of recrystallized PETN were tested and, similar to PETN agglomerates, began to melt immediately upon excitation, as expected due to the low melting point. Fig. 7.3 shows an image sequence of one of the recrystallized PETN samples. Note the jagged morphology and smaller periphery crystals which were created from the fracture of a larger crystal. Melting occurred on the first run of the sample in Fig. 7.3 and gas production began at the lower-most crystals closest to the transducer interface, which also contributed to the crystal heating conductively. In Fig. 7.3(b)-(c) the first sign of a hot spot causing melting began at a crystal/crystal interface. Heat spread to the adjacent crystals as the temperature rose above the melting point (140 °C) in several crystals in Fig. 7.3(d)-(f). Figure 7.3 (g)-(h) show that the decomposition gas products pressurized the lower-most binder cavities, distorting the image through thermal expansion of the binder, and broke out along a connected series of cavities

containing melt in Fig. 7.3(i)-(k). This eventually opened a large void along the weak casting interface as seen in the ‘after’ image Fig. 7.3(l), but did not escape the block of binder.

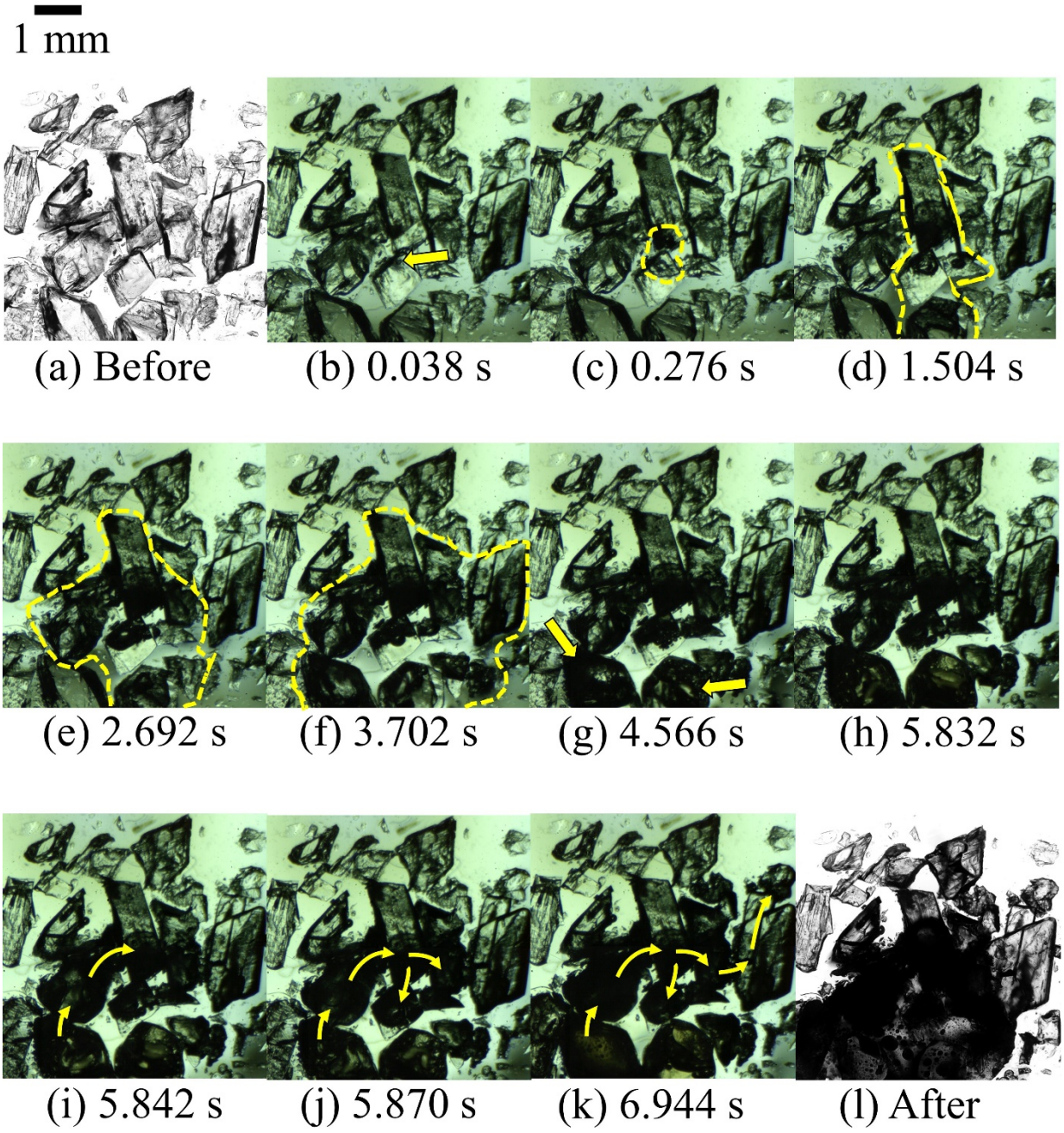


Figure 7.3. Recrystallized PETN recorded at 500 fps with backlighting. ‘Before’ and ‘after’ images were taken with a Hirox microscope.

### 7.3.2 RDX

The identification of crystals likely to delaminate and melt can be done by observing the ‘lensing’ or dark spots in the binder where thermal gradients are high. Figure 7.4 shows two runs of I-RDX sample 1. I-RDX crystals were characterized by small, spherical features and were of a smaller size range than production-grade RDX. Figure 7.4(b)-(d) show the development of a hot spot on the uppermost crystal in the cluster. This was the farthest crystal location away from the transducer which was located on the bottom interface (the thin plastic transducer support is visible at the bottom of the frames). This suggests that there may have been a defect in the crystal/binder interface at that location or that delamination was initiated here due to peak pressure from the constructive interference of acoustic waves in the nearfield of the transducer. Figure 7.4(d)-(e) show additional lensing and melting of the crystals during the first run.

The second run of I-RDX sample 1 is shown in Fig. 7.4(f)-(g) where delamination and ‘boiling’ melt within the cavities moved rapidly outward to adjacent crystals, terminating at the boundary of the cluster. Figure 7.4(h) shows a Hirox microscope image after testing. Note that the dark fringes around the uppermost crystals in the ‘after’ image are no longer ‘lensing’ from a thermal gradient in the binder, but damage, possibly from decomposition products escaped along the weak vertical Sylgard casting interface. The dark mass within the binder cavities are former crystals which have melted and re-solidified after cooling, which happened during and after the insult was stopped.

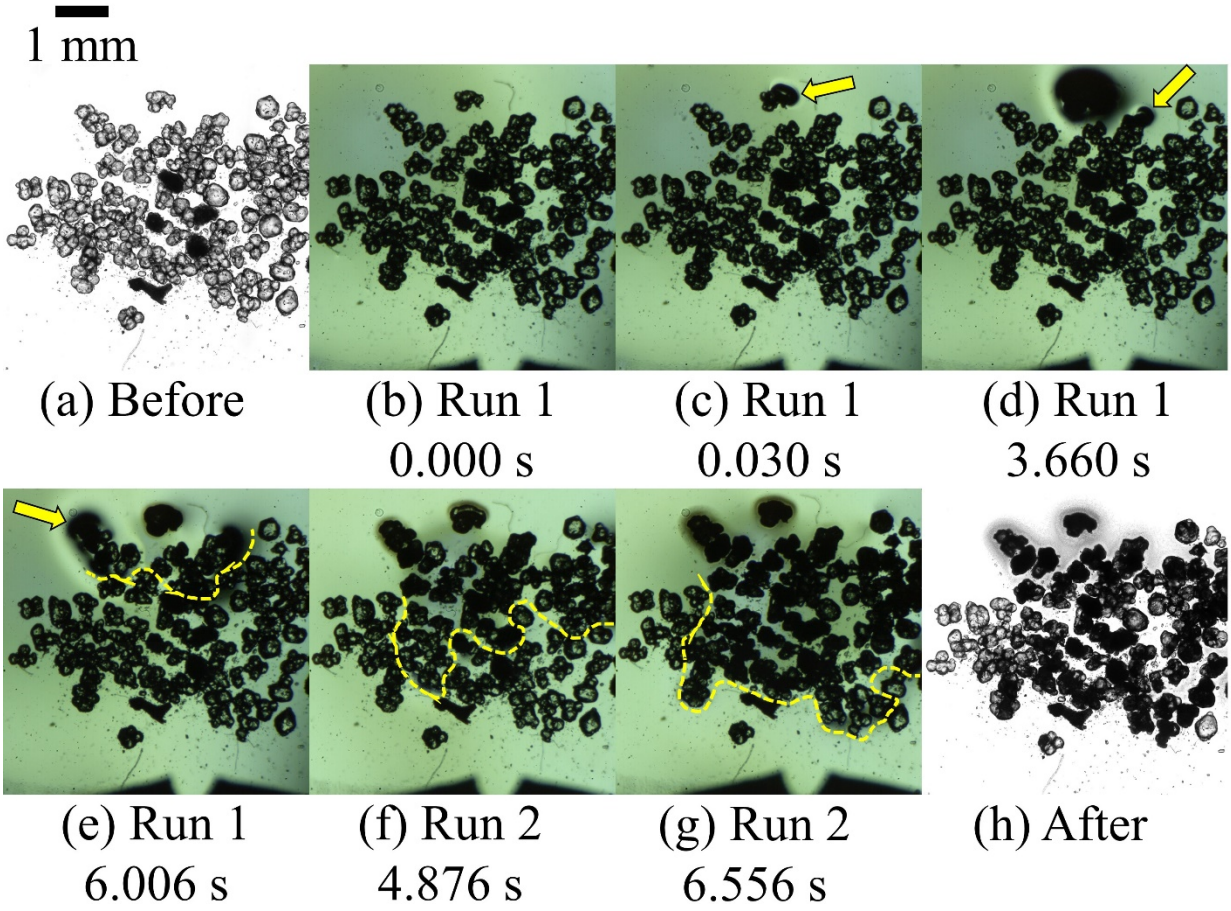


Figure 7.4. First and second runs of I-RDX sample 1 at 500 fps with backlighting. 'Before' and 'after' images were taken with a Hirox microscope.

I-RDX sample 2 is shown in Fig. 7.5. Figure 7.5(b)-(d) show delamination and melting propagate along adjacent crystals in run 1. These crystals melted and then re-solidified as opaque masses within the binder cavities. No motion was observed in run 2. During run 3, shown in Fig. 7.5(e)-(g), delamination and melting began at a different point within the cluster of crystals, away from the initial damage point, and propagated outward. Dark locations shown in the 'after' image in Fig. 7.5(h) identify the melted crystals. In this sample, damage occurred at two separate locations, independent of where crystals had previously been damaged.

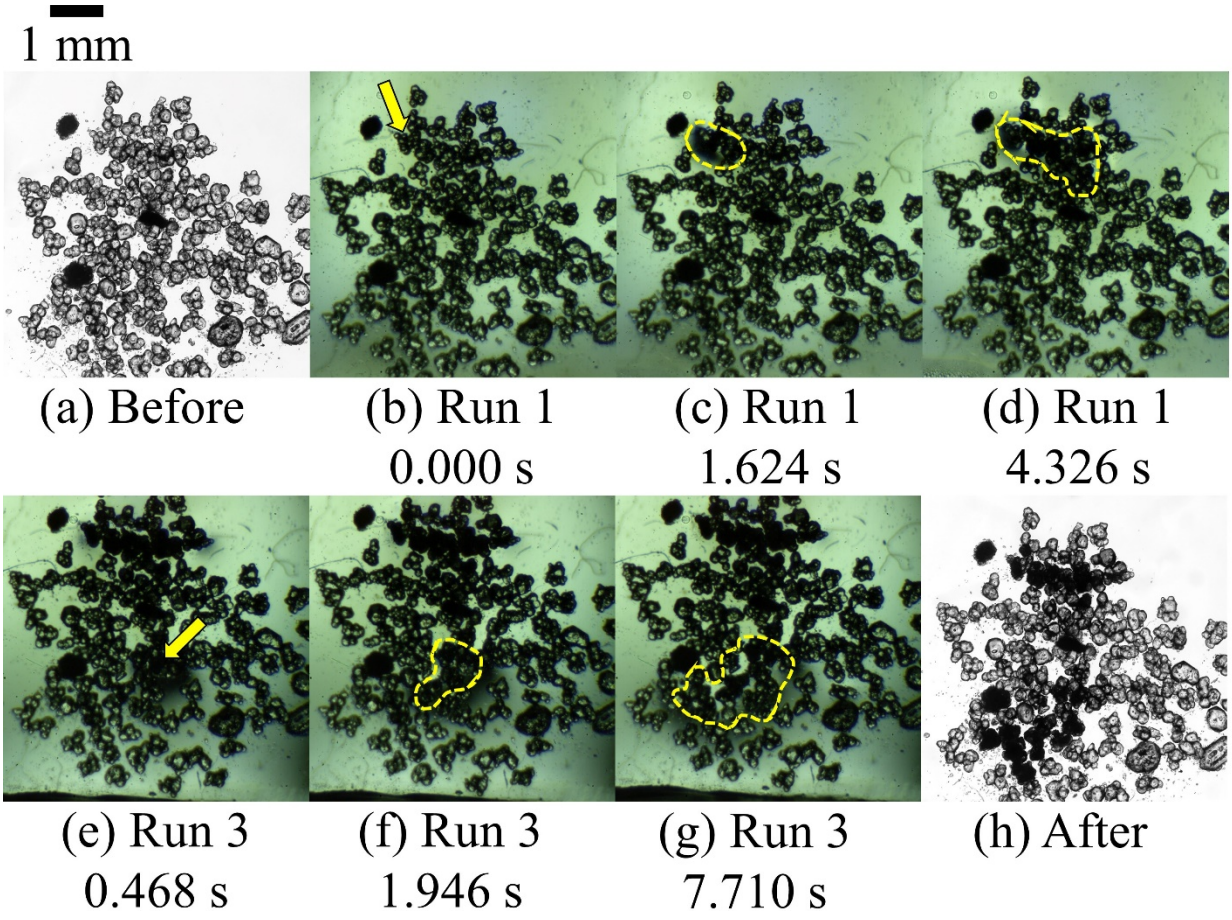


Figure 7.5. Runs 1 and 3 of I-RDX sample 2 at 500 fps with backlighting. 'Before' and 'after' images were taken with a Hirox microscope.

Figure 7.6 depicts 'production-grade' RDX sieved to above 500 μm particle size. The 500 μm production-grade RDX samples typically did not show much delamination or melting as did I-RDX. One case which did show melting and delamination is shown Fig. 7.6(b)-(c) where the first sign of melting began at a single crystal location in the interior of the cluster and then spread in all directions. The RDX melt within the binder cavities 'boiled' and then motion stopped as the melt re-solidified in an opaque mass within the cavity, dark from backlighting with no further motion. This was evidence that the temperature at those crystal locations fell below the melting point of RDX (205 °C), even as the excitation continued. The arrows in Fig. 7.6(d) show where delamination preceded melting and the binder was seen to peel across the crystal surfaces.

In Fig. 7.6(e)-(g), a second run of the same sample was performed after a cool-down period. The transducer interface with glue couplant can be seen, and crystals at the top of the

frame are cut off. This was typical of tests run for longer durations (10-15 s) before first motion was detected. Thermal expansion in the binder lifted the sample upwards where the surface was free. ‘Lensing’ can be observed around a crystal on the left of the cluster in Fig. 7.6(e), but the dark spot disappears as the thermal gradient within the binder at that point equilibrates due to reduced heat generation or as heat conducted away. The binder delamination, crystal melting, and re-solidification phenomenon propagated from the earlier point where run 1 had been terminated. In frame Fig.7.6(g), crystals nearest the transducer which had previously ‘boiled’ and re-solidified began to melt and boil again while expanding the binder cavity. This was indicative of the temperature again climbing above 205 °C as heat from the transducer conducted into the sample from below.

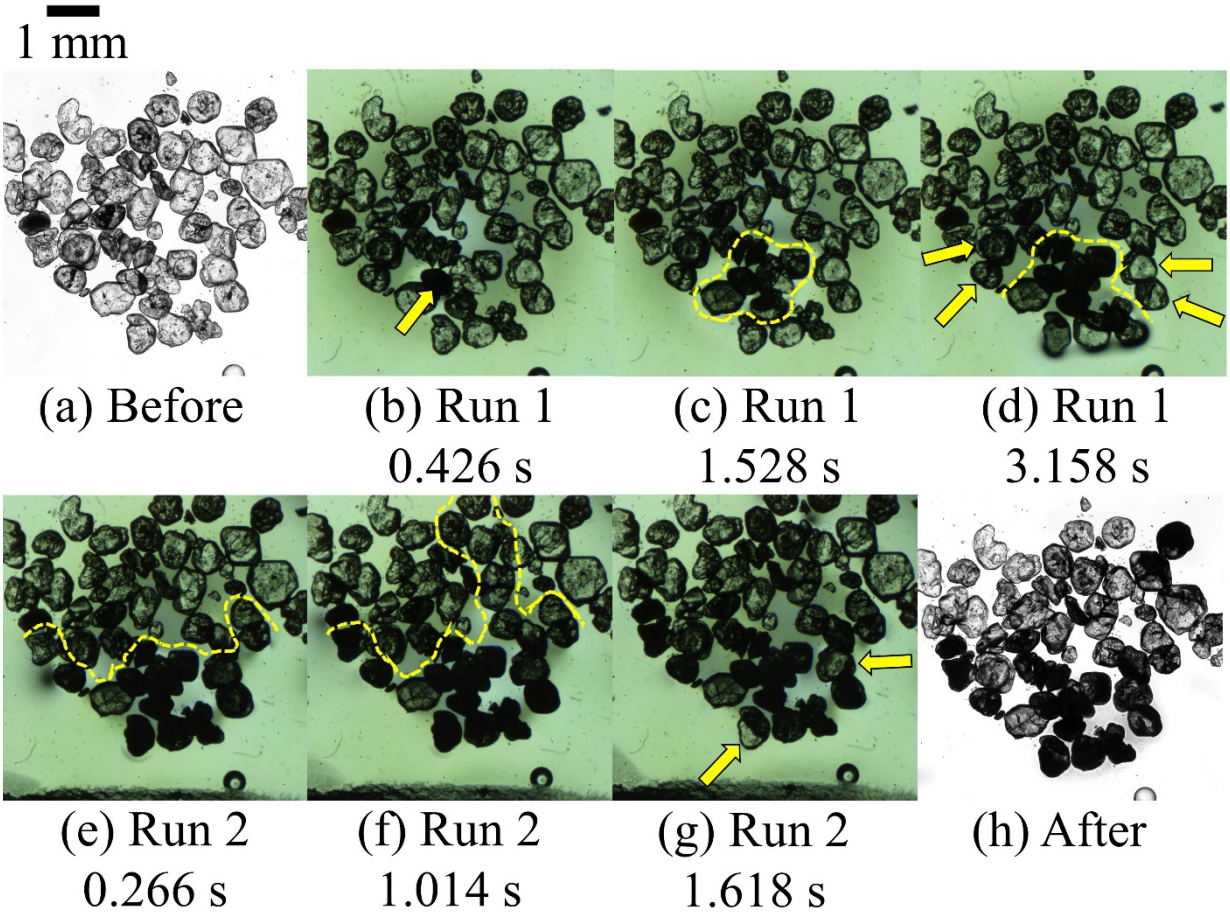


Figure 7.6. Two runs of 500 µm sieved RDX recorded at 500 fps with backlighting. ‘Before’ and ‘after’ images were taken with a Hirox microscope.

### 7.3.3 CL-20 Based PBXs

Figure 7.7 shows images from the only CL-20 agglomerate sample driven to reaction out of the four agglomerate samples tested. Out of the remaining three samples tested, two showed no signs of motion, and one showed brief ‘lensing’ near a central agglomerate. Figure 7.7(b)-(d) show a small, but intense temperature gradient on the bottom side of an agglomerate near the top, with many agglomerates interposed between it and the transducer face. Figure 7.7(e)-(g) show gas production spreading from this point into adjacent cavities. This happened very rapidly, occurring within 134 ms from initial detection of motion. The ‘after’ image in Fig. 7.7(h) shows that multiple agglomerates decomposed along with the initiation site, but quenched once the gases broke out of the top of the Sylgard block. Some agglomerates were only half consumed. An analysis of the growth of the ‘hot spot’ from 0.046 s to 0.114 s from the video of Fig. 7.7 is shown in Fig. 7.8. The small area of intense heating on the underside of a CL-20 agglomerate had an approximately spherical distinct outer-ring and inner dark area which was likely from the temperature/stress gradient early on, transitioning to a cavity of gaseous products.

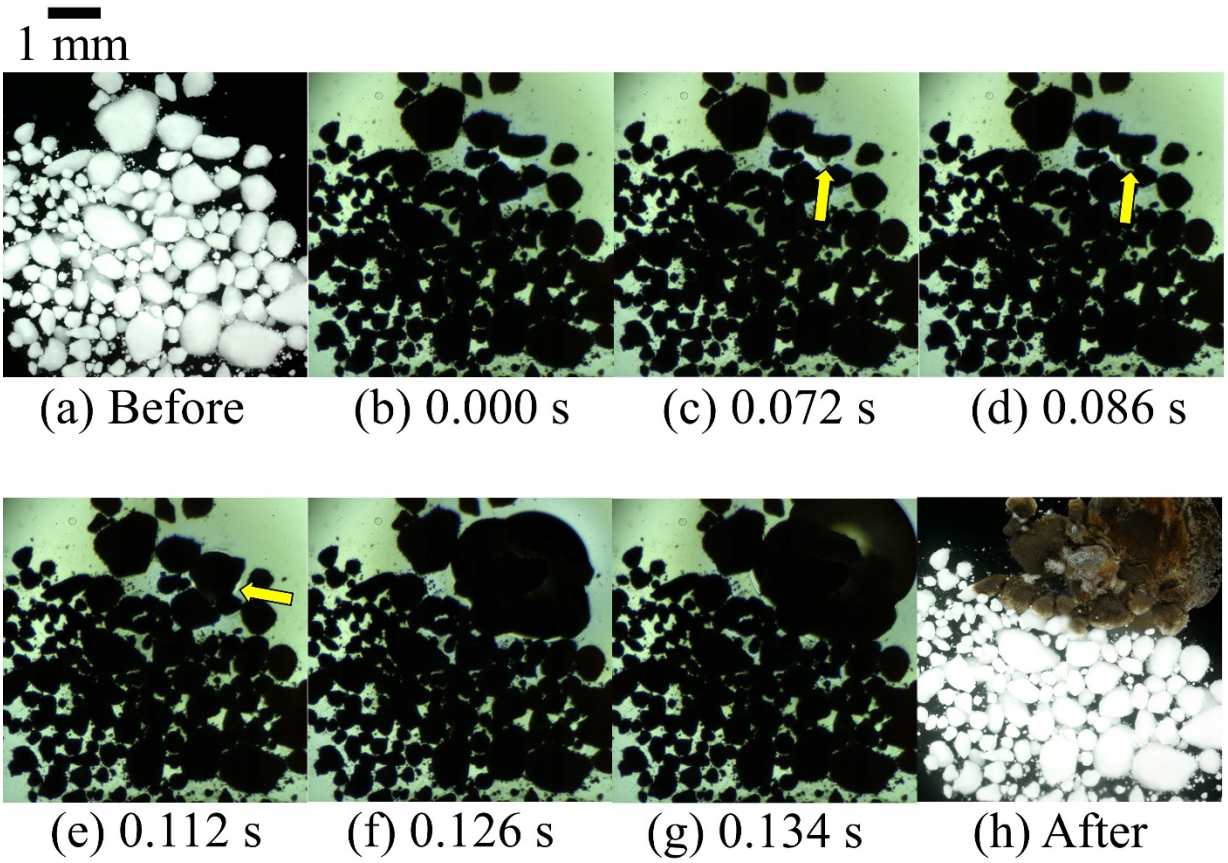


Figure 7.7. CL-20 agglomerates recorded at 500 fps with backlighting. ‘Before’ and ‘after’ images were taken with top ring-lighting on a Hirox microscope.

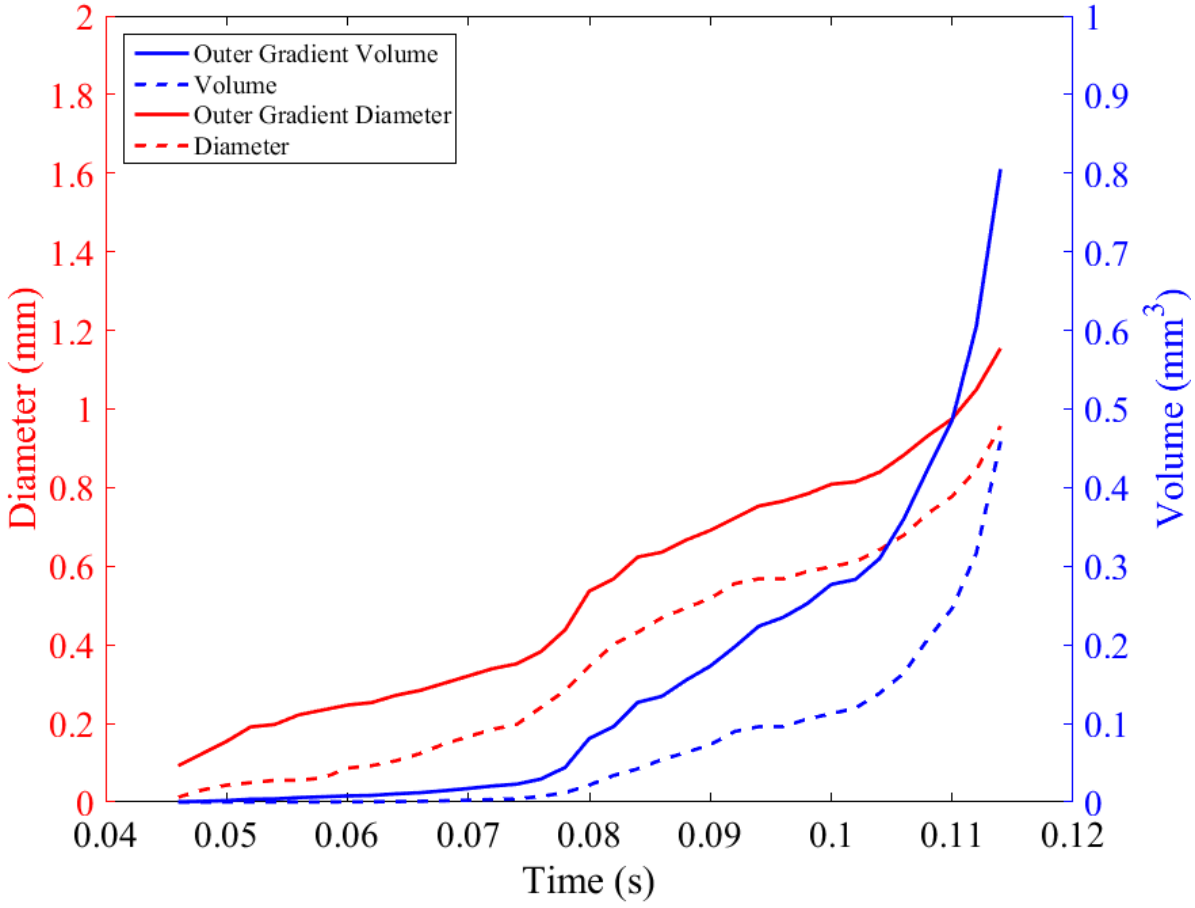


Figure 7.8. Analysis of the 'hot spot' size (outer-ring and inner dark area) and calculated spherical volume as observed from 34 video frames and most notably seen in Fig. 7.7(c)-(d).

Recrystallized CL-20 sample 1 is shown in Fig. 7.9. During the first run, motion was seen in the central most crystals indicated by the arrow in Fig. 7.9(b). Initial 'lensing' and blackening of crystals during the second run were observed with many crystals throughout the sample in Fig. 7.9(b)-(e). Interestingly, there was no 'boiling' or CL-20 melt motion before decomposition. Gas production in Fig. 7.9(f)-(k) pushed through adjacent binder cavities rapidly, taking only 144 ms. Figure 7.9(l) shows a Hirox microscope image with top ring-lighting showing the charred binder cavities after the decomposition products audibly expelled out of the top of the Sylgard block.

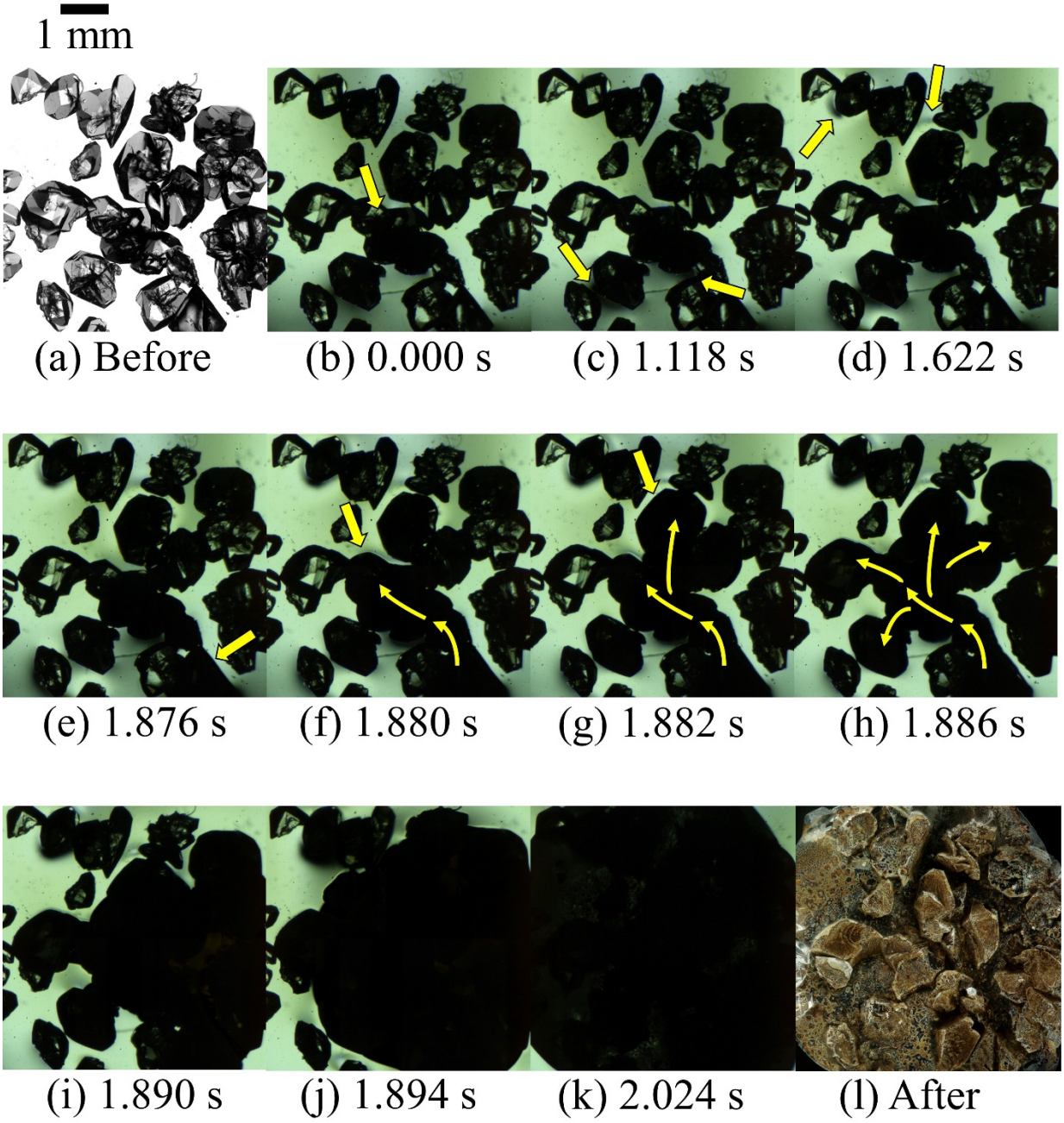


Figure 7.9. The second run of recrystallized CL-20 sample 1 recorded at 500 fps with backlighting. The 'Before' image was taken with backlighting and the 'after' image was taken with top ring-lighting on a Hirox microscope.

Recrystallized CL-20 sample 2 run 1 is shown in Fig. 7.10. As with sample 1, there was 'lensing' throughout the sample at different crystals with no identifiable 'boiling' or melt motion in Fig. 7.10(b)-(e). The first sign of decomposition began in Fig. 7.10(f) and rapidly expanded to

fill adjacent binder cavities along the weak casting layer in Fig. 7.10(f)-(k) before audibly breaking out of the top of the Sylgard block. A Hirox microscope image with top ring-lighting of the charred binder cavities is shown in Fig. 7.10(l). Two CL-20 crystals are seen to have survived.

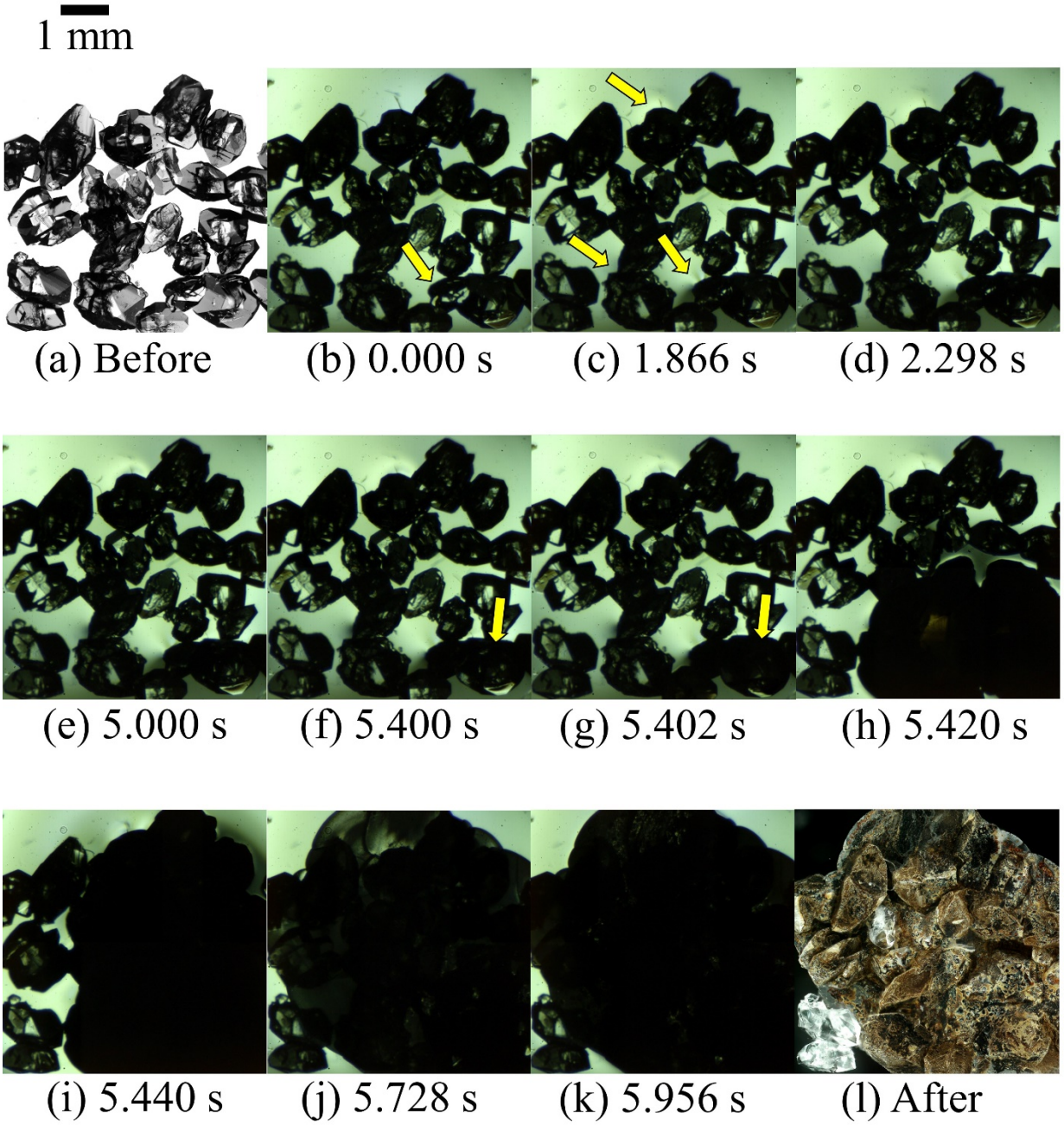


Figure 7.10. Recrystallized CL-20 sample 2 recorded at 500 fps with backlighting. The 'before' image was taken with backlighting and the 'after' image was taken with top ring-lighting on a Hirox microscope.

TNT/CL-20 cocrystals all exhibited very early melting during the tests due to the low melting point of TNT (80 °C). Typically, melt began simultaneously at many crystal locations near the bottom side, closest to the transducer, but lone crystals melting near the top and melting of adjacent crystals in a series were also observed. Four samples of TNT/CL-20 were tested resulting in all four melting, and three driven to decomposition. The TNT/CL-20 cocrystals in Fig. 7.11 began to melt at the lower locations identified in Fig. 7.11(b). Hot spots, visible due to 'lensing', developed at several other locations within the sample in Fig. 7.11(c)-(d). Frames Fig. 7.11(e)-(k) show rapid gas production from decomposition which pressurized the cavity and audibly broke out of the top of the binder. Soot vacated the cavity and the binder relaxed after the pressure reduced resulting in the lighter image in 7.11(k). A large amount of melted material, potentially TNT melt, moved into the broken vertical casting layer. This sample had similar behavior to pure CL-20 during reaction, but the color of the final products differed from those shown in Fig. 7.9(l) and Fig. 7.10(l).

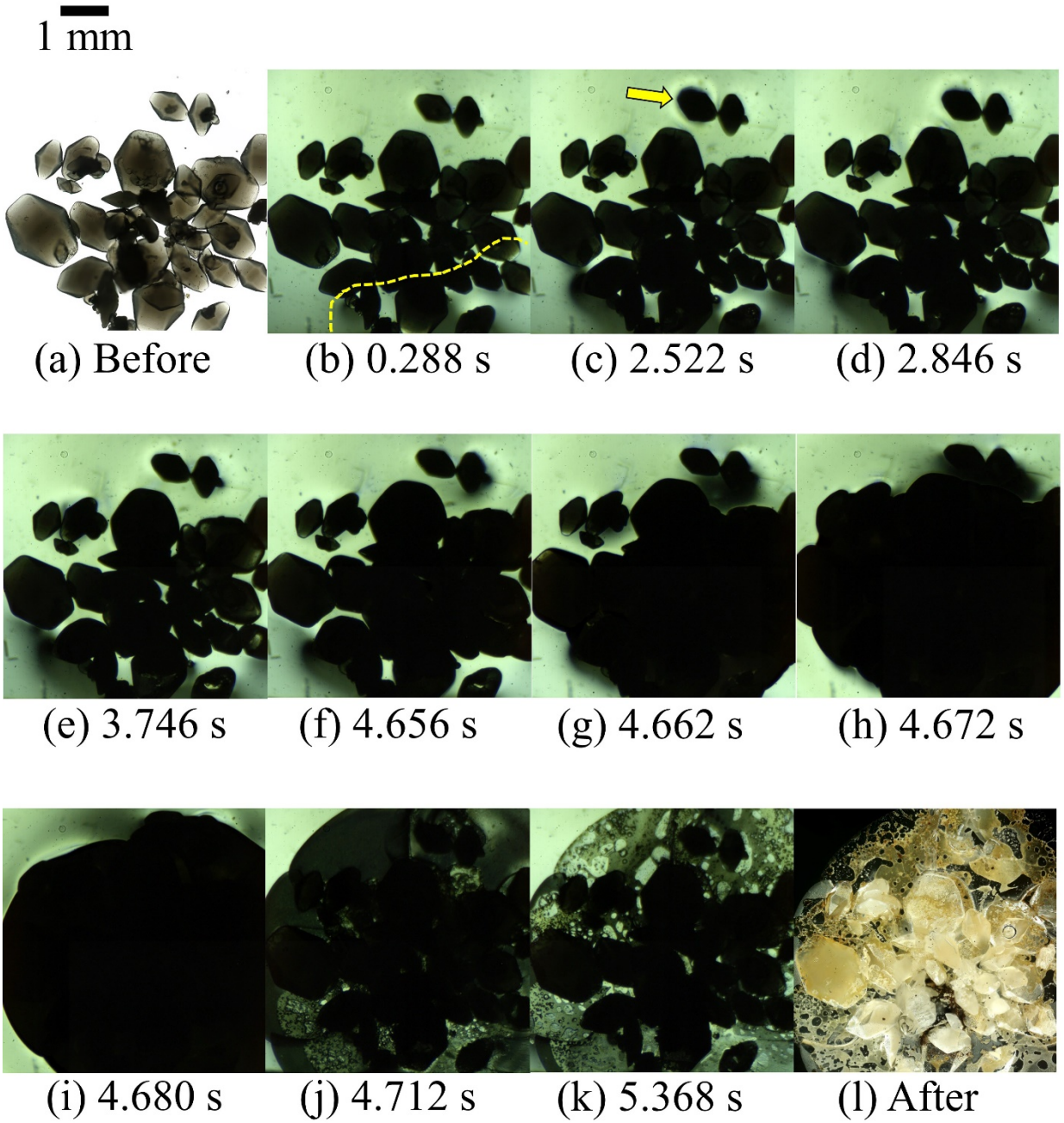


Figure 7.11. CL-20/TNT cocrystals recorded at 500 fps with backlighting. ‘Before’ image taken with backlighting and ‘after’ image taken with top ring-lighting on a Hirox microscope.

### 7.3.4 HMX

A grade B class 3 β-HMX sample is shown in Fig. 7.12. Unlike the single crystal HMX samples in Chapter 6, none of the high solids-loaded β or δ-HMX samples tested here underwent decomposition. More typical was a hot spot initiating near the top of the crystal cluster, as seen in Fig. 7.12(b), resulting in delamination followed by β-δ phase transition. Figure 7.12(c)-(g) show binder delamination and subsequent heating above 170 °C propagated outward until most of the crystals transitioned to δ-phase, as evidenced by the opaque crystals in Fig. 7.12(h).

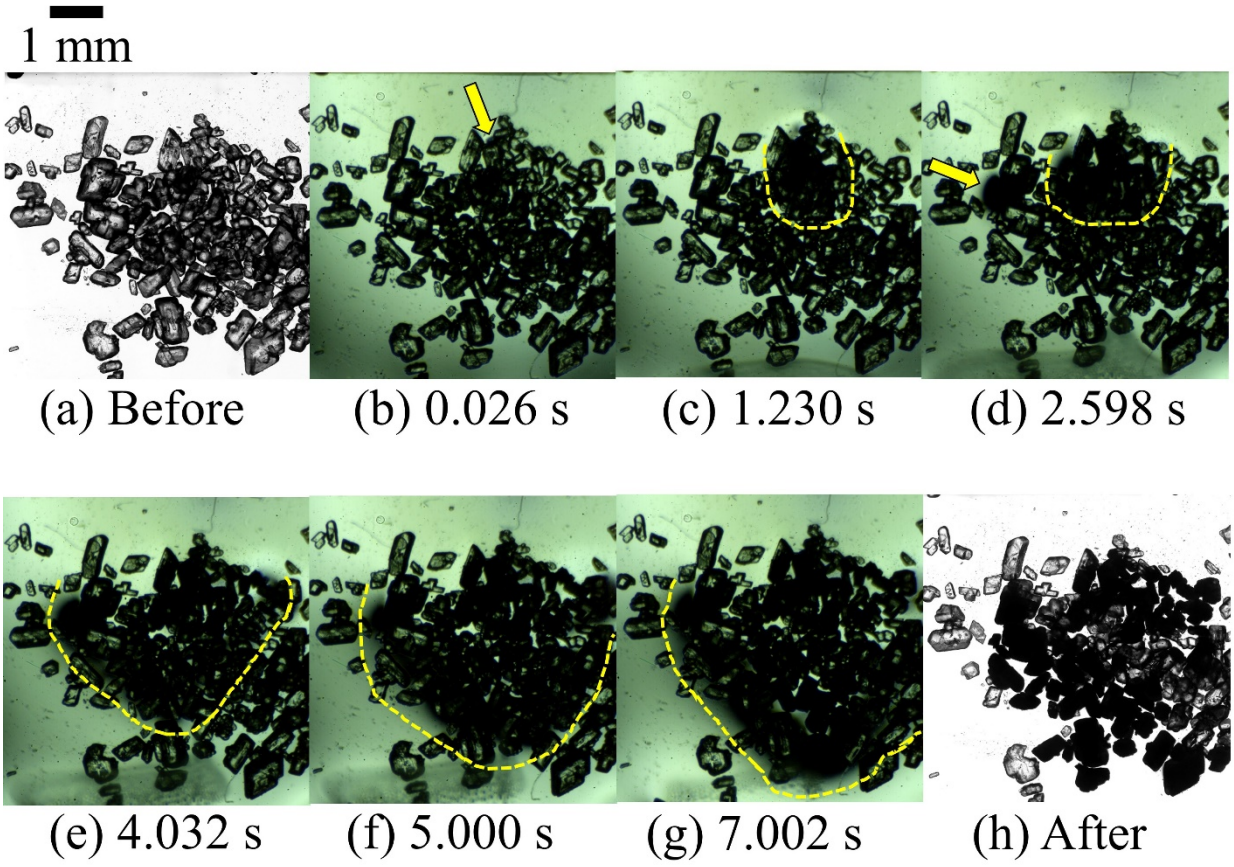


Figure 7.12. A grade B class 3 HMX sample recorded at 500 fps with backlighting. Backlight Hirox microscope images are shown as ‘before’ and ‘after’.

A δ-HMX sample is shown in Fig. 7.13. In Fig. 7.13(a) the first sign of motion appeared at a crystal interface far from the transducer face. In Fig. 7.13(b) more hot spots formed and were identified by ‘lensing’. The thermal images in Fig. 7.13(c)-(e) show the heat generated at the

crystal locations which conducted 1.70 mm to reach the front Sylgard surface. Heat conducted from the transducer interface can be seen at the bottom of Fig. 7.13(e). The maximum surface temperature reached was 64.9 °C and is shown in Fig. 7.14.

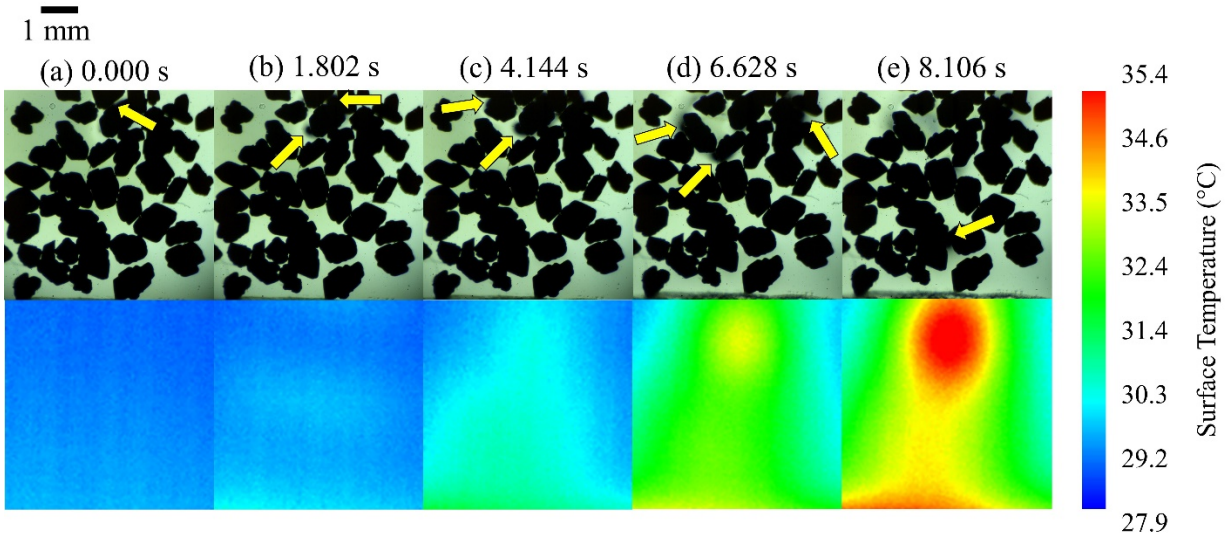


Figure 7.13. Simultaneous high-speed imaging and IR imaging of a δ-HMX sample with a fixed color scale.

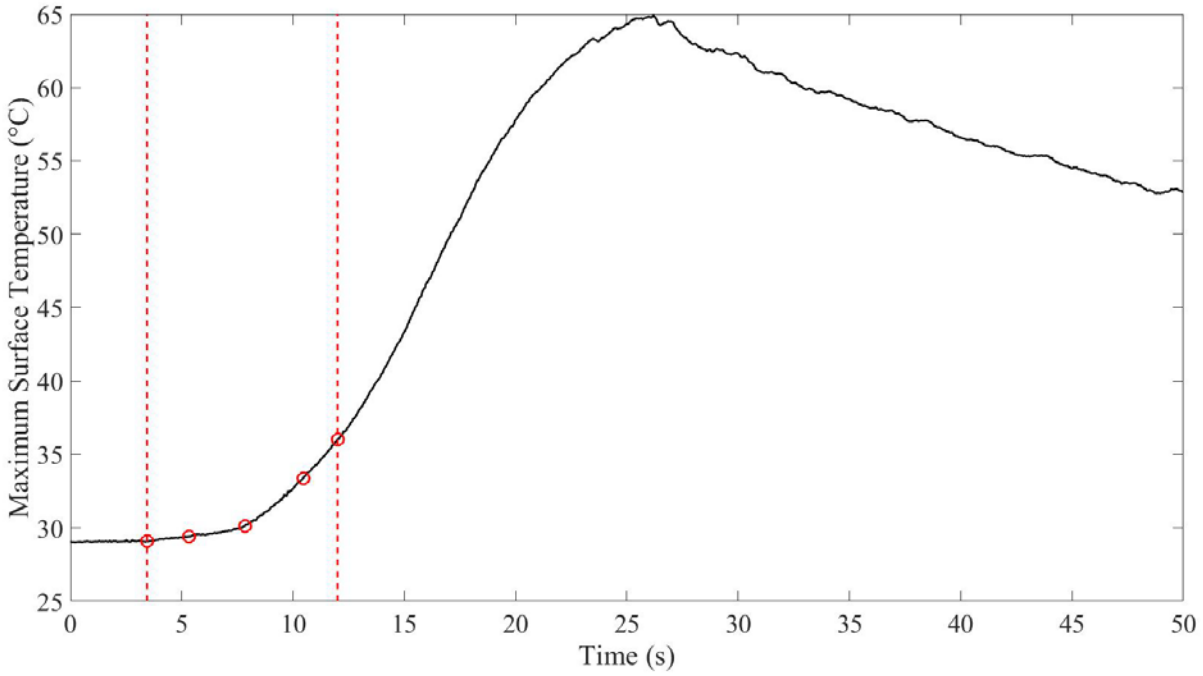


Figure 7.14. The accompanying maximum surface temperature plot for the δ-HMX sample from Fig. 7.12. The dashed red lines indicate the 8.106 s high-speed shadowgraphy recording interval which began at first motion with red circles indicating the selected frames. The transducer input was ended at about 20 s.

Recrystallized HMX is presented in Fig. 7.15. The first observations of 'lensing' along the bottom interface of the crystal on the right and at the interface of the two overlapping crystals on the left are shown in Fig. 7.15(b). In Fig. 7.15(c)-(d), delamination of the binder along the flat side of a crystal can be seen to propagate for approximately 3.5 s and a larger temperature gradient can be seen in the binder near the bottom. The second run began in Fig. 7.15(e) with two crystals already partially δ-phase, as evidenced by the opacity of the crystals against the backlighting. Note that in Fig. 7.15(e), of the crystals in the first run which had hot spots near them, only the crystals on the left underwent the β-δ solid-solid phase transition. Delamination can be seen again in Fig. 7.15(f)-(g) as well as 'lensing'. The 'after' image in Fig. 7.15(h) shows the damaged crystals, some of which underwent partial β-δ solid-solid phase transition during run 2 of testing.

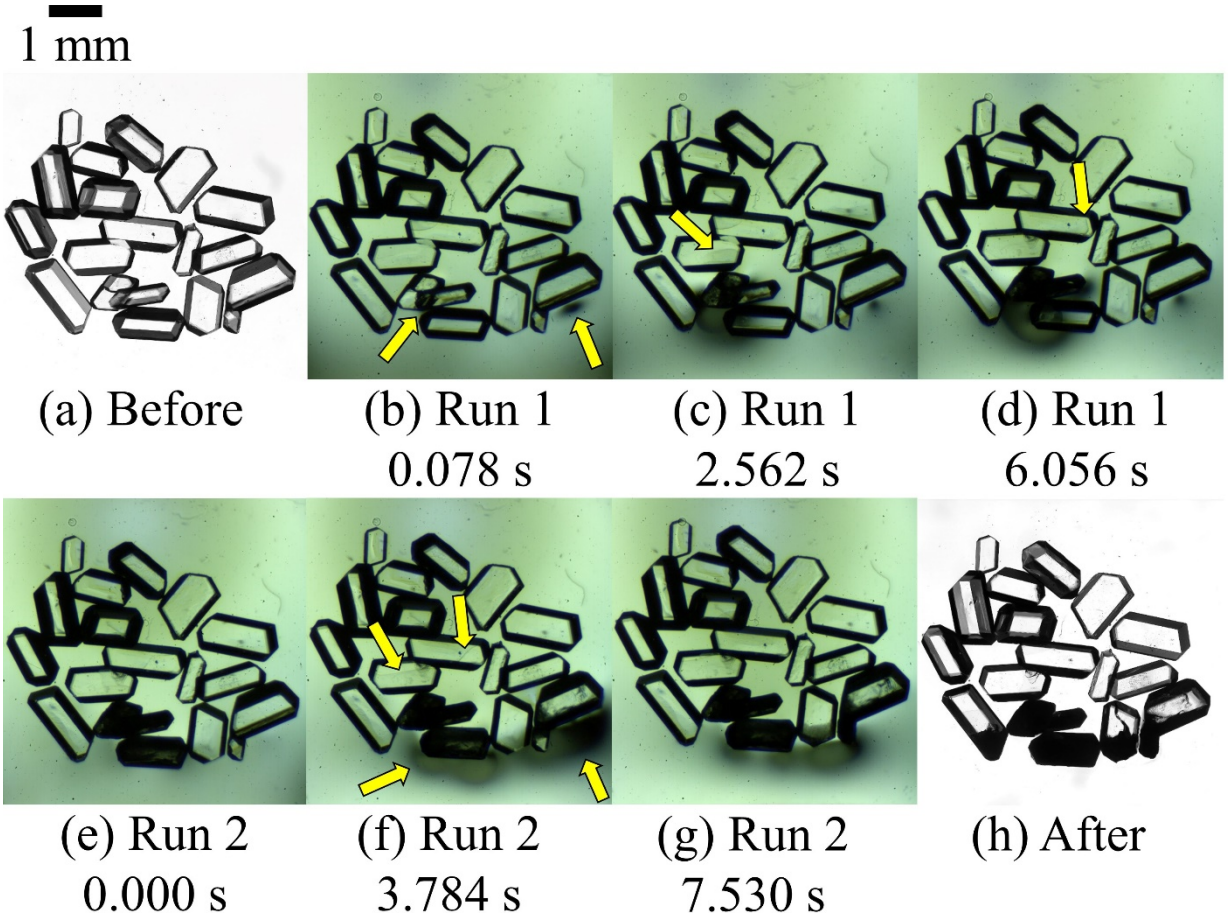


Figure 7.15. A sample of recrystallized HMX which underwent two runs of testing at 500 fps with backlighting. 'Before' and 'after' images were taken with a Hirox microscope.

## 7.4 Discussion

The mechanisms of heating in ultrasonically insulted PBXs were explored by observing the behavior and interaction of systems of multiple energetic crystals with different melting and decomposition temperatures/rates. The first observations of 'lensing' show where initial hot spots exist. Thermal expansion of the transparent binder refracts light due to changing density and thus, index of refraction. Light refracts away from the normal in less dense areas, creating a darker image. I-RDX sample 1, the recrystallized-HMX, and the CL-20 agglomerate samples most clearly show the 'lensing' phenomena, especially at small spatial locations identified as hot spots.

Despite interposing crystals, hot spots manifested at locations far from the transducer interface. Hot spots also appeared in the binder on the near sides of crystals, oriented closest to

the transducer, but never appeared in the binder away from the influence of an inclusion. Darkened areas of binder near crystals were not only visible in the initial seconds of testing when the spatial temperature gradients were highest, but continued to be visible due to continuing heat generation which maintained the temperature gradient. Some hot spots, such as those in the recrystallized-HMX sample, developed without inducing any visible binder delamination in the nearest crystal. This accounts for the ignition of the single-crystal recrystallized HMX sample in Chapter 6 Fig. 6.6, where the primary heat generation mechanism was explained by viscoelastic heating in the binder from the high frequency excitation, rather than frictional heating from a moving, delaminated crystal/binder interface.

Acoustic energy propagated crystal/binder delamination through adjacent crystals, and once gas was produced, the decomposition gas products followed the opened pathway. A binder with stronger adhesion than Sylgard 184 would mitigate further damage in this manner, although once crystals such as RDX melt, or HMX transitions to δ-phase, the binder would also be delaminated. This observation parallels that seen in the low velocity impact sample showcased in Parab *et al.* [65], in which crystal cracking followed a ‘stress train’ of large particles. The failure paths in PBX 9501 have also been observed to follow large crystal detachment from the fine grained material during compression [24].

The RDX sample presented here had the most visible events out of the four RDX samples tested and appeared to melt and re-solidify within the binder pocket, becoming opaque against backlighting. Melting and decomposition are coupled in RDX, although at the heating rates and temperatures inferred here, cavity expansion denoting decomposition in RDX did not appear to take place. Large, spherical RDX appears to be a good candidate for vibration-insensitive formulations, similar in morphology to the spherical recrystallized HMX which experienced very few events in Chapter 6 [see Fig.6.1(e)]. The melting point of RDX is also higher than the δ-phase transition temperature of HMX, making RDX less likely to be permanently damaged during insult.

Eurenco ‘insensitive’ I-RDX is marketed as less sensitive to shock in cast configurations, but consistently appeared to be more sensitive to being damaged (delaminating and melting) from vibrational insult than the 500 μm sieved production-grade RDX. Thus, under insult conditions tested here, I-RDX was more ‘sensitive’ which can primarily be attributed to morphological differences between the two crystal types, as the I-RDX had more features where

stresses from thermal expansion and the acoustic field could initiate delamination [18]. Once delaminated, heating increased rapidly and melted more I-RDX crystals than was seen in any production-grade RDX sample.

The low melting point of PETN caused observable melt early into the agglomerate tests. Re-solidification of melt captured within the binder pockets permitted cycling several times. Some tests concluded with the melt remaining in a liquid phase trapped within the cavities until heat had dissipated out of the sample for several seconds. The agglomerates appear to be porous because the melt occupied entire individual cavities and melt was seen to bubble and 'boil' within. The melting temperature of PETN is distinct from the onset of decomposition, and this property was initially thought to be beneficial in a vibration-insensitive PBX where frictional heating would be reduced at the binder interfaces once melting occurred [9], but in fact this property did not prevent heating to decomposition. Decomposition occurred in three PETN agglomerate samples out of six total and was easily identifiable by the expansion of the cavities (pressurization) and breakout into the weak vertical casting layer. Decomposition never happened on the first run, but only after melt had re-solidified from a previous run. Both tested crystalline PETN samples similarly melted and flowed into connected cavities, one which was cycled three times, and the one showcased here in which gas products broke into the casting plane on the first run.

Melting temperature was not the only determining factor for initiation, shown by comparison of CL-20 versus HMX and RDX, which had drastically different responses despite CL-20 having a melting point between that of HMX and RDX. Both crystalline CL-20 samples tested rapidly decomposed, one on the first run, and one on the second run. One of the four CL-20 agglomerate samples tested underwent a similar decomposition, matching that of crystalline CL-20. This suggests that the thermal initiation sensitivity of polymer-bonded CL-20 subjected to acoustic insult is attributable to chemical differences and not morphological. TNT/CL-20 cocrystals exhibited the expected properties of both constituents. Three of the four TNT/CL-20 cocrystal samples tested had rapid melting early into tests and decomposed violently like both other types of CL-20.

On subsequent runs, events could take place at different locations and not necessarily where damage had already occurred. I-RDX sample 2 shows one example where new pathways were opened rather than the continued reinforcement of heating at previously damaged

crystal/binder interfaces. Damage (debonding and melt) could also be propagated into adjacent crystals as in I-RDX sample 1, the RDX sample, and the grade B class 3 HMX sample which were all observed to be damaged continuously and at the same point on subsequent runs.

Hot spots were observed in δ-HMX, but samples of this type did not show the same sensitivity to initiate as did previous testing on single crystals. The single δ-HMX crystal samples in Chapter 6 were the most reactive, sometimes with up to three gas production events. Strikingly, none of the high solids-loaded δ-HMX samples presented here were driven to decomposition. In this system, a focused acoustic energy appears to be necessary to initiate HMX (as in Chapter 3, Chapter 5 and Chapter 6) [15, 66, 67] but energy was dissipated simultaneously at too many locations in the vertical high solids-loaded samples to reach high enough temperatures for initiation.

## 7.5 Conclusions

Hot spots were observed in simplified PBX systems via the non-intrusive imaging technique of shadowgraphy. The explosives PETN (crystalline and agglomerated), RDX, I-RDX, CL-20 (crystalline and agglomerated), TNT/CL-20 cocrystals, HMX, and δ-HMX within a transparent binder were damaged or driven to thermal decomposition to varying degrees by contact ultrasonic excitations. Constructive interference of acoustic waves occurred within the sample where an opaque binder or higher solids-loading would normally inhibit the detection of internal crystal/binder damage. This highlights the need for vibration insensitive munitions, because the damage might go undetected, resulting in accidental initiation or degradation in performance.

Recommendations of binder and energetic crystal properties to mitigate heating at high frequencies (100-1000 kHz) are made based on these findings. Specifically, frictional heating from a delaminated and moving binder interface against an energetic crystal and friction from crystal/crystal contact points are a major source of heat generation. Delamination can occur due to viscoelastic heat dissipation at stress concentrations from acoustic interaction in the binder at the crystal interface and the accompanying thermal expansion. This particular heating mechanism is not specifically identified by Field [2] in the ten proposed hot spot ignition mechanisms, although it is related to: (ii) other mechanisms involving cavity collapse, such as viscous or plastic heating of the surrounding matrix material and (v) viscous heating of material

rapidly extruded between impacting surfaces. Once a crystal was delaminated, pathways opened through adjacent crystals where delamination propagated and gas products escaped. Thus, the adhesion and thermal expansion behavior of the binder are important properties in formulation design. Additionally, surface asperities on a crystal are the nucleation points of binder delamination and smoother crystals were much less likely to be driven to decomposition. These observations highlight the similarities between the single crystal simplified PBX samples and higher solids-loaded samples, closer to real-world PBXs.

Higher melting point energetic crystals are desirable to be used in a vibration-insensitive PBX since, although friction reduces once melting occurs at the interface, acoustic energy was still seen to drive the explosives to chemical decomposition and frictional heating from delamination occurs at earlier stages. Large, smooth RDX crystals performed well in these high-frequency (210.5 kHz) ultrasonic experiments, followed closely by HMX, while CL-20 and PETN performed poorly.

Future work should focus on characterizing the insult produced by the STEM Inc. SMD10T2R111 transducer for possible standardization or replication in small scale vibration sensitivity testing. Different transducers should be explored which have a flat response over a range of frequencies to facilitate testing the influence of frequency on the initiation/damage response of simplified PBX samples, perhaps matching the wavelength to the crystal diameters. This knowledge will also help when exploring the effects of different power levels. Performing standardized small scale sensitivity tests (dropweight) on similar types of samples and on ultrasonically damaged samples will help to show if any links exist between the ignition mechanisms present. Additionally, other binders with different properties should be examined to confirm the recommendations formed herein.

## 7.6 Acknowledgements

Thanks to V. S. Vuppuluri for supplying the recrystallized CL-20 and TNT/CL-20 cocrystals and C. J. Sorensen for the recrystallized HMX and PETN.

# REFERENCES


[1] Y.-Q. Wu, and F.-L. Huang, “Experimental investigations on a layer of HMX explosive crystals in response to drop-weight impact,” *Combust. Sci. Technol.*, vol. 185, no. 2, pp. 269–292, 2013.

[2] J. E. Field, “Hot spot ignition mechanisms for explosives,” *Acc. Chem. Res.*, vol. 25, no. 11, pp. 489–496, 1992.

[3] F. P. Bowden, and A. D. Yoffe, *Initiation and growth of explosion in liquids and solids*. Cambridge: Cambridge University Press, 1952.

[4] F. P. Bowden, and A. D. Yoffee, *Fast reactions in solids*. London: Butterworths Scientific Publications, 1958.

[5] C. M. Tarver, S. K. Chidester, and A. L. Nichols, “Critical conditions for impact- and shock-induced hot spots in solid explosives,” *J. Phys. Chem.*, vol. 100, no. 14, pp. 5794–5799, 1996.

[6] F. P. Bowden, and K. Singh, “Size effects in the initiation and growth of explosion,” *Nature*, vol. 172, pp. 378–380, 1953.

[7] J. E. Field, N. K. Bourne, S. J. P. Palmer, and S. M. Walley, “Hot-spot ignition mechanisms for explosives and propellants [and discussion],” *Philos. Trans. R. Soc. A Math. Phys. Eng. Sci.*, vol. 339, no. 1654, pp. 269–283, 1992.

[8] F. P. Bowden, and A. Yoffee, “Hot spots and the initiation of explosion,” in *Third Symposium on combustion, flame and explosion phenomena*, 1948, pp. 551–560.

[9] F. P. Bowden, and O. A. Gurton, “Initiation of explosions by grit particles,” *Nature*, vol. 162, pp. 654–655, 1948.

[10] N. P. Loginov, “Vibration sensitivity of solid explosives,” *Combust. Explos. Shock Waves*, vol. 31, no. 1, pp. 94–99, 1995.

[11] B. W. Asay, P. M. Dickson, B. F. Henson, L. G. Hill, S. I. Jackson, J. E. Kennedy, J. M. McAfee, G. R. Parker, W. L. Perry, P. J. Rae, and L. B. Smilowitz, *Shock wave science and technology reference library, Vol. 5: Non-shock initiation of explosives*. Heidelberg: Springer-Verlag, 2010.

[12] F. P. Bowden, and O. A. Gurton, “Birth and growth of explosion in liquids and solids

initiated by impact and friction," *Proc. R. Soc. A Math. Phys. Sci.*, vol. 198, pp. 350–372, 1949.

[13] S. M. Walley, J. E. Field, R. A. Biers, W. G. Proud, D. M. Williamson, and A. P. Jardine, "The use of glass anvils in drop-weight studies of energetic materials," *Propellants, Explos. Pyrotech.*, vol. 40, no. 3, pp. 351–365, 2015.

[14] J. E. Field, N. K. Bourne, S. J. P. Palmer, S. M. Walley, J. Sharma, and B. C. Beard, "Hot-spot ignition mechanisms for explosives and propellants [and discussion]," *Philos. Trans. R. Soc. London A Math. Phys. Eng. Sci.*, vol. 339, no. 1654, pp. 269–283, May 1992.

[15] Z. A. Roberts, J. O. Mares, J. K. Miller, I. E. Gunduz, S. F. Son, and J. F. Rhoads, "Phase changes in embedded HMX in response to periodic mechanical excitation," in *Challenges in Mechanics of Time Dependent Materials, Volume 2: Proceedings of the 2016 Annual Conference on Experimental and Applied Mechanics*, B. Antoun, A. Arzoumanidis, J. H. Qi, M. Silberstein, A. Amirkhizi, J. Furmanski, and H. Lu, Eds. Cham: Springer International Publishing, 2016, pp. 79–86.

[16] J. O. Mares, J. K. Miller, I. E. Gunduz, J. F. Rhoads, and S. F. Son, "Heat generation in an elastic binder system with embedded discrete energetic particles due to high-frequency, periodic mechanical excitation," *J. Appl. Phys.*, vol. 116, no. 20, p. 204902, 2014.

[17] N. P. Loginov, "Structural and physicochemical changes in RDX under vibration," *Combust. Explos. Shock Waves*, vol. 33, no. 5, pp. 598–604, 1997.

[18] J. O. Mares, D. C. Woods, C. E. Baker, S. F. Son, J. F. Rhoads, J. S. Bolton, and M. Gonzalez, "Localized heating near a rigid spherical inclusion in a viscoelastic binder material under compressional plane wave excitation," *J. Appl. Mech.*, vol. 84, no. 4, p. 041001, 2017.

[19] Z. A. Roberts, A. D. Casey, I. E. Gunduz, J. F. Rhoads, and S. F. Son, "The effects of crystal proximity and crystal-binder adhesion on the thermal responses of ultrasonically-excited composite energetic materials," *J. Appl. Phys.*, vol. 122, no. 24, p. 244901, 2017.

[20] A. E. D. M. Van Der Heijden, and R. H. B. Bouma, "Crystallization and characterization of RDX, HMX, and CL-20," *Cryst. Growth Des.*, vol. 4, no. 5, pp. 999–1007, 2004.

[21] L. Smilowitz, B. F. Henson, M. Greenfield, A. Sas, B. W. Asay, and P. M. Dickson, "On the nucleation mechanism of the β-δ phase transition in the energetic nitramine octahydro-1,3,5,7-tetranitro-1,3,5,7-tetrazocine," *J. Chem. Phys.*, vol. 121, no. 11, pp. 5550–5552, 2004.

[22] M. A. Daniel, "Polyurethane binder systems for polymer bonded explosives," *DSTO-GD-*

*0492*. Defence Science and Technology Organisation, 2006.

[23] B. L. Hamshere, I. J. Lochert, and R. M. Dexter, “Evaluation of PBXN-109: the explosive fill for the penguin anti-ship missile warhead,” *DSTO-TR-1471*. Defence Science and Technology Organization, 2003.

[24] P. J. Rae, S. J. P. Palmer, H. T. Goldrein, J. E. Field, and A. L. Lewis, “Quasi-static studies of the deformation and failure of PBX 9501,” *Proc. R. Soc. A Math. Phys. Eng. Sci.*, vol. 458, no. 2025, pp. 2227–2242, 2002.

[25] J. O. Mares, J. K. Miller, N. D. Sharp, D. S. Moore, D. E. Adams, L. J. Groven, J. F. Rhoads, and S. F. Son, “Thermal and mechanical response of PBX 9501 under contact excitation,” *J. Appl. Phys.*, vol. 113, no. 8, p. 084904, 2013.

[26] J. K. Miller, J. O. Mares, I. E. Gunduz, S. F. Son, and J. F. Rhoads, “The impact of crystal morphology on the thermal responses of ultrasonically-excited energetic materials,” *J. Appl. Phys.*, vol. 119, no. 2, p. 024903, 2016.

[27] M. Chen, S. You, K. S. Suslick, and D. D. Dlott, “Hot spots in energetic materials generated by infrared and ultrasound, detected by thermal imaging microscopy,” *Rev. Sci. Instrum.*, vol. 85, no. 2, p. 023705, 2014.

[28] S. You, M. Chen, D. D. Dlott, and K. S. Suslick, “Ultrasonic hammer produces hot spots in solids,” *Nat. Commun.*, vol. 6, p. 6581, 2015.

[29] Z. Men, K. S. Suslick, and D. D. Dlott, “Thermal explosions of polymer-bonded explosives with high time and space resolution,” *J. Phys. Chem. C*, vol. 122, no. 26, pp. 14289–14295, 2018.

[30] D. C. Woods, J. K. Miller, and J. F. Rhoads, “On the thermomechanical response of HTPB-based composite beams under near-resonant excitation,” *J. Vib. Acoust.*, vol. 137, no. 5, p. 054502, 2015.

[31] J. K. Miller, D. C. Woods, and J. F. Rhoads, “Thermal and mechanical response of particulate composite plates under inertial excitation inertial excitation,” *J. Appl. Phys.*, vol. 116, no. 24, p. 244904, 2014.

[32] D. C. Woods, J. K. Miller, and J. F. Rhoads, “On the thermomechanical response of HTPB composite beams under near-resonant base excitation,” in *Proceedings of the ASME 2014 International Design Engineering Technical Conferences & Computers and Information in Engineering Conference*, 2014, p. 34516.

[33] J. Paripovic, and P. Davies, “Characterizing the dynamics of systems incorporating

surrogate energetic materials," in *Special Topics in Structural Dynamics: Conference Proceedings of the Society for Experimental Mechanics Series*, vol. 6, 2016, pp. 101–109.

[34] A. R. Range, N. R. Mcmindes, J. B. Tucker, and J. F. Rhoads, "The influence of formulation variation and thermal boundary conditions on the near-resonant thermomechanics of mock explosives," in *Fracture, Fatigue, Failure and Damage Evolution, Volume 7, Conference Proceedings of the Society for Experimental Mechanics Series*, 2018, pp. 47–55.

[35] P. W. Cooper, *Explosives Engineering*. New York: Wiley-VCH, 1996.

[36] T. R. Gibbs, and A. Popolato, Eds., *LASL Explosive Property Data*. Berkeley: University of California Press, 1980.

[37] A. Elbeih, M. Mohamed, and T. Wafy, "Sensitivity and detonation characteristics of selected nitramines bonded by Sylgard binder," *Propellants, Explos. Pyrotech.*, vol. 41, pp. 1044–1049, 2016.

[38] M. Suceska, *Test methods for explosives*. New York: Springer-Verlag, 1995.

[39] N. P. Loginov, "Criteria for estimation of explosion hazard in producing and processing explosives under vibration," *Combust. Explos. Shock Waves*, vol. 36, no. 5, pp. 633–638, 2000.

[40] V. W. Manner, J. D. Yeager, B. M. Patterson, D. J. Walters, J. A. Stull, N. L. Cordes, D. J. Luscher, K. C. Henderson, A. M. Schmalzer, and B. C. Tappan, "In situ imaging during compression of plastic bonded explosives for damage modeling," *Materials*, vol. 10, no. 6, p. 638, 2017.

[41] M. M. Sandstrom, G. W. Brown, D. N. Preston, C. J. Pollard, K. F. Warner, D. N. Sorensen, D. L. Remmers, J. J. Phillips, T. J. Shelley, J. A. Reyes, P. C. Hsu, and J. G. Reynolds, "Variation of methods in small-scale safety and thermal testing of improvised explosives," *Propellants, Explos. Pyrotech.*, vol. 40, no. 1, pp. 109–126, 2015.

[42] Z. Men, W. P. Bassett, K. S. Suslick, and D. D. Dlott, "Drop hammer with high-speed thermal imaging," *Rev. Sci. Instrum.*, vol. 89, no. 11, p. 115104, 2018.

[43] L. E. Kinsler, A. R. Frey, A. B. Coppens, and J. V. Sanders, *Fundamentals of acoustics*, 4th ed. New York: Wiley, 1999.

[44] C. R. Heitkamp, J. K. Miller, A. Loehr, J. S. Bolton, and J. F. Rhoads, "Experimental measurements of binder wave speeds using wavenumber decomposition," *Publ. Ray W. Herrick Lab.*, p. 105, 2017.

[45] C. R. Heitkamp, “Experimental wave and material property measurements for an elastomer binder and particulate composite,” Purdue University, 2018.

[46] P. M. Dickson, G. R. Parker, L. B. Smilowitz, J. M. Zucker, and B. W. Asay, “Frictional heating and ignition of energetic materials,” *AIP Conf. Proc.*, vol. 845, no. 1, pp. 1057–1060, 2006.

[47] W. L. Perry, J. A. Gunderson, M. M. Balkey, and P. M. Dickson, “Impact-induced friction ignition of an explosive : Infrared observations and modeling,” *J. Appl. Phys.*, vol. 108, no. 8, p. 084902, 2010.

[48] C. K. Saw, “Kinetics of HMX and phase transitions : effects of grain size at elevated tempearture,” in *12th International Detonation Symposium*, 2002, pp. 70–76.

[49] B. F. Henson, B. W. Asay, R. K. Sander, S. F. Son, J. M. Robinson, and P. M. Dickson, “Dynamic measurement of the HMX β- δ phase transition by second harmonic generation,” *Phys. Rev. Lett.*, vol. 82, no. 6, pp. 1213–1216, 1999.

[50] L. Smilowitz, B. F. Henson, B. W. Asay, and P. M. Dickson, “The β-δ phase transition in the energetic nitramine-octahydro-1,3,5,7-tetranitro-1,3,5,7-tetrazocine: Kinetics,” *J. Chem. Phys.*, vol. 117, no. 8, pp. 3789–3798, 2002.

[51] F. Simon, S. Clevers, V. Dupray, and G. Coquerel, “Relevance of the second harmonic generation to characterize crystalline samples,” *Chem. Eng. Technol.*, vol. 38, no. 6, pp. 971–983, 2015.

[52] H. Czerski, W. L. Perry, and P. M. Dickson, “Solid state phase change in HMX during dropweight impact,” in *13th International Detonation Symposium*, 2007, pp. 681–688.

[53] H. Czerski, M. W. Greenaway, W. G. Proud, and J. E. Field, “β-δ phase transition during dropweight impact on cyclotetramethylene-tetranitroamine,” *J. Appl. Phys.*, vol. 96, no. 8, pp. 4131–4134, 2004.

[54] P. A. Franken, A. E. Hill, C. W. Peters, and G. Weinreich, “Generation of optical harmonics,” *Phys. Rev. Lett.*, vol. 7, no. 4, pp. 118–120, 1961.

[55] F. L. Pedrotti, L. S. Pedrotti, and L. M. Pedrotti, *Introduction to optics*, 3rd ed. Upper Saddle River: Pearson Education Inc., 1987.

[56] A. Mazumdar, “Principles and techniques of Schlieren imaging systems.” Columbia University, pp. 1–16, 2013.

[57] D. G. Gregory-Smith, A. R. Gilchrist, and P. Senior, “A combined system for

measurements of high-speed flow by interferometry, Schlieren and shadowgraph," *Meas. Sci. Technol.*, vol. 1, no. 5, pp. 419–424, 1990.

[58] D. R. Guildenbecher, "Schlieren apparatus for applications to shock tube investigations." Purdue University, pp. 1–9, 2011.

[59] G. S. Settles, "The Penn State full-scale Schlieren system," in *11th International Symposium on Flow Visualization*, 2004, pp. 1–12.

[60] J. L. Devore, *Probability and statistics for engineering and the sciences*, 7th ed. Duxbury: Thomson Brooks/Cole, 2008.

[61] V. Placet, and P. Delobelle, "Mechanical properties of bulk polydimethylsiloxane for microfluidics over a large range of frequencies and aging times," *J. Micromech. Microeng.*, vol. 25, no. 3, p. 035009, 2015.

[62] R. R. Stevens, "Modeling of Sylgard adhesive strength," *LA-UR-15-20757*. Los Alamos National Laboratory, 2015.

[63] C. Liu, J. D. Yeager, and K. J. Ramos, "Bonding energy of sylgard on fused quartz : an experimental investigation," *Philos. Mag.*, vol. 95, no. 4, pp. 346–366, 2017.

[64] I. D. Johnston, D. K. McCluskey, C. K. L. Tan, and M. C. Tracey, "Mechanical characterization of bulk Sylgard 184 for microfluidics and microengineering," *J. Micromech. Microeng.*, vol. 24, no. 3, p. 035017, 2014.

[65] N. D. Parab, Z. A. Roberts, M. H. Harr, J. O. Mares, A. D. Casey, I. E. Gunduz, B. Claus, T. Sun, K. Fezzaa, S. F. Son, and W. W. Chen, "High speed X-ray phase contrast imaging of energetic composites under dynamic compression," *Appl. Phys. Lett.*, vol. 109, no. 13, p. 131903, 2016.

[66] J. O. Mares, Z. A. Roberts, I. E. Gunduz, N. D. Parab, T. Sun, K. Fezzaa, W. W. Chen, S. F. Son, and J. F. Rhoads, "In-situ X-ray observations of ultrasound-induced explosive decomposition," *Appl. Mater. Today*, vol. 15, pp. 286–294, 2019.

[67] Z. A. Roberts, J. A. Wickham, C. J. Sorensen, T. D. Manship, I. E. Gunduz, S. F. Son, and J. F. Rhoads, "Mesoscale observations of the thermal decomposition of energetic composites under ultrasonic excitation," *J. Appl. Phys.*, vol. 125, no. 21, p. 215114, 2019.

[68] B. W. Asay, B. F. Henson, L. B. Smilowitz, and P. M. Dickson, "On the difference in impact sensitivity of beta and delta HMX," *Energ. Mater.*, vol. 21, no. 4, pp. 223–235, 2010.

[69] B. N. J. Persson, and E. Tosatti, “The effect of surface roughness on the adhesion of elastic solids,” *J. Chem. Phys.*, vol. 115, no. 12, pp. 5597–5610, 2001.

[70] I. J. Lochert, M. D. Franson, and B. L. Hamshere, “Reduced sensitivity RDX (RS-RDX) part I : literature review and DSTO evaluation.” DSTO Systems Sciences Laboratory, 2003.

[71] A. D. Casey, Z. A. Roberts, A. Satija, R. P. Lucht, T. R. Meyer, and S. F. Son, “Dynamic imaging of the temperature field within an energetic composite using phosphor thermography,” *Appl. Opt.*, vol. 58, no. 16, pp. 4320–4325, 2019.

[72] I. J. Lochert, M. D. Franson, and B. L. Hamshere, “Reduced sensitivity RDX (RS-RDX) part II : sympathetic reaction.” DSTO Defence Science and Technology Organisation, 2006.

[73] O. Bolton, L. R. Simke, P. F. Pagoria, and A. J. Matzger, “High power explosive with good sensitivity: a 2:1 cocrystal of CL-20:HMX,” *Cryst. Growth Des.*, vol. 12, no. 9, pp. 4311–4314, 2012.

[74] A. Mcbain, V. Vuppuluri, I. E. Gunduz, L. J. Groven, and S. F. Son, “Laser ignition of CL-20 (hexanitrohexaazaisowurtzitane) cocrystals,” *Combust. Flame*, vol. 188, pp. 104–115, 2018.

[75] B. M. Dobratz, and P. C. Crawford, *LLNL Explosives handbook-properties of chemical explosives and explosive stimulants*. Livermore, California, 1985.

# VITA

Zane Roberts received his B.Sc. degree in mechanical engineering with an applied mathematics minor, graduating cum laude from Boise State University in Idaho in the spring of 2014. After time spent as a quality control engineer at a plastic parts fabrication facility, he enrolled in graduate school in the spring of 2015 as a direct to Ph.D. student where he researches energetic materials. Zane is currently enrolled in the School of Mechanical Engineering at Purdue University in Indiana under advisers Professor Steve Son and Professor Jeff Rhoads.

# PUBLICATIONS

**Z. A. Roberts**, A. D. Casey, I. E. Gunduz, J. F. Rhoads, and S. F. Son, "The effects of crystal proximity and crystal-binder adhesion on the thermal responses of ultrasonically-excited composite energetic materials," *Journal of Applied Physics*, vol. 122, no. 24, pp. 244901, (2017).

**Z. A. Roberts**, J. O. Mares, J. K. Miller, I. E. Gunduz, S. F. Son, and J. F. Rhoads, "Phase changes in embedded HMX in response to periodic mechanical excitation," *"Challenges in mechanics of time-dependent materials," in Proceedings of the 2016 Annual Conference of Experimental and Applied Mechanics*, vol. 2, pp. 79-86, (2016).

**Z. A. Roberts**, J. A. Wickham, C. J. Sorensen, T. D. Manship, I. E. Gunduz, S. F. Son, and J. F. Rhoads, "Mesoscale observations of thermal decomposition of energetic composites under ultrasonic excitation," *Journal of Applied Physics*, vol. 125, no. 21, pp. 215114, (2019).

N. D. Parab, **Z. A. Roberts**, M. H. Harr, J. O. Mares, A. D. Casey, I. E. Gunduz, M. Hudspeth, B. Claus, T. Sun, K. Fezzaa, S. F. Son, and W. W. Chen, "High speed X-ray phase contrast imaging of energetic composites under dynamic compression," *Applied Physics Letters*, vol. 109, no. 13, pp. 131903, (2016).

J. O. Mares, **Z. A. Roberts**, I. E. Gunduz, N. D. Parab, T. Sun, K. Fezzaa, W. W. Chen, J. F. Rhoads, and S. F. Son, "In-situ X-ray observations of ultrasound-induced explosive decomposition," *Applied Materials Today*, vol. 15, pp. 286-294, (2019).

A. D. Casey, **Z. A. Roberts**, A. Satija, T. R. Meyer, and S. F. Son, "Visualization of the temperature field from within an energetic composite using phosphor thermography," *Applied Optics*, vol. 58, no. 16, pp. 4320-4325, (2019).

A. Dandekar, **Z. A. Roberts**, S. C. Paulson, W. W. Chen, S. F. Son, and M. Koslowski, "The effect of the particle surface and binder properties on the response of polymer bonded explosives at low impact velocities," *Computational Materials Science*, vol. 166, pp. 170-178, (2019).

B. Tanasoiu, J. Palsdottir, N. D. Parab, M. Harr, **Z. A. Roberts**, J. O. Mares, I. E. Gunduz, T. Sun, K. Fezzaa, S. F. Son, W. W. Chen, and M. Koslowski, "Adhesive energy between Sylgard and inclusions: experiments and model calibration," *32nd Technical Conference of the American Society for Composites*, vol. 2, pp. 862-875, (2017).